A Wide Area
Bipolar Cascade
Resonant Cavity
Light Emitting Diode
for
A Hybrid Range-Intensity Sensor

DISSERTATION

Reginald J. Turner, Major, USAF

AFIT/DEE/ENG/08-12

**DEPARTMENT OF THE AIR FORCE**
**AIR UNIVERSITY**

# AIR FORCE INSTITUTE OF TECHNOLOGY

**Wright-Patterson Air Force Base, Ohio**

# A Wide Area
# Bipolar Cascade
# Resonant Cavity
# Light Emitting Diode
### for
# A Hybrid Range-Intensity Sensor

DISSERTATION

Presented to the Faculty

Graduate School of Engineering and Management

Air Force Institute of Technology

Air University

Air Education and Training Command

In Partial Fulfillment of the Requirements for the

Degree of Doctor of Philosophy in Electrical Engineering

Reginald J. Turner, M.S.E.E., M.DIV

Major, USAF

19 June 2008

# A Wide Area
# Bipolar Cascade
# Resonant Cavity
# Light Emitting Diode
## for
# A Hybrid Range-Intensity Sensor

Reginald J. Turner, M.S.E.E., M.DIV

Major, USAF

Approved:

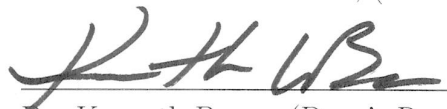| | |
|---|---|
| _Maj LaVern A. Starman, (Chairman)_ | 7 May 08 <br> Date |
| _Lt Col James A. Fellows, (Member)_ | 5 MAY 08 <br> Date |
| _Dr. Guna Seetharaman, (Member)_ | 5 May 08 <br> Date |
| _Dr. Robert Bedford, (Member)_ | 05 MAY 2008 <br> Date |
| _Dr. Michael A. Marciniak, (Member)_ | 6 May 08 <br> Date |
| _Dr. Kenneth Bauer, (Dean's Representative)_ | 2 MAY 08 <br> Date |

Accepted:

M. U. Thomas

Dean, Graduate School of Engineering and Management

27 May 08

Date

AFIT/DEE/ENG/08-12

## *Abstract*

Autonomous Ground Vehicles (AGV) will require high-speed, real-time three dimensional (3-D) image processing to navigate treacherous terrain in order to complete their assigned mission without a human in the loop. LIDAR scanners of the 3-D variety, provide the necessary area coverage for 3-D image processing, but lack the speed to deliver the collected data for real-time processing. A novel Hybrid Range-Intensity System (HRIS) has been proposed for imaging large swaths of area very rapidly. This system is comprised of two infrared cameras, an illumination source, a control and coordination system to position the cameras, and signal processing algorithms to extract the contour image of the scene.

This dissertation focused on the development of an illuminator for the HRIS. This illuminator enables faster image rendering and reduces the potential of errors in return signal data, that could be generated from extremely rough terrain. Four major achievements resulted from this work, which advance the field of 3-D image acquisition. The first is that the TJ is an effective current spreading layer for LEDs with mesa width up to 140 $\mu$m and current densities of $\sim 1$ x $10^6$A/cm$^2$. The TJ allows fabrication of an efficient illuminator, with required geometry for the HRIS to operate as a real-time 3-D imaging system. Secondly, a design for a Bipolar Cascade-Resonant Cavity Light Emitting Diode (BC-RCLED) has been accomplished, that will illuminate the FOV of the hybrid-ranged intensity system with a single sweep of the beam. This device is capable of producing $\sim 330$ mW of output power. Additionally, from this work, key parameters for HRIS design were identified. Using a collection optic with a 15 cm diameter, an HRIS mounting height of 1.5 m, and a detector integration time of 330 msec, a SNR of 20 dB was achieved. Lastly, we demonstrated that the BC-RCLED designed for the HRIS can deliver sufficient energy to produce the required SNR. Also, through parametric analysis, we determined that a system

trade-off, between the collection optic diameter, and the integration time, results in an increase in the SNR from 20 to nearly 50, or extending the operational range from 50 to nearly 130 m.

*Acknowledgements*

## Table of Contents

## List of Figures

x

xiv

xviii

xix

# List of Tables

## List of Abbreviations

# A Wide Area

## Bipolar Cascade

## Resonant Cavity

## Light Emitting Diode

for

## A Hybrid Range-Intensity Sensor

# I.  Introduction

### 1.1   Introduction

A new effort has been proposed as a joint program between the Air Force Institute of Technology, (AFIT), and the Air Force Research Laboratory, Sensors Directorate (AFRL/RY), to develop devices and components, enabling three-dimensional (3-D) imaging systems for autonomously guided mobile platforms. The impetus for this effort stems from published research that suggests that vast improvements in combat-orientated target identification systems are seen when 3-D visual feedback is utilized [50]. Additionally, having an imaging system, capable of acquiring range and intensity data, quickly and efficiently, has been a goal for quite some time [43]. Developing this capability represents significant progress in the world of computer vision and robotics [43], a fact that has drawn the interest of the defense community, to include the Defense Advanced Research Projects Agency (DARPA). DARPA instituted an event, The DARPA Grand Challenge, in 2004, in response to a Congressional and DoD mandate, where robots navigate a predetermined obstacle course without any human input. It is intended to accelerate research and development in autonomous ground vehicles (AGVs) that will help save American lives on the battlefield. The Grand Challenge brings together individuals and organizations from industry, the Research and Development (R&D) community, government, the armed

services, academia, students, backyard inventors, and automotive enthusiasts in the pursuit of a technological challenge [8] .

A vital capability of any vehicle entered into the competition is the ability to circumnavigate obstacles and difficult terrain on the course. Forward-looking imaging systems have been employed by most of the vehicles entered, in lieu of Global Positioning System (GPS) navigation systems. A severe limitation of the forward-looking imaging system is real-time image processing. Because there is a time limit levied to negotiate the course, a minimum speed is necessary. These robots can only move where they can see, thus, there is a maximum speed the vehicle can safely travel, based on the data that can be received and processed in real-time. Therefore, developing an imaging system that enables real-time processing is of great interest, since it could reduce the time to render an image, and increase the robot's travel speed.

Image rendering can be accomplished in three stages: first, the scene of interest is captured by an acquisition system, like an infrared or microwave radar; next, the data gathered by the acquisition system is processed to extract the signal from the noise, using signal processing algorithms; then, the extracted signal is used to create a graphical depiction of the scene in a digitized format, or an image, for the robot to use for navigation. Each stage takes a finite amount of time to complete, and reducing the overall time to generate the image is accomplished by reducing the duration of one or more of these stages. The effort outlined in this dissertation discusses an advanced sensor, which reduces the data acquisition stage by using multiple sensors that are coplanar on the mobile platform, and separated by a known distance [43]. By having coplanar sensors, an autonomous platform can capitalize on stereopsis, which is the process in visual perception that leads to the perception of stereoscopic depth. This depth emerges from the fusion of two slightly different projections of a scene recorded by two sensors. Stereopsis can be used to determine the distance from the platform to a point in the scene, and subsequently, render an image of the scene. This technique utilizes an energy source to project a sheet of light on the target area, and sensors to image the illuminated area. Sources are typically laser diodes,

whose emission pattern is spread over the target area, using vibrating mirrors, or a series of optics [43]. The source determines the range, and establishes the speed of acquisition of the system, due to the maximum output capability of the device, and the method used to traverse the area to be imaged, scanning or starring. Considerable time delays can be introduced into the image rendering process if relatively long time lags are created during the data acquisition stage. More detail on the advance sensor will be offered in a later section.

Research objectives, for the advance sensor development, were established, initially, using an ultra-light aerial platform as the vehicle that would use the system. These objectives were categorized into system level and device level, which include:

- System Level Objectives

    - 50 meter look ahead range from source to target (aerial platform)

    - SNR $\geq$ 20 dB to create a robust system

    - Deliver a striped emission pattern, having a width to length aspect ratio of 0.006, to the target

- Device Level Objectives

    - Develop a device, most likely one of large area, to deliver the required energy and emission pattern to the target

    - Device should have a uniform emission pattern across the surface of the device

    - Device design should be optimized for maximum output
        * Utilize multiple active regions (AR)
        * Separate stages with Esaki tunnel junctions (TJ)
        * Integrate a resonant cavity (RC) structure to increase the probability of capturing most of the emitted energy into optics

– Place the TJ at a distance from the active region which limits it impact on overall device operation

– Optimize the device size, such that, the TJ is an effective current spreading layer

To determine the aspect ratio for the system, the feature size of potential objects in the environment were considered. If the proposed sensor is used on a ground vehicle, the viewing resolution must be acute enough to discern objects that are the width of standard automobile tires, or smaller. A typical passenger vehicle tire is about 23 cm wide [59], so the width of the stripe should be smaller than the tire width to be able to image objects that could present a serious obstacle for the tire to surmount. For this reason, 18 cm was the agreed upon width of the stripe. The length of the stripe was chosen to match the width of a typical multi-lane highway, which is approximately 3000 cm. The ratio of these dimensions produce the 0.006 aspect ratio used for the proposed system.

Because the proposed system is an active system, a light source must be created to illuminate the scene, so that the sensors can collect the return signal, much in the same way as the human vision system collects image data from scenes illuminated by the sun. The human brain processes the data and renders an image that can be used for navigation, among other things. Similarly, the light source for the imaging system illuminates the scene and the sensors collect the image data, much like human eyes, and the data used to render an image, as with the human vision system. A suitable illuminator makes this sequence more efficient. A suitable illuminator is one that can deliver sufficient energy to the target, and subsequently, adequate energy to the sensors, at a level where the scattered energy can be detected and the image signal extracted. Two device options were considered to meet the illuminator specification, which include, 1) semiconductor lasers, either edge emitting lasers or vertical cavity surface emitting lasers (VCSELs), and 2) wide area light emitting diodes (LEDs).

Edge emitting semiconductor lasers are devices that have been well characterized and extensively used for over 40 years. Power ratings have been reported as achieving levels of up to 5 W and higher. VCSELs have grown in popularity over the past few years also, with several investigations currently underway to exploit their full capability [52]. Both devices are viable options for this system, but do present a need for caution. Lasers are coherent sources and coherent sources capable of delivering large amounts of energy over a small area can cause eye damage, and could be subject to government regulation, which could complicate the deployment of any system using them. Also, lasers tend to have relatively small surface areas to enhance current confinement, and reduce the number of optical modes that can persist in the cavity, in particular, transverse modes for vertical cavity devices, which effect the beam uniformity. Beam uniformity can be mitigated using external apparatuses, but this complicates the optical system.

Wide area LEDs are well characterized devices and are growing in popularity [23]. Like all LEDs, wide area LEDs are less of a concern for causing eye damage, and, most importantly, are not closely subject to government regulation. Also, because attention to current confinement is not necessary in LEDs, since modal density is not necessarily problematic, devices with very large surface areas can be fabricated. If a particular emission pattern is required, the device itself can be shaped, within reason, to project the necessary pattern, reducing the number of beam shaping optics needed. One limitation of wide area LEDs is the surface area itself. Current crowding becomes an issue in wide area devices and impacts the total device output power and beam uniformity. A detailed discussion on mitigation strategies will be presented later in this dissertation.

Although both of the device types mentioned are viable options, the wide area LED was selected for development, primarily, because it offers tremendous flexibility in device shape. Relatively small width to length aspect ratio devices are possible when designed as an LED. In addition to the benefits listed above, an investigation involving similar devices was already underway at AFRL/RY, and equipment was

configured to support that investigation, several wafer samples with similar LED structures were previously grown, and the support staff and other researchers were already engaged in that effort. The work being proposed in this dissertation is an extension of the work at AFRL/RY [53] and differs in primary focus. Previous work focused on multi-stage VCSEL optimization and design, this effort utilizes insights from that effort in LED design, while also focusing on beam uniformity, current crowding, and, to a lesser degree, the impact of heating in wide-area LEDs.

For this application, a wide area Bipolar-Cascade Resonant-Cavity Light Emitting Diode (BC-RCLED) has been designed and is detailed in this report. Several effects were studied during the course of this research, which culminates in a demonstration of the emitter's ability to project sufficient energy onto a target down range, and using an off-the-shelf sensor, to detect the return signal.

The rest of this chapter provides some background on the problem of 3-D imaging in real-time. It also presents a conceptional rendering of a hybrid range-intensity image sensor, which uses an illuminator and two cameras for imaging. Lastly, an introduction of the final demonstration experiment is made.

## 1.2   Real-time 3-D Imaging of Unstructured Scenes

Many reported 3-D perception systems currently have the ability to perceive the shape, orientation and location of objects in environments that are static, or change at a slow rate. Also, perception systems operating in structured or controlled environments have performed very well [5]. A structured environment is one where there is a prior knowledge of the objects contained there in, as well as the location of these objects  [5]. Such an environment poses a less complex problem to 3-D perception techniques than does one in which the objects are not known, change rapidly in shape, orientation, and location, with respect to the image retrieval and processing speed of the system, or the environment (background) is unfamiliar. The latter describes what is known as an unstructured or uncontrolled environment.

Several techniques for mapping environments in three dimensions have been published; many of them were used in familiar settings with objects whose classification were previously known [43] [49]. According to the literature, sensor fusion is well suited for the complex problem of imaging in familiar and unfamiliar environments with unknown objects. This technique, much like the human vision system, integrates information, which is derived from multiple sensors looking from different vantage points, and renders a 3-D image using stereopsis. There are drawbacks to producing real-time 3-D imagery using sensor fusion as a processing technique. One major issue is processing time. Since each sensor obtains data sequences independently, the data from one sensor must be synchronized, or registered, with the data from the other, to produce an accurate image. The process is known as registration, and can significantly slow down real-time image processing. As stated in [49] the processing speed of acquiring and analyzing an image must be comparable to the speed of execution of the specific task. A system with two sensors and an illuminator, as discussed previously, can expedite processing, by reducing registration time. A Hybrid Range-Intensity Sensor (HRIS) system has been proposed to address these issues.

## 1.3   *The Hybrid Range-Intensity Image Sensor System*

The HRIS has been proposed in [43] [50], and will produce the registered data sequences used in the sensor fusion algorithm to quickly render the 3-D scene. A notional depiction of the HRIS is shown in Figure 1.1. This depiction shows only one camera for collecting signal returns, even though two would be used for an actual system to generate the two sets of images from different perspectives required for 3-D rendering. The proposed sensor is made of four components, which include: 1) two IR cameras, 2) an illumination source that generates a planar sheet of energy, nominally perpendicular to the image plane, projecting a stripe on the target, 3) a control and coordination system to position cameras with a desired geometrical relationship, and 4) signal processing algorithms to extract the contour image, calculate and identify
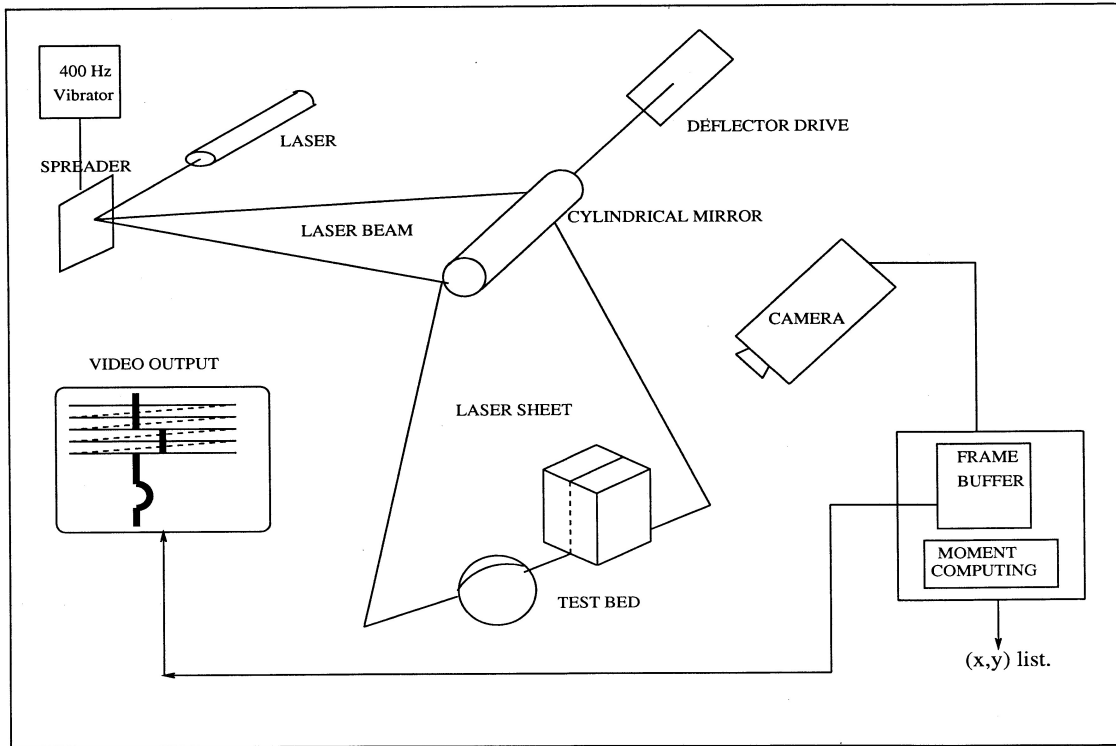
Figure 1.1: A notional depiction of an active sensor (the Hybrid Range-Intensity Sensor) using an illuminator that produces a sheet of energy, which projects a stripe on objects in the scene, the test bed. The laser is reflected off of a actuated spreader, which distributes the laser energy and directs it to a cylindrical mirror. The laser sheet can then be swept over the test bed. A video camera captures the illuminated image and provides a signal to a raster scan video output apparatus. [50]

the point correspondence of each point in the contour and recover the pertinent information for 3-D image construction [49]. Introducing the illumination source into this configuration mitigates the registration time-lag issue that could arise. Only the patterns illuminated by the source are collected as a data sequence. This reduces the number of patterns that must be searched to produce the final image. The illuminated points in the scene can be time stamped as the illuminator is modulated. This design capitalizes on the distance between the cameras to perceive the range of the object imaged, stereopsis, while recording the intensity data, which produces a range-intensity registered pair [49]. Conceptually, this system is very similar to a two dimensional (2-D) scanning Light Detection and Ranging system (LIDAR), but does not need to calculate the distance from the signal return time, as is the case with the LIDAR. Nevertheless, the LIDAR imaging process was used as a template in the analysis of this system.

LIDARs project radiation and use the temporally detected return signal to calculate distance [12]. They offer the capability to resolve very small targets, and can be laser range finders or laser scanners. Range finders can be upgraded and made into scanners, by sweeping the beam horizontally, and often vertically, via a set of rotating mirrors, to produce a series of points (point-cloud) over a swath of area. A point-cloud is the collection of reflected optical energy points returned from a target that has been imaged by a LIDAR scanner. As the number of points is increased, the resolution of the imaged area will increase. A finite time is required to produce the requisite number of points for desired image quality. Since several scans may be necessary to cover an area, the speed of the platform will suffer, as is the case with current mobile robots. Reducing the amount of time for data acquisition by eliminating the number of scans, will in effect, allow the vehicle to increase its safe traveling speed.

Additionally, if a platform is moving along the ground, a discontinuity in the mapping data can be introduced if the vehicle is traveling over very rough terrain, or if the vehicle is moving at a very high rate of speed. As the beam is swept in

1-9

front of the platform, which is moving perpendicular to the sweep direction, signal returns are registered. Adjacent returns may be separated by a distance too large to garner accurate image data. The remedy to this is to increase the pulse rate of the illuminator, which results in a higher spatial density of the scene, creating a larger point-cloud, which slows the sweeping speed of typical 2-D scanners. A beam that could cover a much larger swath of area with one or zero sweep would be ideal. We propose using an emitter that delivers a stripe with the same dimension as one of the axes (horizontal or vertical) to be scanned, to address this limitation. A STRiped EMittER (STREMER) has been designed for this purpose.

The STREMER is an emitter developed to be utilized with commercial-off-the-shelf (COTS) components to build an inexpensive sensor for 3-D data collection to be processed via an in-house developed sensor fusion algorithm. The Bipolar Cascade-Resonant Cavity Light Emitting Diode (BC-RCLED) structure, with stacked ARs separated by TJs to increase the device efficiency, uniformity, and total output power, is used for the STREMER design.

Although one stated application of this system comes from the DARPA Grand Challenge, this technology can be utilized in a number of applications, which require real-time, precise 3-D imagery, to include mobile robotic systems, multi-armed multi-sensory robots, and aerial reconnaissance [49]. In each application, principles of remote sensing are utilized. Basically, an adequate signal-to-noise ratio (SNR) must be reached for the sensor to perceive the target return signal, and distinguish it from the background noise, in order for usable data to be extracted. To achieve this SNR, an emitter that can deliver the energy needs to be produced and demonstrated using appropriate sensors. The next section discusses some key points of the remote sensing demonstration involving the final device.

## 1.4   Remote Sensing Demonstration

This research effort capitalized on the availability of several components that are production ready or under development. The sensor fusion algorithm developed

by Team Cajunbot [49] will perform the necessary processing of the collected data sequences to render the 3-D scene. COTS infrared (IR) cameras will be the passive sensors used in conjunction with an active illuminator to collect the image data. An emitter is the key component for successful acquisition of registered 3-D data pairs if using two cameras. If a stripe is projected, it will produce a larger point-cloud with a 1-D sweep of the area, in comparison to a point raster scanner that makes several sweeps, resulting in a reduced total time to acquire image data of the entire scene.

Using a projected stripe also mitigates the issue of potentially large physical separation between adjacent points. For example, if the illuminator is mounted such that the projected stripe is a line in the $y$-axis (vertical) and the beam is swepted across the scene in the $x$-direction (horizontal), during vertical jarring caused by very rough terrain, data points can still be projected at the target and collected by the sensors, provided the targets are still in the sensor's field of view. This would not be the case with a raster scan system. Typically, raster scan systems sweep a point in the $x$-direction (horizontal) successively, while moving a finite vertical distance after each horizontal sweep. Vertical jarring could produce a much larger gap in returned data, resulting in an incorrectly rendered scene. The full system was not tested in this effort, but two of the four hybrid sensor components, the illuminator and the IR camera, were integrated into a demonstration to collect data, which can be used to develop and refine the final system.

First, a beam train was designed to project the source down-range to the target. An 18 cm x 3000 cm rectangular spot was desired on target 5000 cm down range. The final beam train was made of a combination of glass and Fresnel lenses. This was necessary to keep with the idea of using the least expensive commercially available components. The next step was to find or develop a source that could deliver the desired amount of energy with this proper aspect ratio. The OSRAM IR Dragon® was selected for our investigation. The OSRAM device is a square emitter that required a beam train with a little more complexity and relies on interdigitated metal contacts to get even current distribution over the surface of the device. An in-house emitter, the

STREMER, was also designed and fabricated in a rectangular configuration with the desired aspect ratio, eliminating the need for cylindrical optics. The COTS camera used had a silicon focal plane array (FPA) detector, utilizing a charge-coupled-device (CCD) storage device. Next, a remote sensing demonstration was conducted using the low-cost COTS camera with a set-up similar to that shown in Figure 1.1. A test set-up consisted of the source (emitter) and a single IR camera, which was placed at a predetermined distance from a target. The source produced the energy plane and projected a stripe on the target, and the return signal was recorded. This experiment was conducted under ambient solar-like conditions in the laboratory at scaled distanced, spot sizes and drive currents.

## 1.5   *Document Organization*

This document is organized to bring together the three disciplines that supported this effort. First, it discusses some basic principles of remote sensing and how various researchers have addressed the laser scanner limitations like discontinuities in data collected, and the sensor fusion bottleneck. Next, relevant semiconductor device theory is highlighted to provide some background on considerations for final device development. Several preliminary experiments were necessary to design an optimized device and these experiments are summarized next. Then, the device design is presented, followed by results of device characterization experiments, and the remote sensing demonstration. Finally, conclusions and future investigation possibilities are presented.

# II.  Remote Sensing

## *2.1  Remote Sensing Background*

A simple definition for remote sensing is the gathering of information at a distance  [3]. Historically, this has been done with various types of systems, both active and passive, for a myriad of applications [3]. Active systems emit energy from a radiating source, at a particular wavelength, to illuminate the target and generate signal returns for the detector.  Passive systems depend on the natural energy emissions from targets to generate signal returns. In both cases, sensors intercept the returned signal from the targets, generating point-clouds, and this data is processed to garner information about the target [19]. The point-cloud returned from the target needs to be as dense as possible to render a richer picture.  The challenge then becomes how best to render a dense point-cloud as quickly as possible.

Remote sensing with light sources is very much like that done with millimeter-wave (MMW) sources, but one major difference is the wavelength.  Millimeter-waves are on the order of $10^{-3}$ m and LIDAR, or electro-optical (EO) systems, responds to energy with wavelengths on the order of $10^{-6}$ m.  This difference in wavelength allows EO systems to use much smaller components and have much better resolution.  This also causes degraded operation in fog and rain, since these particles can be sizes on the order of infrared wavelengths, thus, scattering power out of the detection system. The apertures or lenses in EO systems are on the order of centimeters and the angular resolution is on the order of single digit microradians.  Due to atmospheric attenuation, only a limited number of wavelengths can be used for a viable light detection system. There is a 98 % transmission window at the wavelength of primary interest, 980 nm, chosen in particular, due to its mature material development.

Ranging, detection, and tracking are some of the uses for LIDARs, and for this particular effort, ranging is most applicable.  Ranging is accomplished via a time-of-flight concept.  Laser pulses are emitted at a certain frequency and the returns are captured. The time between emissions and reception is measured and the distance to

the target is determined by the relation

$$R = \frac{ct}{2} \tag{2.1}$$

where $R$ is the distance between the source and target (range), $c$ is the speed of light, and $t$ is the time between transmit and return signals. The angular position of the target can also be determined from the target returns, provided the location of the source is known. Although ranging is the primary function of laser range finders, their capability can be upgraded by adding a rotating mirror to sweep the beam over a target area. The laser range finder typically samples a single point at a distance as opposed to two transverse dimensions. Adding a movable mirror extends the capabilities of the range finder, making a laser scanner. Several manufactures and researchers have adopted this technique to demonstrate this capability, and to produce commercially available LIDAR line scanners, and some of this work will be summarized later in the next section.

## 2.2 *Review of Application Specific Literature*

Nearly every one of the 35 teams participating in the DARPA Grand and Urban Challenge competitions used LIDAR as their primary vision system to include the top three teams [8]. Systems used include those manufactured by IEBO, SICK, Velodyne, BEA and Continental. Standard LIDARs utilize a line scanner for ranging and detection, like the one depicted in Figure 2.1 [60]. Line scanners illuminate one line at a time in the direct line-of-sight of the scanner, as is the case with most of the LIDARs mentioned above. Only the Velodyne sensor scans in a horizontal and vertical plane. As stated previously, the objective of any active scanning system is to produce a point-cloud of signal returns that is as dense as possible over the largest swath of area possible. Standard 2-D systems have a FOV directly in front of the sensor platform, and to the left or right of it depending on its scan angle capability, as shown in Figure 2.2. It can be seen that objects slightly above or below the plane
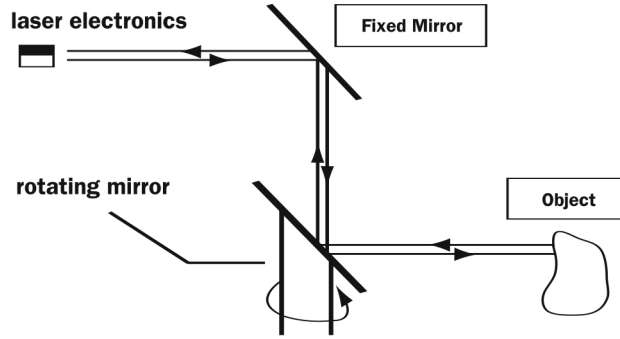
Figure 2.1:     Depiction of a rotating mirror added to a laser range finder taken from the Velodyne white paper. The rotating mirror rotates over $360^o$, causing the beam to scan an azimuth of $360^o$ [60].
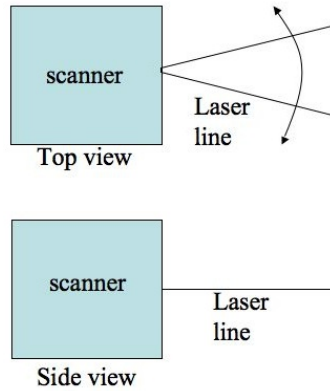


Figure 2.2:     A notional view of a 2-D scanner operational viewing angles. The top view shows an azimuth scan that can collect image data to the left and right of the scanner. The side view shows the line exiting the scanner. No elevation data can be collected with this system.

made by the laser line are not detected due to the direct emission trajectory of the scanner. The sensor can be mounted with a tilt, but the platform on which the LIDAR is mounted must move in the direction of interest, as shown in Figure 2.3. The steepness of the angle determines the look-a-head distance, which will be limited, and will subsequently limit the speed of travel of the platform.

Another issue with the 2-D systems is the possibility of discontinuities being introduced into the data stream due to excessive vibration or very high speeds, causing successive target returns to have a relatively large distance between them. These large
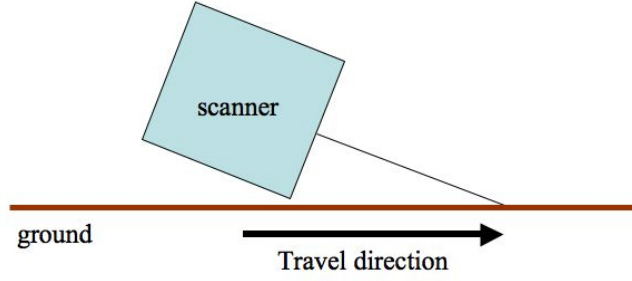
Figure 2.3: A notional scanner mounted in a tilt configuration. The tilt-mounted scanner can image the ground by traveling in the direction shown. The azimuth data can still be collected, but the viewing range is limited by the tilt angle.

distances between successive scans cause inaccuracies in the data collected, leading to an inaccurately rendered picture.

One way to overcome these issues is to add a third dimension to the system. By adding a third dimension to the scanner, the swath of area that can be imaged is enlarged, producing a point-cloud that covers a larger area, from which the scene can be better rendered. Multiple scanners can be utilized in concert to add the third dimension and, have been used by Waltheim et. al.. [61] and Kristnesne et. al.. [18]. In each instance one sensor is shifted by $90^o$ when mounted, producing separate scans in the $x - y$ plane and the $y - z$ plane. Another method used by Surmann et. al. [56], where a 2-D sensor is mounted on a servo-motor, is shown in Figure 2.4. This system has scanning capabilities that include an area of $150^o$ (h) x $90^o$ (v) and produces 115,000 points every 12 seconds, and a scanning resolution of 5 cm.

Ng [36] utilizes a 6-mirror assembly to produce a 3D scanner with a horizontal field of view (HFOV) of $90^o$ to $120^o$, and a vertical field of view (VFOV) of $60^o$, as depicted in Figure 2.5 and Figure 2.6. These figures show the 3-D laser scanner in a sketch and a set of pictures, respectively. A SICK scanner is mounted horizontally, producing vertical scans that are perpendicular to the ground. The vertical scans are then reflected from the mirror assembly and swept across the scene. Ng's apparatus has a horizontal resolution of $5^o$. Although adding the third dimension to the 2-D
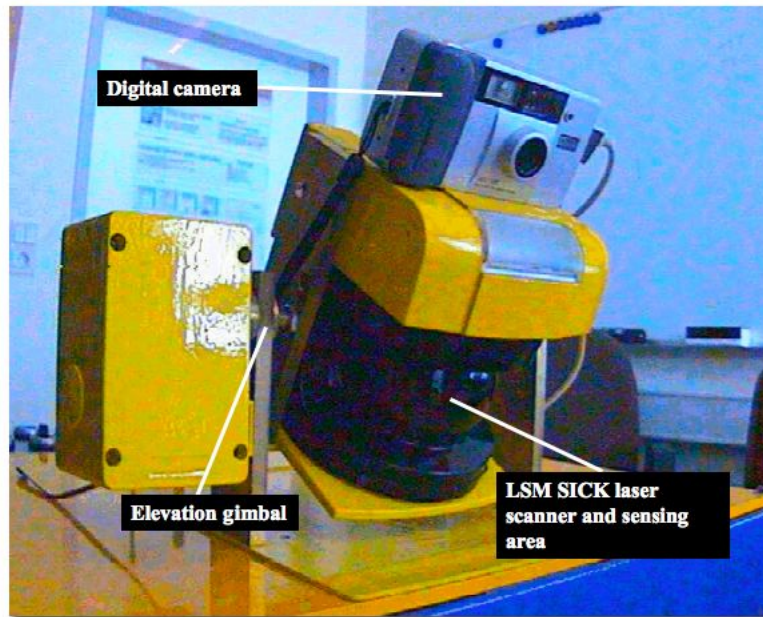
Figure 2.4:  LSM SICK scanner on a gimbal mount making a 3D scanner. Shown is the elevation gimbal axis and the laser scanner emitter and sensing viewing window in front of the scanner. Also, a digital camera is mounted atop the LSM SICK laser scanner [56].
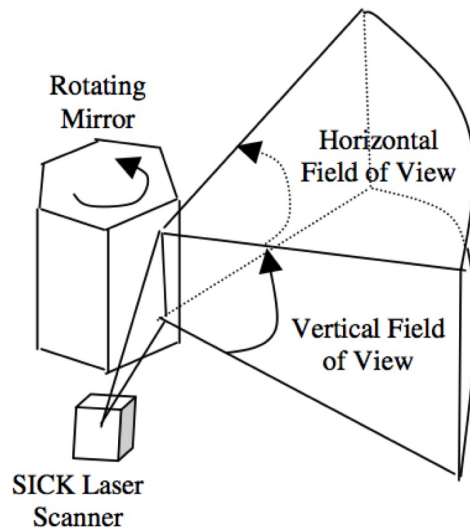


Figure 2.5:  Notional depiction of 3D scanner using SICK scanner and 6 mirror housing. This sketch displays how the energy from the scanner is projected onto the FOV [36].
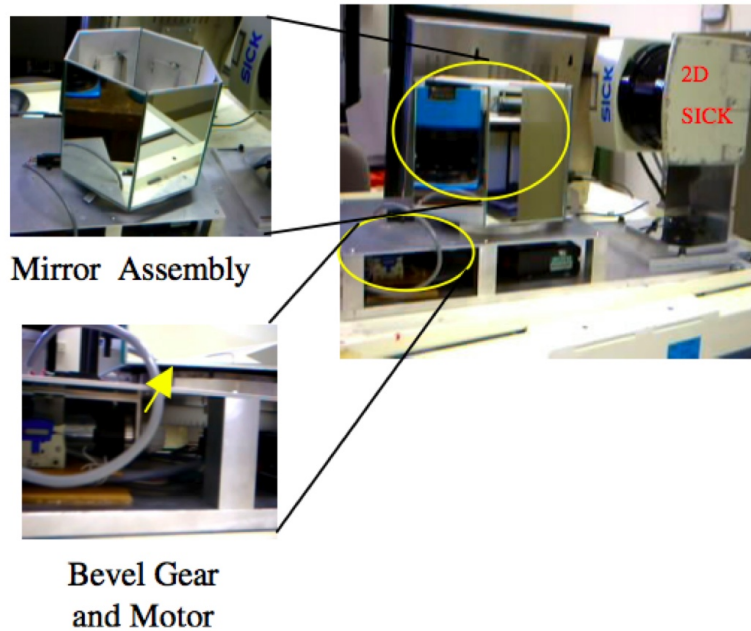
Figure 2.6: A 3D LIDAR using six-mirror assembly to continuously scan the target area. The 2-D LSM SICK scanner is mounted horizontally and makes a vertical scan. The six-mirror housing sweeps the vertical signal across the target area from left to right [36].

scanner will generate elevation data points, it reduces the number of azimuth data points. This results in a less dense point-cloud and a system with lower resolution [36].

Velodyne [60] has developed a sensor with a $360^o$ HFOV and a $26.5^o$ VFOV. The sensor is reported to have a range of up to 120 m and outputs a constant one million points per second regardless of rotational speed. The sensor has a bank of 64 emitter-detector pairs that are mounted on a motorized base that rotates a full $360^o$ at speeds up to 900 RPM (15 Hz). Figure 2.7 shows a depiction of the sensor and its components. Figure 2.8 shows the pattern in which the energy from the sensor would be delivered to the targeting area. Concentric circles are produced, as the closely spaced lasers are rotated about the sensors central axis.

Researchers at Advanced Scientific Concepts in association with the Air Force Research Laboratory [54] have produced a Flash LIDAR. In this system, a laser pulse is emitted from the transmitter while the optics spread the beam over the entire field of view of the receiver. In this way, all of the scene information is captured
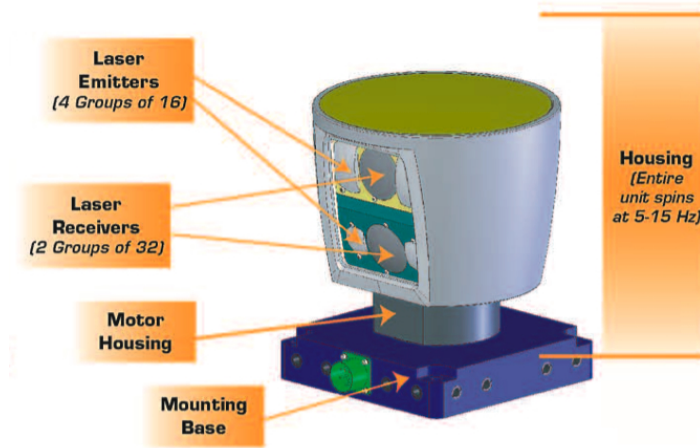
Figure 2.7: Velodyne High Density LIDAR. The LIDAR has a bank of 64 lasers emitting energy in a pattern that creates a virtual continuous stripe that is swept across the scene [60].
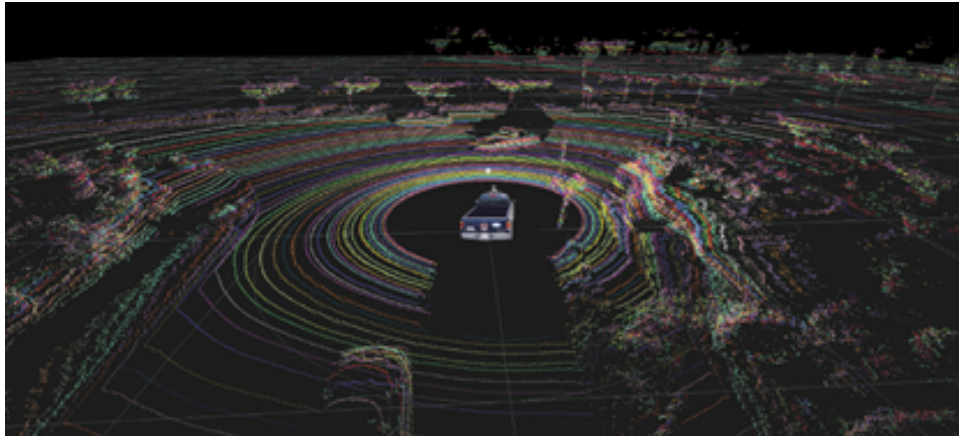


Figure 2.8: A depection of the area of coverage of the Velodyne sensor. The multiple laser banks produce concentric circles on the target area. [60].

simultaneously from a single laser shot or flash. A three-dimensional focal plane array (3-D FPA), with specialized read-out integrated circuitry (ROIC), is used to capture the reflected energy. Each pixel counts time from pulse emission to reflected pulse at the pixel, as well as temporal information about the reflected pulse. The laser pulse from the Flash LIDAR is reported to be eye-safe. The flash LIDAR system consists of a transmitter and transmit optics, and receiver optics collect the target-reflected light and directs it onto the 3D-FPA. The Flash LIDAR is shown in Figure 2.9. According to Seyrafi [51], the ideal sensor is one that could capture all of the image

energy returns with one flash of energy, much like a flash on a photographic camera. The Flash LIDAR is one such device, but is expensive, complicated and difficult to manufacture, and for these reasons is not widely commercially deployed [60].
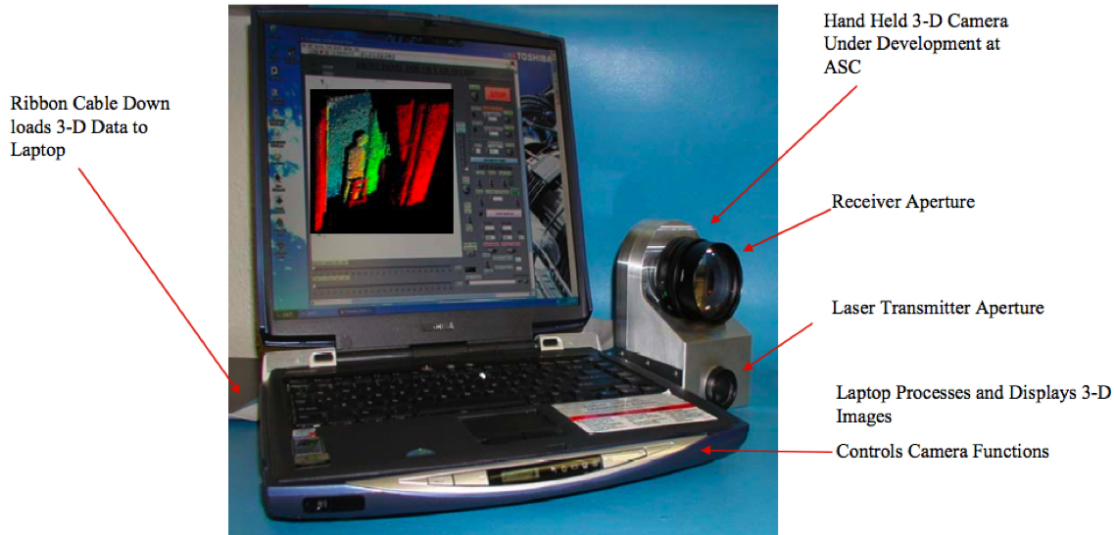


Figure 2.9:     The Flash LIDAR is shown connected to a laptop, with the receiver aperture, transmitter aperture, and a rendered image shown on the laptop screen [54].

We seek a cost-effective approach to deliver a comparable sensor using COTS devices, vastly reducing the cost of the sensor. This can be achieved by using a striped emission pattern to map the area seen by the FOV of the detector as shown in Figure 2.10. Each of the previously described modifications and improvements to the standard 2-D systems are efforts that move in the direction of producing a continuous emitter stripe instead of a scanner that delivers a pixelated pattern at the target. A stripe will only need to be scanned once to cover the FOV. This greatly reduces the scan time and makes the pixel registration simpler when using multiple sensors. A striped emission pattern would greatly increase the point-cloud density as compared to the 2-D and 3-D scanners described above; especially in the FOV perpendicular to the direction the stripe is swept.

Each of the suggested improvements to the standard 2-D system could create a severe bottleneck to processing electronics and standard data readout systems. With
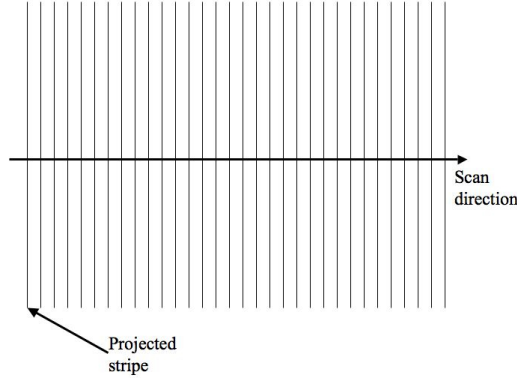
Figure 2.10:    A notional depiction of projected stripes at a distance scanned across an area.

such a largely dense point-cloud, it could take up to several minutes to process and render the image. This will be exacerbated with the integration of a second camera as proposed in Chapter 1. Insights from this research effort will enable the ultimate goal of fusing the imagery from two cameras and rendering a true 3D image, based on stereopsis, of the scene captured by the FOV of the two camera system, in order to reduce the overall image rendering time. A process known as registration has been presented to address this concern in [43] and [49]. Essentially, the packets of data, which are the target returns incident on the detector arrays of the cameras, can be time stamped by synchronizing them with the emitted pulse from the energy source. A more detailed explanation of the registration and render algorithm can be found in [49]. Also, by using two cameras, the range data is extracted from the camera position and not the line of sight process typically used with laser scanners, which reduces the processing stage of the rendering sequence.

## 2.3    Source Determination

A large part of this project is to demonstrate the capability of the HRIS for remote sensing applications by showing that a wide area LED can be used as a suitable illuminator. The goal of remote sensing is to have a signal current significantly larger than the noise current produced by the spectral background. Filters can be
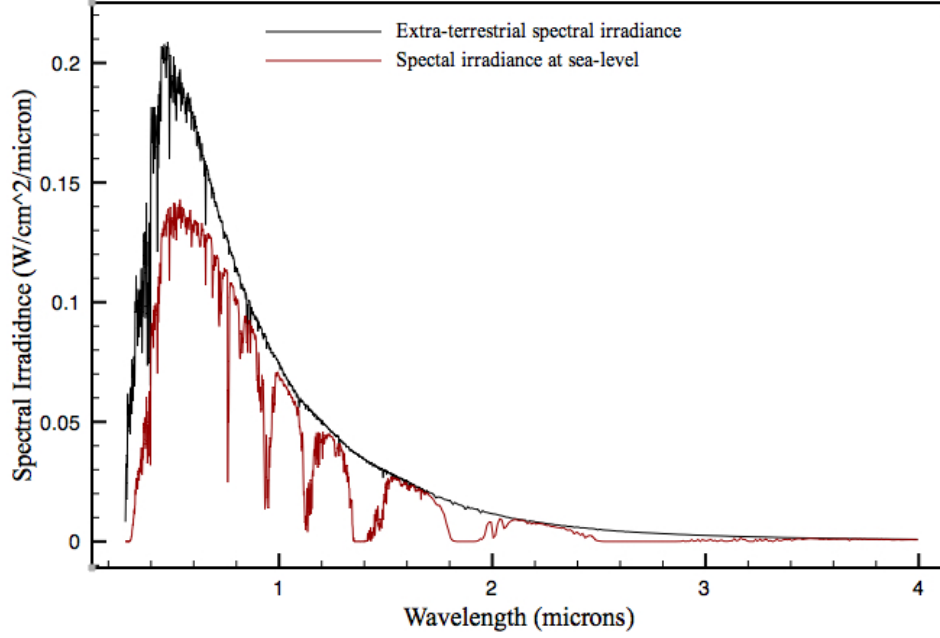
Figure 2.11:    The solar radiation spectrum.

used to reduce the noise level due to the background, and also using a very large energy source could help to increase the SNR. For this reason, the source must be adequately sized to successfully design an operational system. A source calculation was performed to determine the source size needed for the remote sensing demonstration. All calculations were accomplished using MATLAB® and the code used can be found in Appendix G.

Figure 2.11 shows the spectral irradiance of the sun as a function of wavelength, measured at the top of the earth's atmosphere and at sea-level, taken from the NASA Ames Research Center web site [1]. Planck's blackbody spectral radiance equation ($L_{eBB}$), at T = 5793 K, closely models the solar spectral radiance. Because $L_{eBB}$ has units $Wcm^{-2}\mu m^{-1}sr^{-1}$, multiply it by the solid angle the sun subtends from the earth, and the result is the spectral irradiance. The solar solid angle is found by

$$\Omega_{sun} = \frac{\pi\theta^2}{4} \tag{2.2}$$
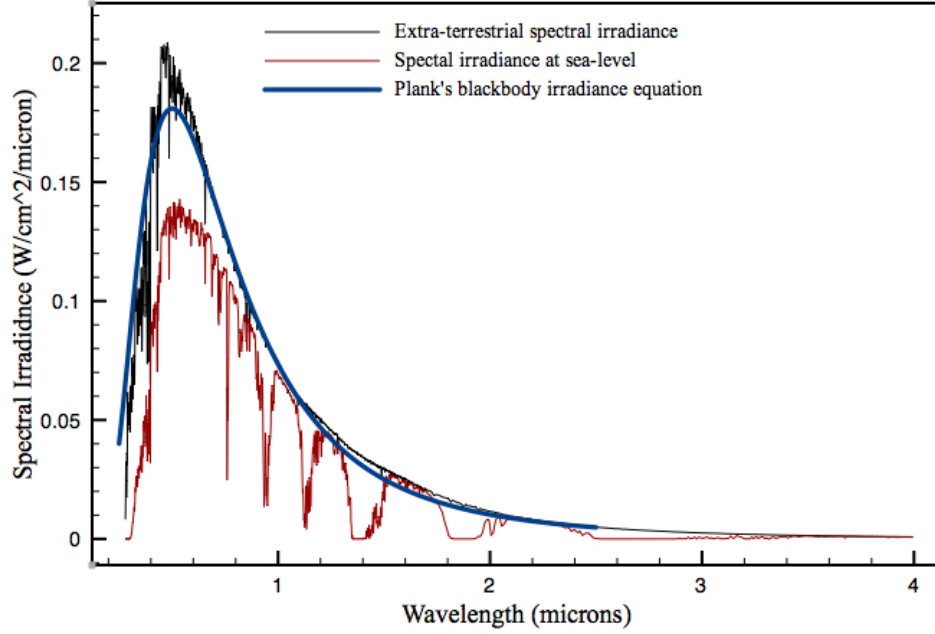
Figure 2.12:    The solar radiation spectrum.

where $\theta$ is the angle subtended by the sun, which is 9.3 mrad, and the solid angle has units of sr. The result of multiplying $L_{eBB}$ and $\Omega_{sun}$, is the Planck's spectral irradiance, $E_{eBB}$, and is shown in Figure 2.12 superimposed over the measured spectral solar irradiance.

Figure 2.12 showed the spectral irradiance over a wide band, but the band of interest for this investigation is from 0.8 - 1.1 $\mu$m, as determined by the Si detector used for detection, and the 0.8 $\mu$m long-pass filter on hand. Figure 2.13 shows a close-up view of the curves over the smaller range. Several *dips* in the measured sea-level plot exist, indicating that certain spectra of solar radiation are filtered by the earth's atmosphere, which allows only a fraction of the radiation at that wavelength to reach the earth's surface. Planck's spectral irradiance equation closely models the shape of the measured curve, but not the peaks and valleys over this range. A significant
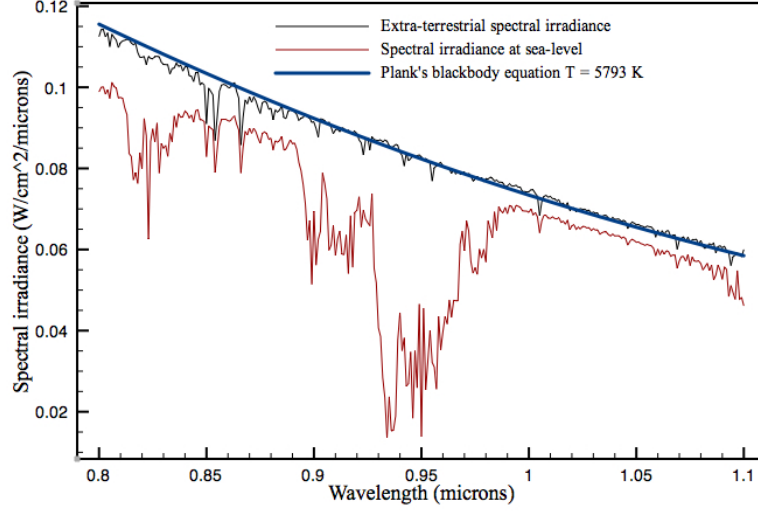
Figure 2.13:    The solar radiation spectrum from 0.8 - 1.1$\mu$m.

valley exists between 0.9 and 1.0 $\mu$m, and was modeled by the relation

$$\epsilon(\lambda) = 0.85 - 0.52 \; exp\left[-\left(\frac{(\lambda - .95)}{0.025^2}\right)^2\right] \qquad (2.3)$$

where $\lambda$ is the wavelength in $\mu$m. Equation 2.3 is plotted in Figure 2.14, and the $\epsilon(\lambda)L_{eBB}(\lambda)$ product is shown in Figure 2.15, superimposed over the measured spectrum, spanning the wavelength range of interest.    Using the product of these two
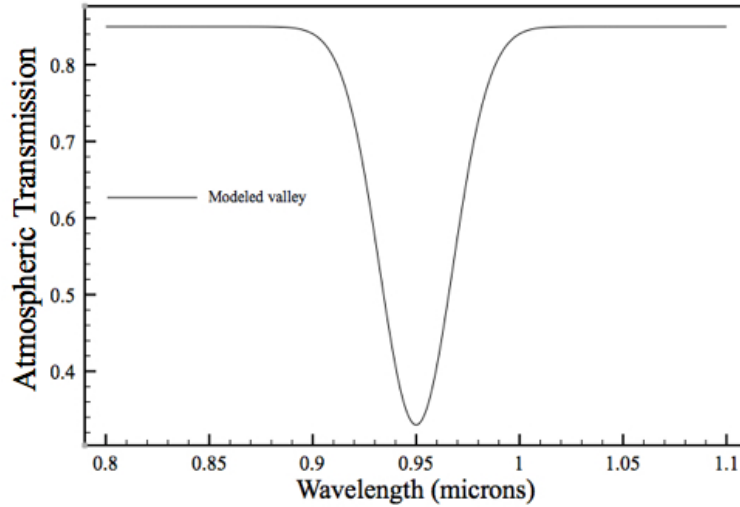


Figure 2.14:    Plot of equation modeling large valley between 0.9 and 1.1 $\mu$m.
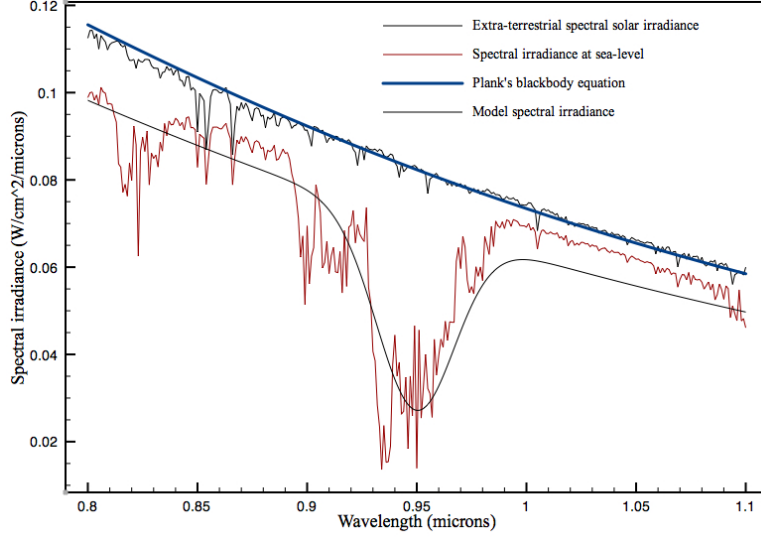
Figure 2.15:   The solar radiation spectrum from 0.8 - 1.1 $\mu$m.

equations, the noise due to the background solar radiation could be approximated and used to determine the source power needed to meet the 20 dB SNR requirement.

The form of Planck's blackbody equation used for this calculation was

$$L_{eBB} = \frac{2hc}{\lambda^5 e^{\left(\frac{hc}{\lambda kT}\right)} - 1} \tag{2.4}$$

where Planck's constant is $h = 6.626075$ x $10^{-34}$ J-sec, the speed of light is $c = 2.99792458$ x $10^8$ msec$^{-1}$, Boltzman's constant is $k = 1.380658$ x $10^{-23}$ JK$^{-1}$, with $\lambda = 0.980$ $\mu$m, and $L_{eBB}$ is given in Wcm$^{-2}\mu$m$^{-1}$sr$^{-1}$. For this endeavor, the solar radiance can be adequately modeled by the $\epsilon(\lambda)L_{eBB}$ product, and with some basic radiometry, the background noise due to solar radiation can be computed. Since $L_{eBB}$ has units Wcm$^{-2}\mu$m$^{-1}$sr$^{-1}$, so does the $\epsilon(\lambda)L_{eBB}$ product, and we seek the power, in watts (W) at the detector.

The energy from the sun will be reflected by the ground, or asphalt in this case, which has a reflection coefficient of $\rho = 6$ %. Since the reflected energy will be diffuse, a factor of $1/\pi$ is included to find the resultant luminance of the asphalt, and this reflected energy gets collected within the solid angle (FOV) of the system formed by

the detector and the collection optics (detector telescope). The instantaneous field of view (IFOV) of this optical system is determined by

$$\Omega_{IFOV} = \frac{A_{pixel}}{f^2} \tag{2.5}$$

and has units sr. The area of the collection optic is found by

$$A_{optic} = \frac{\pi D^2}{4} \tag{2.6}$$

and has units cm$^2$. A more detailed description of the optical telescopes for the camera and the source will be discussed in Chapter 5. The final spectral reflected solar power ($\Phi_{solar}$) collected by the detector telescope and delivered to the detector is, therefore, found by

$$\Phi_{solar} = \frac{\epsilon L_{eBB} \Omega_{sun} \Omega_{IFOV} \rho A_{optic}}{\pi} \tag{2.7}$$

which has as its units W$\mu$m$^{-1}$.

Figure 2.13 showed the total spectral irradiance from the sun incident on the surface of the earth over a 0.3 $\mu$m band. A portion of this incident energy will be reflected by the ground and delivered to the detector. Our system will be mounted on an autonomously guided vehicles (AGV), but could also be used on aerial platforms, as shown in Figure 2.16. In both cases, the radiation from the sun is diffusely reflected by the ground and will be incident on the detector surface, where it contributes to the noise current. For background-limited detection, one can assume that the shot noise will dominate other noise signals generated during electronic detection [26]. The shot noise is found by

$$i_{shot} = \sqrt{2q\bar{i}\Delta f} \tag{2.8}$$

where the electron charge is $q = 1.602$ x $10^{-19}$ C, the noise equivalent bandwidth $\Delta f = 1/2\tau_{int}$ Hz, where $\tau_{int}$ is the detector integration time in seconds, and $\bar{i}$ is the
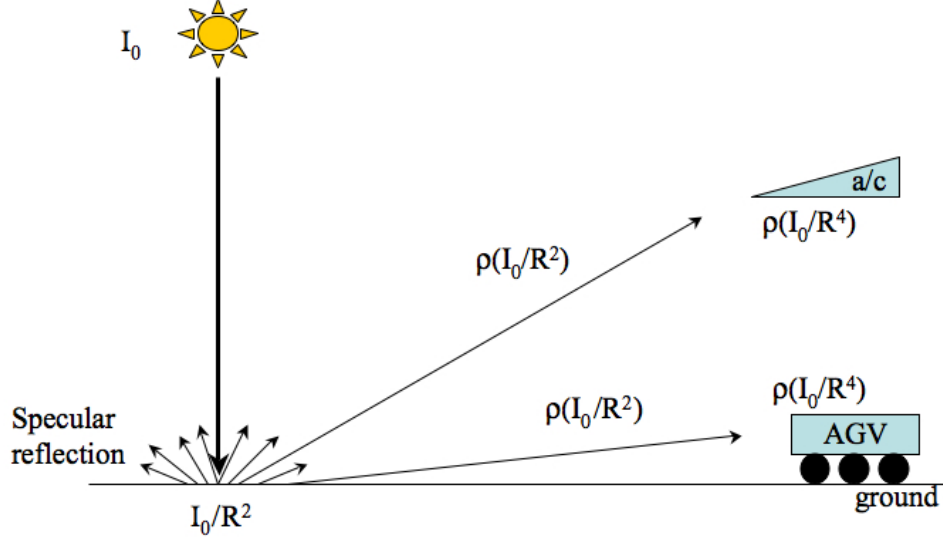
Figure 2.16:    The imaging environment showing a ground platform (AGV) and an aerial platform (a/c) receiving diffusely reflected energy from the sun.

received photon flux converted to current, found by

$$\bar{i} = \frac{\Phi_{solar}\eta q \lambda}{hc} \tag{2.9}$$

where $\Phi_{solar}$ is the received power at the detector in W, $\eta$ is the detector quantum efficiency, $\lambda$ is the wavelength of the energy collected in microns. For this case, $\lambda$ and $\Phi_{solar}$ extend over a band of wavelengths, so integration is necessary, causing $\bar{i}$ to become

$$\bar{i} = \frac{\eta q}{hc} \int_{0.8}^{1.1} \lambda \Phi_{solar}(\lambda) d\lambda \tag{2.10}$$

The ratio between the signal current ($i_{sig}$) and the noise current ($i_{shot}$) generated by energy incident on the detector is the SNR. The objective is not to produce a source large enough to surpass the background radiation, but one that will deliver energy sufficient to produce a signal current large enough to surpass the noise current, which results from random noise fluctuations generated by the background radiation incident on the detector. For electrical parameters, to include voltage, 20 dB represents a factor of 10x. Because $v = ir$, $r$ can be viewed as a constant, so the 20 dB conversion applies

to current, as well. The resulting signal current is superimposed on the background noise current, and when the signal is greater than the noise by a relatively large factor, background subtraction is much easier to accomplish. The signal current can be found by

$$i_{sig} = \frac{\Phi_{sig}\eta\lambda q}{hc} \tag{2.11}$$

where $\Phi_{sig}$ is the signal power received at the detector, originating from the LED source, and reflected from the target (ground), which has a reflection coefficient, $\rho$. $\Phi_{sig}$ is found by

$$\Phi_{sig} = \frac{\rho\Phi_{LED}\cos\theta_a A_{optic}}{\pi R^2} \tag{2.12}$$

where $\theta_a$ is the angle between the surface normal and the path of the returning radiation from the source on the platform. Figure 2.17 is a depiction of the imaging environment, showing a ground platform (AGV), an airborne platform (a/c), and their respective angles, represented by $\theta_1$ and $\theta_2$. Referring to Equation 2.12, at normal incidence, $\theta = 0$, the cos term in the numerator becomes one, when evaluated, resulting in the maximum amount of signal energy returned to the detector. At angles other than normal, the evaluated cos term in the numerator will be smaller than one, reducing the amount of reflected energy received at the detector.
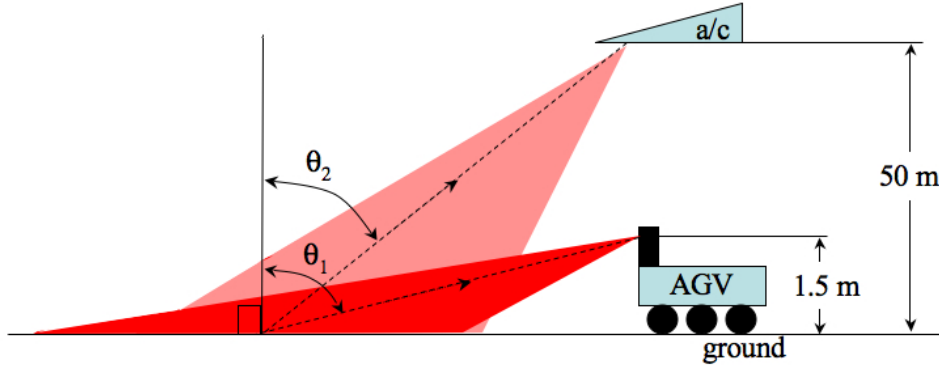


Figure 2.17:     Schematic of the imaging environment showing the projected area for an AGV and an airborne platform..

The AGV has a view of the target plane at a much larger angle from the surface normal, resulting in an increased projected area, than that of a platform with normal incidence. Planners have proposed a minimum range of 50 m, which, in the case of the airborne platform, means that the aircraft would fly at an altitude of 50 m, and could have a FOV that is normal to the platform, or could have a forward-looking FOV. The AGV's look-ahead range is 50 m, and the sensor mounting position affects the projected area at the target. In this instance, the AGV mounting height is assumed to be $\sim 1.5$ m. In both cases, the presence of the $\cos \theta$ term increases the projected area, which reduces the irradiance delivered to the target by the source. To determine the values of the angles, simple geometry can be used, which results in $\theta_1 = 1.54$ rad and $\theta_2 = \pi/4$ rad for the respective ground and airborne platforms.

In determining the appropriate parameters for achieving the desired SNR, a strong dependancy on $\tau_{int}$, the diameter of the collection optic ($D_{optic}$), and $\theta$ was observed, with a much smaller dependancy on $\eta_{det}$. Several plots were produced by varying each parameter and are included in Appendix F. The data plotted summarizes the relationship between the SNR and LED power needed at the source to achieve the desired SNR by the system. This data was used to design the final remote sensing demonstration, and a more detailed discussion is included in Chapter 5.

## 2.4   Summary

This chapter discussed some basics of remote sensing to include the concept of time-of-flight, as used in laser rangers, and how their capability is enhanced to function as 2-D laser scanners. The development of 3D LIDAR scanners has been discussed, to include a flash-LIDAR system, which is not realistically usable for this application. The Velodyne scanner portends the smart choice by using a large bank of emitters to form a virtual continuous line that can be swept across the target area. An emitter that delivers a striped emission pattern eliminates the need for the large bank of separate emitters, like that produced by the Velodyne scanner. To produce

an illuminator with an area as large as required for the striped pattern, several device design techniques were implemented and will be discussed in the next chapter.

Also presented in this chapter was the process used to determine the size of the source needed for the HRIS, and the remote sensing demonstration. Parametric studies produced several graphs showing how altering key parameters impact the overall power needed for the imaging system. These graphs can be used to design an imaging system by selecting a detector integration time, and desired SNR, which results in a particular source size. Likewise, a system range can be determined based on the detector integration time and the source power capability.

# III. Optical Device Design Theory

## 3.1 Introduction

A significant portion of this effort is devoted to developing the illuminator for the imaging system. What follows is a discussion of some of the key technological improvements in photonic devices, particularly to the LED, that are pertinent to the illuminator under development. To contextualize these advances, some basic semiconductor device physics is included. The Esaki Tunnel Junction (TJ) is an essential enabling technology for the emitter being designed. A detailed discussion of the TJ and how it is utilized for our purpose is also incorporated.

Our goal is to develop a wide area LED with and aspect ratio of 0.006, so that the projected energy pattern is a stripe. This stripe can be swepted over a swath of area and provide signal returns with one pass, greatly reducing the acquisition phase of image rendering as compared to the typical raster scan method used in LIDARs. There are challenges to producing a device with such a large surface area, which includes high injection current and decreased beam uniformity across the surface of the diode due to current crowding. To overcome these obstacles, some key technologies were used. With this in mind, specific characteristics are highlighted as part of this summary to include current spreading layers, the tunnel junction, distributed Bragg reflectors (DBRs) and mircrocavities. Our attention is focused on these areas, due to their importance in the development of the BC-RCLED STREMER. A more detailed discussion of other LED improvements can be found in Appendix A.

## 3.2 Device Physics

There has been an abundance of work developing methods for improving many of the different physical aspects of semiconductor optical devices. The discovery of quantum mechanics established the foundation for understanding the operation of semiconductors as a whole. Using quantum mechanics, researchers were able to conclude that carrier recombination is the basis of LED functionality, and therefore carrier recombination must be enhanced to produce efficient semiconductor light emit-

ters [20]. This section is a summary of key technologies, from the body of knowledge, developed from many research efforts conducted concerning luminescent semiconductors over the past 100 years. Since the development of the first LED, making a more efficient device has been an ongoing effort. To do this, one must understand how these devices operate. There are two key factors that contribute to producing an efficient LED: photon generation (internal quantum efficiency) and photon radiation (extraction efficiency). To understand the impact each has on the overall device operation, one must understand how these factors are significant. For photon generation, understanding recombination theory is essential since it is the process that produces photons. Within this process are mechanisms that inhibit the production of photons. These *photon inhibitors* need to be minimized or eliminated from the device to maximize its efficiency. The second factor, photon radiation, is a post recombination phenomenon. Once the photons are generated, they need to be expelled, or coupled, out of the device. The larger the number of photons coupled out of the device, the larger the output power of the device.

*3.2.1 Recombination Theory .* Intrinsic semiconductors at thermal equilibrium have an equal number of holes and electrons, which are the free carriers found in semiconductor material. At thermal equilibrium, the material system obeys the mass action law, i. e.

$$n_o p_o = n_i^2 \tag{3.1}$$

where $n_0$ and $p_0$ are the thermal equilibrium electron and hole concentrations and $n_i$ is the intrinsic carrier concentration. Under non-equilibrium conditions, which can be created by light absorption or current injection, excess carriers are created in the material. The total carrier concentration within the semiconductor is then given by

$$n = n_o + \Delta n \tag{3.2}$$

$$p = p_o + \Delta p \tag{3.3}$$

where $n$ and $p$ are the total electron and hole concentration in the material, and $\Delta n$ and $\Delta p$ are the excess carriers created under bias condition. Over time, the excited semiconductor will seek to re-establish thermal equilibrium by reducing the number of excess carriers. These excited electrons will loose energy and fall from the conduction band to the valence band. This falling is the process of carrier recombination and energy is released from the material as a result. Recombination may occur non-radiatively or radiatively, and each process will be briefly summarized.

*3.2.1.1 Non-radiative Recombination .* As described in the previous section, recombination will occur when excited carriers and available lower states exist within the same semiconductor material. This recombination may be radiative or non-radiative. During non-radiative recombination, the energy released from the excited carrier is converted to vibrational energy and dissipated into the crystal lattice as heat, or phonons. There are several factors that influence the occurrence of non-radiative recombination. One factor is the presence of defects in the lattice. Defects create energy states within the bandgap region, which precipitates unwanted recombination. These inter-gap energy levels, or traps, are efficient recombination centers and have been termed luminescence killers [46], since phonons result when traps are involved in recombination events. A detailed analysis of the recombination of carriers with traps, non-radiative recombination, referred to as Shockley-Read-Hall recombination, can be found in [14] [44], and [45].

Another undesirable recombination process is Auger recombination. During this process, the excited carrier transfers its energy to another carrier of the same type, for example from one electron to another one in the conduction band. As a result, the newly excited electron is elevated into a higher energy state within the conduction band. It will eventually loose its energy to the lattice in the form of heat. This process becomes a cause of significant photon reduction in highly doped materials or at high injection levels [46].

The semiconductor surface is also a location of unwanted recombination. The periodicity of the crystal ends at the boundary of the material, so a different energy band, with different energy states, will exist [47]. Also, dangling atomic bonds can be found at the surface. Since the surface is where the material abruptly ends, bonding at the chemical level ends there. Therefore, some atoms will not have filled electron orbitals, which again can produce traps within the energy gap. These dangling bonds may also rearrange themselves and form bonds with neighbors, making a totally different structure at the surface, which may have a different energy band structure than the rest of the material. This creates unwanted recombination centers at the surface.

*3.2.1.2 Radiative Recombination .* The desired recombination process is one in-which the amount of energy released equals the difference between the conduction and valence bands. There are materials that have a bandgap that equals optical energies, nominally between 0.1 and 5 $eV$, which are used for light emitting structures. Figure 3.1 shows a depiction of the recombination process. Schubert superbly summarizes radiative recombination theory [48], but what is of particular interest in our case is the rate (R) at which recombination occurs.
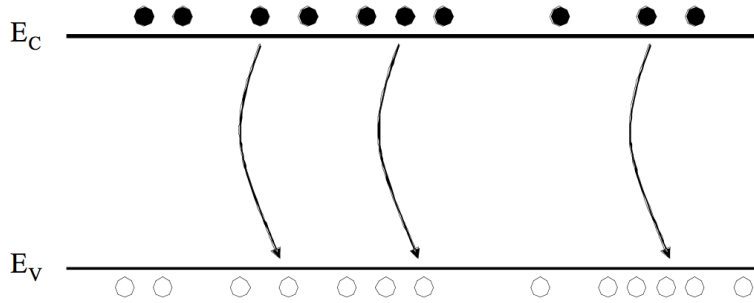


Figure 3.1:    Notional depiction of recombination showing holes in the valence band ($E_v$) and electrons in the conduction band ($E_c$).

Generally speaking, the probability of a radiative recombination event occurring is proportional to the excess hole and electron concentration. Also, recombination is

a time dependent process and can be modeled by

$$R = -\frac{dn}{dt} = -\frac{dp}{dt} = Bnp \qquad (3.4)$$

where $B$ is a proportionality constant known as the bimolecular recombination coefficient [48], and is calculated by

$$B = 3.0\text{x}10^{-10}\frac{cm^3}{s}\left(\frac{300K}{T}\right)^{\frac{3}{2}}\left(\frac{E_g}{1.5eV}\right) \qquad (3.5)$$

where $E_g$ is the bandgap of the semiconductor and $T$ is the temperature. For GaAs, $B$ is in the range of $10^{-10}cm^3/s$ at room temperature. For very high carrier concentrations (degenerately doped materials) the bimolecular recombination coefficient is dependent on the carrier concentration and is expressed as

$$B_{degenerate} = B - \frac{n}{N_c}B^* \qquad (3.6)$$

where $N_c$ is the density of states in the conduction band. The same equation can use the density of states in the valence band $N_v$ in place of $N_c$. Observed values of $B^*$ can be found in Olshansky et. al [37].

Temperature has a large impact on the spontaneous emission of the device, as can be seen in Equation 3.5, which shows that $B$ has significant temperature dependence. In addition to impacting the bimolecular recombination coefficient, temperature also affects the band gap of the material. This relationship is modeled as

$$E_g = E_g(0K) - \frac{\alpha T^2}{T + \beta} \qquad (3.7)$$

which shows that the energy gap decreases with increasing temperature, yielding longer wavelength emission. The parameters $\alpha$ and $\beta$ are fitting parameters, often referred to as Varshni parameters [47]. The Varshni parameters of several semiconductors has been compiled by Ioffe and the values for GaAs are presented in Table 3.1.

Table 3.1: Varshni parameters of GaAs from compiled data by Ioffe (2004), taken from Schubert. [46]

| Semiconductor | $E_g$ at 0 K (eV) | $\alpha$ ($10^{-4}$ eV/K) | $\beta$ (K) | Validity range |
|---|---|---|---|---|
| GaAs | 1.519 | 5.41 | 204 | T $\leq$ 1000 K |
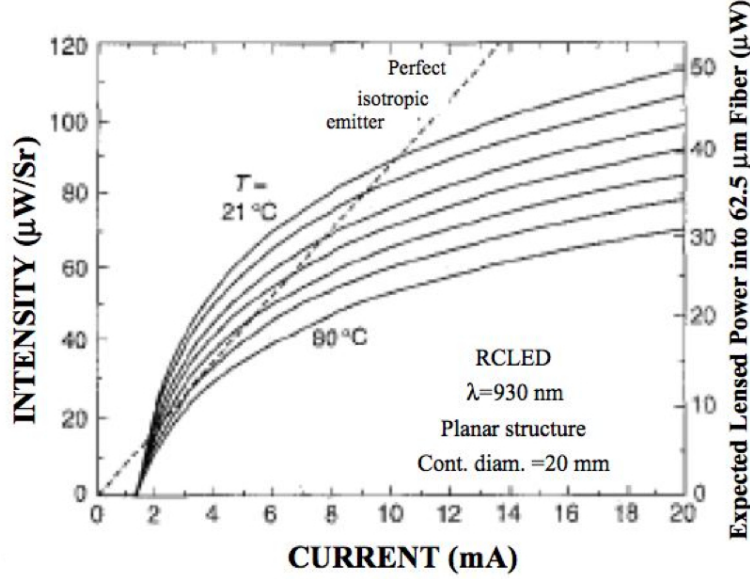


Figure 3.2: Intensity-versus-current (LI) for an RCLED emitting at 930 nm for different temperatures. The traces are measured at the temperatures 21, 30, 40, 50, 60, 70, and 80 $^oC$. Also shown is the theoretical LI curve of an"ideal isotropic emitter", from [48]. As the temperature is increased, the total output power is reduced.

For GaAs, the temperature dependence of the energy gap is approximately linear for temperatures ranging from 20 $^oC \leq T \leq 100\ ^oC$. In RCLEDs, the resonance of the cavity changes with temperature because of the temperature dependence of the refractive index, and the changing thickness of the layers of the distributed Bragg reflectors (DBRs) due to the coefficient of thermal expansion of the layers. The red-shift of the cavity's resonance mode is smaller than the red-shift of the peak wavelength emitted from the AR, due to the change in $E_g$ [58]. There is also a decrease in radiative efficiency at higher temperatures, due to an increase in Schokley-Read-Hall and Auger nonradiative recombination processes [48]. Figure 3.2 shows the measured intensity versus current over temperatures ranging from 21 $^oC$ to 80 $^oC$. Schubert et. al reports a 62% decrease over that temperature range.

*3.2.2  Radiative Recombination Enhancements .*     Radiative recombination is of key importance for light emitting devices. Although both the radiative and non-radiative recombination phenomena always occur, reducing non-radiative recombination and optimizing radiative recombination is, and has been, the ultimate goal for LED designers [46]. Since even the most pure materials will have some native defects, non-radiative recombination can never be totally eliminated. Over many years, through countless investigations, drastic improvements have been made in optimizing the radiative recombination occurrences in semiconductor material, while reducing the non-radiative recombination events. Two technologies include heterostructures and multiple quantum wells, which both confine holes and electrons in close proximity, increasing the probability of recombination. Blocking layers are also used in concert with heterostructures to trap the faster moving electrons in a region closest to the holes.

Quantum wells (QW) are formed by growing materials with smaller energy gaps between layers with a wide energy gap, or heterostructures. QWs are potential well structures with widths smaller than 100 nm. The benefit of QWs is that the small width of the wells increases the recombination rate of the excess carriers due to the descretized status of the well. QWs are embedded within the active region and are often used in concert with several other QW, as depicted in Figure 3.3. This depiction also shows an electron blocking layer. The multiple quantum wells (MQW) are evenly spaced in the center of the active region. These layers have a bandgap much narrower than the other layers in the stack. Due to their small width, single QWs fill rapidly, even under low level injection, and free carriers can accumulate to a level where they surpass the confining boundary and be lost to non-radiative recombination outside of the QW, or recombine and generate a photon with different wavelength. MQW are used to counter this occurrence. The plot in Figure 3.4 shows optical intensity emitted by $In_{0.16} Ga_{0.84} As/GaAs$ LEDs with active regions containing one, four, six, and eight quantum wells (QW), and a theoretical intensity of a perfect isotropic emitter (dashed line) taken from Schubert et. al. [47]. The plots show that although saturation does

electron
blocking
layer

MQW
Active Region

$E_C$

$E_F$

p-type confinement layer

n-type confinement layer

$E_V$
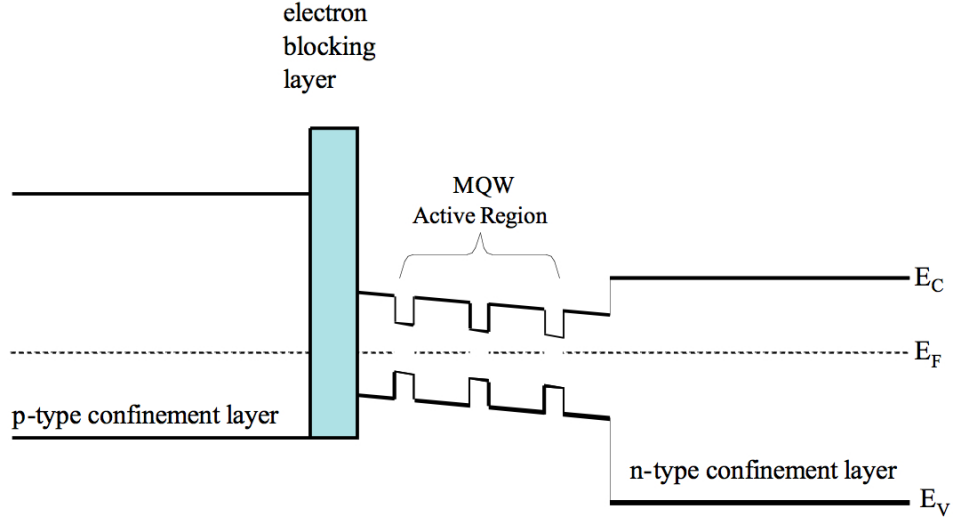
Figure 3.3:    Illustration of an AlGaN current-blocking layer in multi-quantum well LED from Schubert [46]. Three QW are placed in a heterostructure device adjacent to an electron blocking layer. Electrons are injected from the right of the figure and impinge upon the blocking layer and fall into the MQW AR where holes injected from the left of the figure have undergone the same process.

occur, it can be mitigated to a degree by adding QWs. This corresponds to an increase of optical intensity. Generally, no more than 10 QWs are used at a time, so not to make the AR too wide, preventing holes and electrons from traveling into all QWs across the AR. Another characteristic of the quantum well structure is the formation of distinct energy levels within the QW due to the small width. This formation of distinct energy levels within the QW will reduce the spectral purity of the device.

## 3.3    *Current Spreading in Wide Area Devices*

Surface area size is of concern for optical devices, as it has been reported by a number of researchers and observed in several experiments, as the width of a device increases, uniformity decreases. This is especially the case in p-i-n LEDs. Vertically stacked emitters have contacts on the top of the device surface. Contacts can be in the center, making the beam profile an annulus, or they can be around the edge of the surface, leaving an open aperture. In both cases, the metal contact is only as large as necessary to inject current into the device because it blocks part of the beam. For
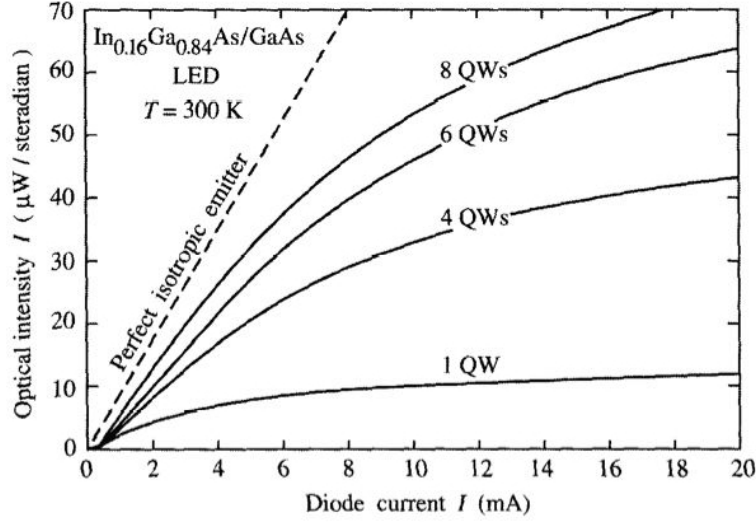
Figure 3.4: Optical intensity emitted by $In_{0.16} Ga_{0.84} As/GaAs$ LEDs with active regions containing one, four, six, and eight quantum wells (QW), and a theoretical intensity of a perfect isotropic emitter (dashed line) taken from Hunt et. al.. The optical intensity is shown to increase as the number of QW increases [16].

bonding purposes, the contact needs to be on the order of 50-150 $\mu$m. To produce a device with sizable output power, the device needs to be fairly large.

As carriers are injected through the metal, they spread out laterally into the layers beneath according to the diffusion length of carriers in that material. Short diffusion lengths cause premature recombination before holes or electrons can reach the full width of the device or even the AR. This is manifested at the surface of the device by a nonuniform beam. This phenomenon has been referred to as current crowding [46]. Current crowding is increased under very high current densities, which are required, in many cases, to drive wide area devices. Wide area devices can handle higher injection currents, dissipate more heat, and have wider active regions, which increase the opportunity for more radiative recombination. This combination leads to a device that emits more power. If injected current cannot take full advantage of the added girth of the device, then the device is less efficient and the total output power will suffer due to current crowding. The introduction of a current spreading layer in the structure stack creates the lateral spreading desired. Figure 3.5 shows current flow from contact layers with and without current spreading layers. Fletcher
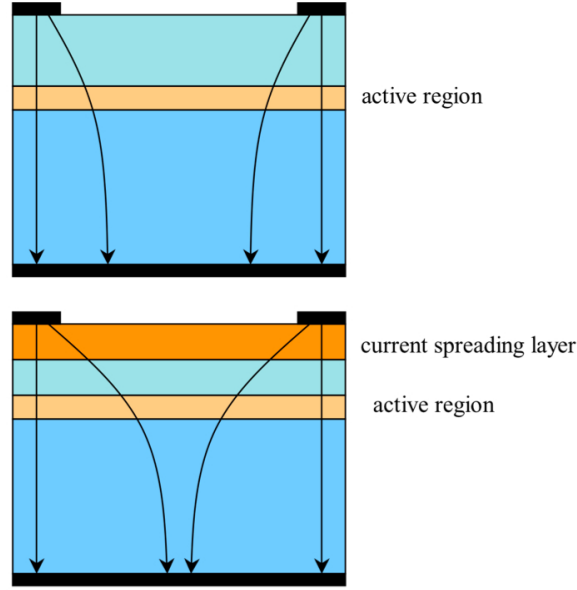
Figure 3.5: A depiction of current crowding in a simple p-i-n structures with and without spreading layer with contacts in the middle and around the edges of the device.

et. al. [10] shows the effect of current spreading on the efficiency of an AlGaInP/GaAs LED. A GaP spreading layer is added to the stack and an increase in the extraction efficiency, by a factor of nearly 8, is observed. Its thickness must be optimized to capitalize on the benefit of current spreading while not suffering from any negative effects that may be introduced to include

- Current spreading to the device edges if the layer is too thick

- Light absorption in thick window layer

- Increased ohmic resistance

- Long growth time could induce diffusion of dopants

Current spreading analysis has produced a model [47] that assumes a constant current density $(J_o)$ under the metal, constant potential over the metal, and a substrate at constant potential. The current density $J(x)$ under the current spreading

layer extending from the contact is found by:

$$J(x) = \frac{2J_0}{\left[\frac{x-r_c}{L_s} + \sqrt{2}\right]^2} \qquad (3.8)$$

for $(x \leq r_c)$, and $L_s$ is the current spreading length found by

$$L_s = \sqrt{\frac{kTtn_{ideal}}{\rho q J_0}} \qquad (3.9)$$

where $\rho$ is the resistivity of the current spreading layer, $t$ is the thickness of the current spreading layer, $q$ is the charge on an electron, and $n_{ideal}$ is the diode ideality factor, typically $1.05 < n_{ideal} < 1.35$. One key factor of importance is the resistivity, $\rho$, of the current spreading layer. A large resistivity leads to a shorter current spreading length and a higher device potentilal. A short spreading length translates into a current density that decreases rapidly as $x$ increases. This is depicted in Figure 3.6 for a square metal contact. This investigation proposes using an Esaki Tunnel Junction (TJ) as a current spreading layer for wide area LEDs. Some background on the TJ is summarized in the next section.

## 3.4   The Tunnel Junction

A typical p-n junction operates as a rectifying device, i.e. current only flows in one direction under forward or reversed bias. Under reverse bias, a reverse current will flow only once a fairly large breakdown voltage $(V_B)$ is reached. With the tunnel junction, this is not the case. The tunnel junction permits current flow at comparatively lower bias voltages under forward and reverse bias conditions. Consider the ideal p-n junction diode I-V characteristic curve shown in Figure 3.7. The breakdown voltage $(V_B)$ occurs at a value that, in most cases, is significantly larger than the damage threshold of the device. For this reason, a reverse current in usable amounts is not realistic in typical p-n junction devices. If $V_B$ could be moved further to the right on the graph, to a point $V_B'$, significant current flow under reverse bias conditions

(a) Linear stripe-shaped top contact

Top view

Cross section view

Current-spreading layer

pn junction

Substrate

$J_0$     $J(x)$

Current density $J(x)$

$x = 0$     Distance from stripe center $x$
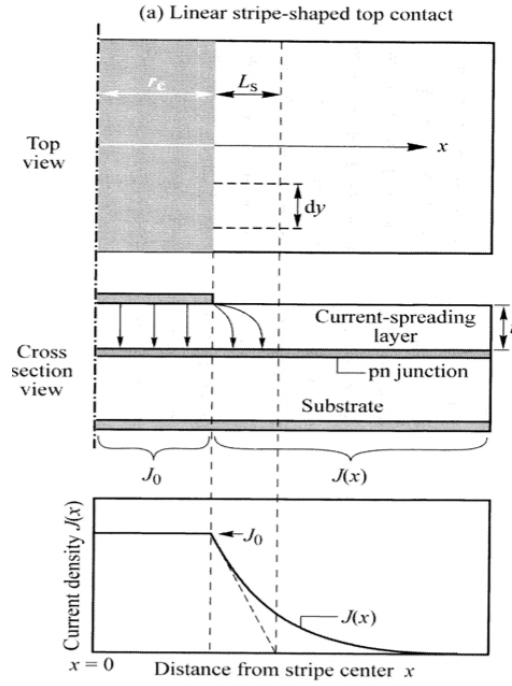
Figure 3.6:     Illustration of current spreading in devices with square and circular contact geometry.  Current density decreases with distance away from the contact increases.
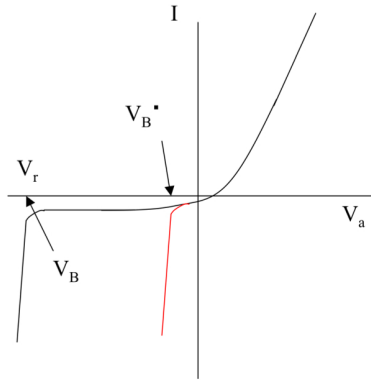


Figure 3.7:     The ideal p-n junction diode I-V curve.  Shown is the typical diode current-voltage characteristic in the upper right quadrant, Quadrant I, under forward bias of $V_a$.  Quadrant III, the lower left qudrant, shows the reverse biased $V_r$ current-voltage characteristic.  At a particular breakdown voltage $(V_B)$, current will increase. Properly doping the junction moves $V_B$ to the left or right of its current location.

3-12

could be obtained without being in jeopardy of causing damage to the device. Since $V_B$ is controlled by the dopant level, it can be shifted by using highly doped layers to form the junction. This is basically an optimization of the Zener effect and has been reported by several researchers [27], [28], [29], [31].

During a study of germanium Zener diodes by Dr. Leo Esaki [9], he noticed that some of the diodes exhibited a negative resistance region under forward bias conditions. Another report with similar results using silicon was made about the same time as Esaki's report [6]. In both cases, a uniquely different diode characteristic curve was the outcome. It was concluded that the negative resistance was a result of the tunneling of carriers across the junction. Figure 3.8 shows the general shape of the I-V characteristic of a tunnel junction [17]. Under forward bias, notice that a local maximum current is achieved before the diode reaches its turn-on voltage and the conventional forward bias current begins to flow.
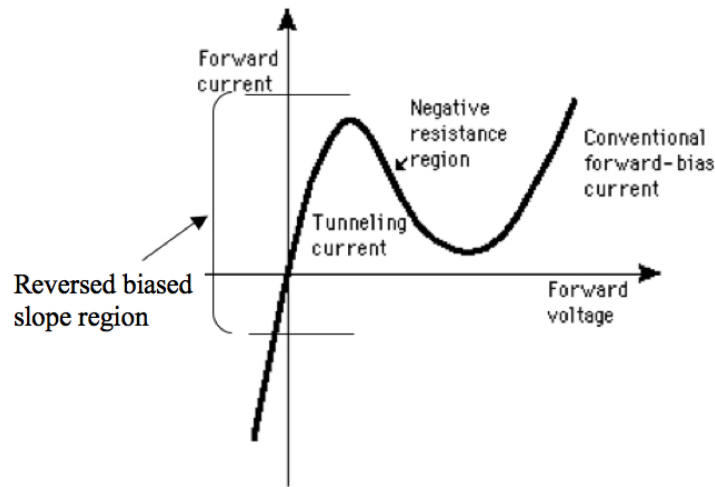


Figure 3.8: The general shape of the I-V characteristic of a tunnel diode. The curve in the upper right quadrant, quadrant I, has a different shape than does the p-n diode. There is a negative resistance region shown, located between two regions of positive current flow. These two increasing, linear curves, are due to the presence of the TJ structure. Also notice that $V_B$ is at the origin, occurring at a much lower voltage than the p-n diode.

For this peak current to reach an appreciable level, two conditions must be fulfilled [15]. First, a sufficiently narrow energy barrier at the junction of the device
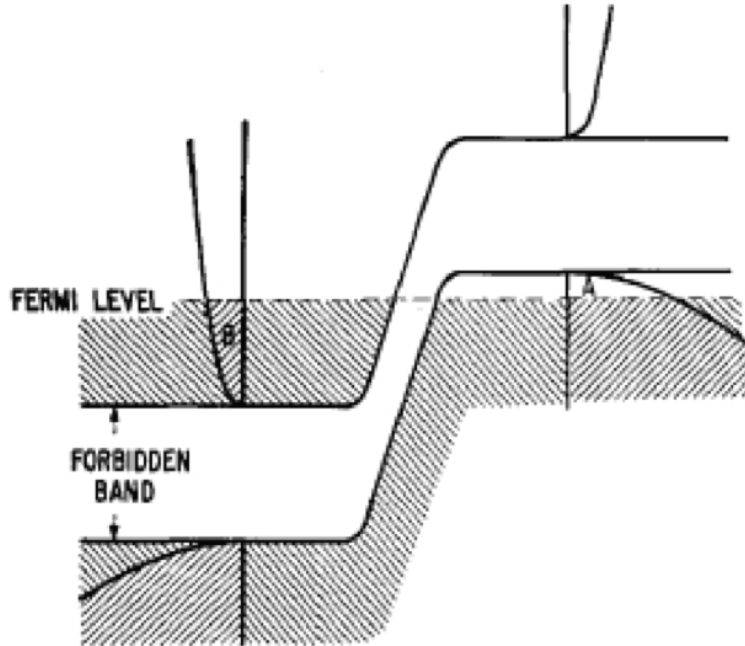
Figure 3.9:    A graphical illustration of the conditions for tunneling. Electrons must be in region B and empty states in region A to create tunneling condition. [15]

must exist. Having a thin energy barrier increases the probability of the carrier penetrating the barrier. Secondly, there must be electrons on one side of the barrier and empty states on the other side in relative proximity. Figure 3.9 shows a graphical depiction of this situation [15]. Region A shows that there are empty states (holes) at the top of the valence band in the degenerately doped p-type material. Likewise, region B shows that there are electrons at the bottom of the degenerately doped n-type material. The dotted line demonstrates that electrons on both sides of the barrier are at the same energy level at thermal equilibrium. When a bias is applied to a diode, the energy band is shifted vertically. The positive terminal will push the band down, while the negative terminal will push the band up.

Diagrams $(a) - (b)$ in Figure 3.10 explain how the tunnel diode characteristic curve is created. Diagram (a) shows that a current exists through the device under reverse bias. There are electrons in the valence band of the p-doped material at a higher energy level than electrons in the conduction band of the n-doped material, i.e.

3-14
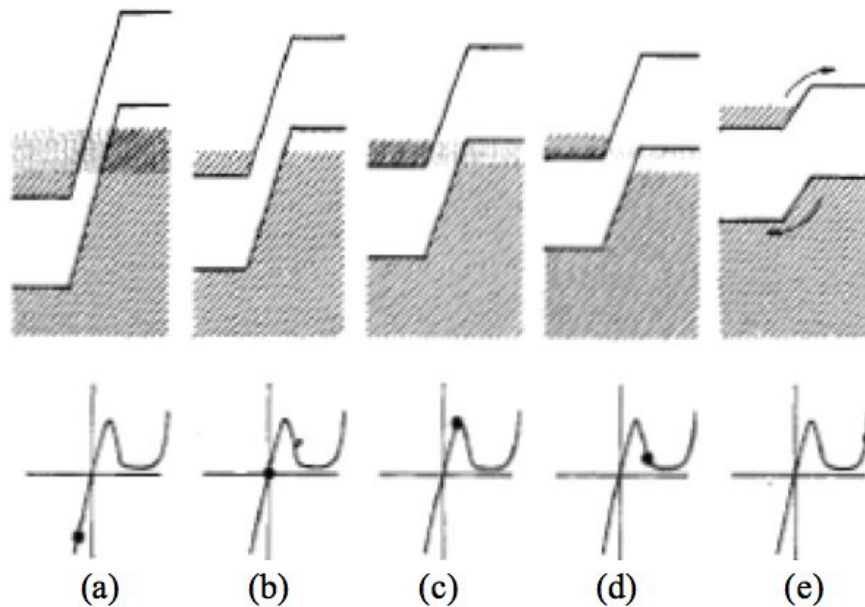
Figure 3.10:    Energy bands of a tunnel junction at various bias levels. (a) shows the junction under reverse bias with holes in the valence band can see electrons in the conduction band, and current flowing. (b) shows now current flow and zero bias voltage. (c) shows a small forward bias voltage and a small amount of current flowing due to a forward biased tunnel current. (d) shows a drop in the forward bias current due to the widening of the forbidden band, and fewer electrons are able to tunnel across this region. (e) shows typical forward bias condition where holes and electrons are swept into the conduction band and valence bands respectively. [9]

there are empty states they can fill. Also, the barrier between them is thin, satisfying a necessary condition for tunneling.

The electrons at the higher potential will tunnel to fill the empty states across the barrier and a current is produced. Diagram (b) shows the device with a 0 V applied. No current will flow as all carriers are at equal levels. Diagram (c) shows a forward bias adequate to produce the peak tunnel current of the diode. Some electrons in the conduction band of the n-doped material can see holes in the valence band of the p-doped material. Again, the barrier is sufficiently thin and tunneling will occur. Increasing the forward voltage past this value will cause a decrease in the

tunnel current as shown in diagram (d). This decrease is due to the barrier widening as the diode energy-bands are flattening and the barrier width is approaching that of the materials energy gap. As the forward voltage reaches $V_{bi}$ of the device, the forward bias current will be produced as the built-in potential has been lowered to a level that allows holes and electrons to move across the junction. This is exhibited in diagram (e). The tunnel current, negative resistance region and the forward bias current are all heavily dependent on the dopant levels of the constituent materials [9].

The slope of the curve in the lower left region of Figure 3.8, quadrant I, is of particular interest when considering the tunnel junction for usage in bipolar-cascade (BC) devices such as BCLEDs. The steepness of the slope under forward bias changes much faster as the dopant is decreased than under reverse bias, meaning, the curve in quadrant I is very sensitive to the amount of dopant in the device, while the curve in the upper right quadrant, quadrant III is not. Having a steep slope means that much larger current at lower voltage levels will flow through the TJ, i.e. a lower resistance junction exist. Operating the device in quadrant I has some advantages that we intend to exploit. In this quadrant, the device is not subject to a dependence on the lifetime of minority carriers, so a current spreading effect results from using the tunnel junction. Additionally, by achieving appropriate doping levels, we can maximize the tunnel current while reducing the input voltage.

Layer doping is the limiting factor in creating these narrow depletion regions. Möller et. al. [32] discuss their results of growing tunnel junctions in GaAs. They used Si as a donor and Be as an acceptor. A low growth temperature was determined to be ideal to prevent Si from being incorporated as acceptors. Under these conditions, a maximum homogeneous doping of $1\text{x}10^{19}$ $cm^{-3}$ for Si and $2\text{x}10^{20}$ $cm^{-3}$ for Be was realized. Möller [32] also confirms, experimentally, that TJ utilization enhanced the uniformity of the beam profiles of wide area devices. By ensuring the maximum number of electrons and holes traverse the entire width of the device before traveling into its depth, the benefit of utilizing multiple ARs can be maximized.
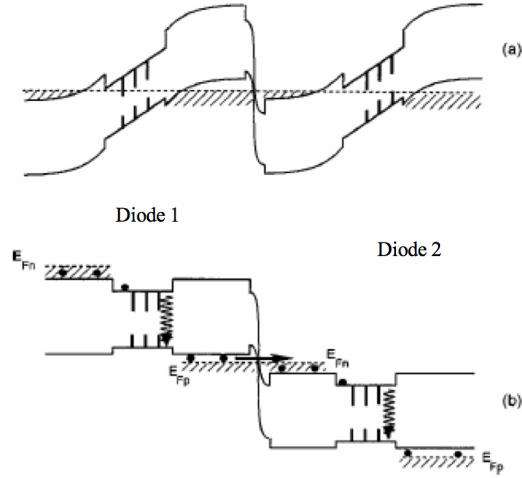
Figure 3.11:    The band structure of the stacked laser diodes separated by a tunnel junction taken from Garcia [13]. Under bias, the bands flatten, and electrons travel toward the active region in Diode 1 and recombine and continue to travel toward the AR in Diode 2. This process is knows an electron recycling.

## 3.5   Multiple Active Regions

Utilization of multiple ARs is not new, as several researchers have used multiple active regions for improved laser power [13] [21] [53] [65]. Figure 3.11 shows the band structure of the stacked laser diodes from Garcia [13]. When no bias voltage is applied, the tunnel junction separates the diodes. Under forward bias, most of the potential is across the diodes, since the tunnel junction is a low resistance structure. Electron transitions from the conduction band of Diode 1 will produce photons. Once these electrons are in the valence band, they are injected into the conduction band of Diode 2 through the tunnel junction. Once in the conduction band of Diode 2, electrons can once again transition and produce additional photons of the same wavelength. This process, in theory, can be extended to additional stages. In some cases, using the stacked stages eliminated the need for highly reflective mirrors in laser diodes. Considerable improvements in total output power using stacked AR have also been reported more recently using 50 $\mu$m VCSELs [21].

## 3.6   Distributed Bragg Reflectors

Since the emission from the source (AR) is omnidirectional, about half of the light is emitted in the direction of the substrate. There are instances where transparent substrates are used to prevent excess photon absorption. A reflective layer can also be inserted between the substrate and the AR. A widely used technique for introducing highly reflective layers is growing distributed Bragg reflectors (DBR) in the device. A detailed discussion of DBRs can be found in several works [2], [7], [64] and only a cursory explanation will be offered here.

DBRs are periodic layered structures that consist of alternating quarter-wave ($\lambda/4$) layers of low ($n_l$) and high ($n_h$) refractive index material [25]. These layers form reflective structures, mirrors, that can be specifically designed to have a certain reflectivity. An effective mirror is one with a large reflectivity coefficient. Light traveling from one medium with refractive index $n_1$, into a second medium with refractive index $n_2$ will experience a reflectivity coefficient ($R$), found by

$$R = \left(\frac{n_1 - n_2}{n_1 + n_2}\right)^2 \tag{3.10}$$

The reflectivity coefficient increases, as the difference between the refractive indices increase. Typically the entrance medium, in which the light originates, is air, which has an index of refraction n = 1, so $R$ becomes

$$R = \left(\frac{1 - n_2}{1 + n_2}\right)^2 \tag{3.11}$$

Since the index of refraction is wavelength dependent, the layer is a quarter-wave thick only at $\lambda_o$. Each high-low index layer pair, also called a DBR pair, forms a $\lambda/2$ thick structure. The $\lambda/2$ thick structure causes the incident energy to be reflected in phase with other incident waves of the same wavelength, creating a condition of constructive interference. By increasing the number of DBR pair, very highly reflective surfaces, with $R = 99.999$ % and up, can be created. To determine the physical thickness of

each layer in the DBR stack, one can use the following equations:

$$d_l = \frac{\lambda_o}{4n_l} \tag{3.12}$$

$$\lambda = \frac{\lambda_o}{n} \tag{3.13}$$

where

$\lambda_o$ is the design wavelength of the energy emitted in air

$n_l$ is the index of refraction of the low index material

$n_h$ is the index of refraction of the high index material

$d_l$ is the physical thickness of the quarter-wave layer

Figure 3.12 [25] show multiple reflections from the DBR surface. These successive reflections are in phase and add constructively to produce total reflections of nearly 100%.

## 3.7  Resonant Cavities

The insertion of two DBR mirrors, one above and one below the AR, forms a resonant cavity (RC) around the AR. LED structures having RCs have been shown to exhibit many advantages over conventional LEDs. The RC, or Fabry-Perot etalon, used in micro-devices increases the spectral purity of LEDs [47]. It also enhances the overall brightness of the emitted energy [47]. Because energy within the cavity is repeatedly reflected, amplification of energy exiting the cavity occurs. RCs lower the injection current requirement to get the same amount of output power from a conventional device. They also narrow the exit cone of semiconductor emitters, which can be as large as $120^o$ for some devices [47]. When DBRs are used to form RCs, the entrance medium is the spacer material between the DBR surface and the AR, which
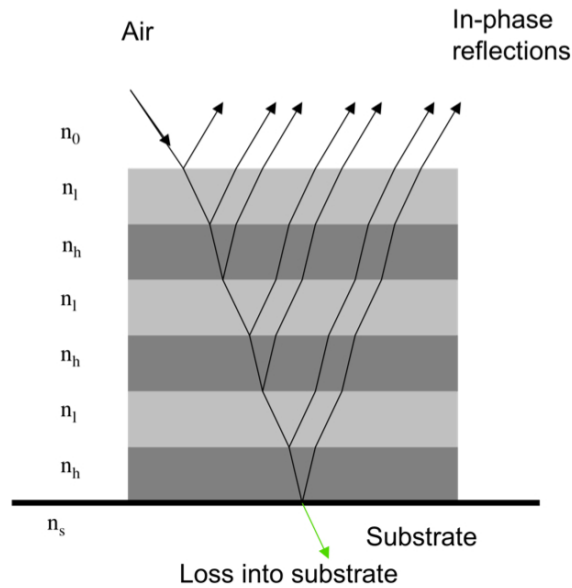
Figure 3.12: This notional DBR stack shows how light is reflected constructively at the junctions formed by layers with high and low refractive indices. The successive reflections add to produce a total reflection by the structure of nearly 100%. Any light that passes through the stack is lost into the substrate [25]. This depiction is of a DBR with air as the entrance medium, which is not the case when the DBR is part of a device. Light is incident from the direction of the AR.
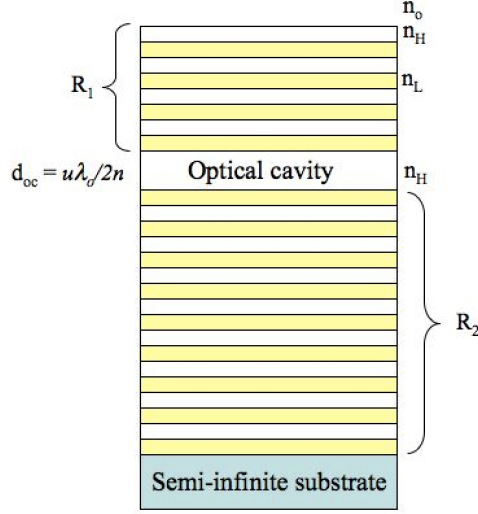
Figure 3.13: Conceptional depiction of a resonant cavity structure. The mirrors are made of high ($n_H$) and low ($n_L$) index of refraction material placed on the top and bottom of the optical cavity, which is also a high index material. The cavity thickness ($d_{oc}$) is an integer multiple of $\lambda/2$, where $u$ is any integer. $R_1$ and $R_2$ are the reflectivities of the respective mirrors. The entire structure is grown on a semi-infinite substrate. This figure is adapted from [25]

is typically a material with a high index, and Equation 3.11 becomes

$$
R_{2N_P} = \left[ \frac{1 - \frac{n_s}{n_{AR}} \left( \frac{n_1}{n_2} \right)^{2N_P}}{1 + \frac{n_s}{n_{AR}} \left( \frac{n_1}{n_2} \right)^{2N_P}} \right]^2
\tag{3.14}
$$

where $N_p$ is the number of DBR periods, $n_1$ and $n_2$ are the high and low refractive indices respectively, $n_{AR}$ is the refractive index of the AR, and $n_s$ is the refractive index of the semiconductor surface on which the multilayer DBR "stack" is grown.

The basic conceptional structure of the RC device is depicted in Figure 3.13. The top DBR is typically of much lower reflectivity than the bottom device. For RCLEDs, which do not require as high finesse cavity as a vertical cavity surface emitting laser, the top DBR typically has a reflectivity $R < 90$ %, where the bottom is nearly 100% [47]. The design of the microcavity is important to maintain and increase the device efficiency.

The optical thickness of the microcavity must be an integer multiple of $\lambda/2$, to ensure that the intensity resonance peak of the emitted energy is appropriately placed within the cavity. The microcavity contains the active region, which is made of quantum well structures. The resonance peak, or antinode, must be co-located with the quantum well region to have the most efficient transfer of emitted energy to the resonance mode of the structure. Figure 3.14 shows a cavity with an electric field intensity standing wave pattern placed at the center of the cavity. The resonance peak (antinode) is located at the AR and nodes are at the mirrors [47]. Shorter cavities, where $u$ is a small integer multiplied by the cavity length, are desired for optimal transfer of the spontaneous emission spectrum to the cavity mode as shown in Figure 3.15. There, one can see the optical mode density for (a) short and (b) long cavities with the same finesse F, and (c) The spontaneous free-space emission spectrum of the active region of an LED. A better overlap between the optical energy and the optical mode density occurs with the shorter cavity compared with the longer one.
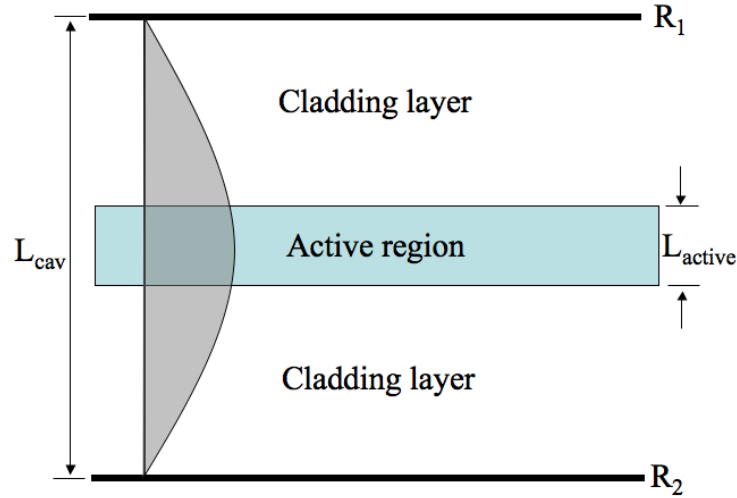


Figure 3.14: A cavity with an electric field intensity standing wave is shown, adopted from Schubert [47]. The resonance peak (antinode) is located at the AR and nodes are at the mirrors $R_1$ and $R_2$. The cavity has a length $L_{cav}$, and an active region length $L_{active}$. This picture was taken from [47].
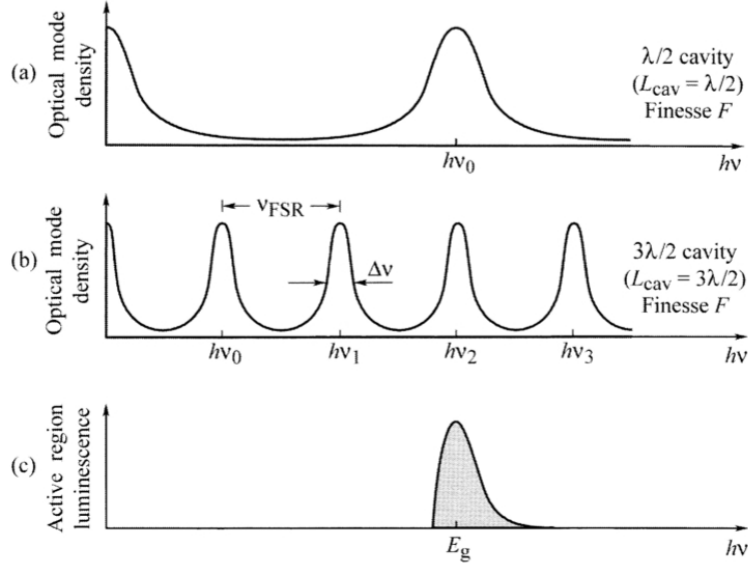
Figure 3.15:    Optical mode density for (a) a short and (b) a long cavity with the same finesse F. (c) The spontaneous free-space emission spectrum of the active region of an LED. A better overlap occurs with the shorter cavity compared with the longer one. This figure was taken from [47]

As $u$ increases, so does the number of intensity peaks that will fit in the cavity. When only one mode persist in the cavity, a larger portion of the intensity peak of the energy can overlap the cavity resonance mode, than occurs when there are multiple cavity modes.  The result is a much more efficient device.  Resonant cavities also reduce the size of the light extraction cone of LEDs. LEDs without resonant cavities have total extraction cones as large at $120^o$. It has been reported in [33] that devices with extraction cones totaling $30^o$ have been built using RCs in LEDs.

## 3.8    Summary

This chapter summarized some the technological developments over the past 100 years that have made the LED a more efficient device. The technologies included in this chapter are those that were utilized in the development of the STREMER. The basic theory behind the issue of current crowding, as well as a mitigation strategy, was presented. The TJ was then discussed and background provided. The use of a TJ, as a current spreading layer for wide area devices, was also presented. The design

of vertical cavity optical devices using DBRs as mirrors was discussed as well. Each of these concepts were considered necessary to design a device for the final remote sensing demonstration, and subsequently, for the HRIS.

# IV. Preliminary Testing and Device Development

## 4.1 Introoudction

This chapter discusses the methodology used in developing the STREMER. The STREMER is a BC-RCLED, which is not a typical LED, but a collection of technologies that improve the operational output of the basic LED. For this reason, several preliminary experiments were necessary prior to settling on a final device design. The purpose of these preliminary experiments was to

- Determine the appropriate growth process for best TJ current vs voltage (I-V) slope under forward bias

  - An abrupt dopant profile is demanded for best TJ characteristic curve.

- Determine the optimal location of the TJ with respect to the ARs.

  - Highly doped TJ are scattering centers and heat sources and could reduce overall device power

- Determine the impact of heat on the resonance peak of the resonant cavity (RC)

  - RC will be designed with a red shifted center frequency in expectation of the red shifted emission spectrum from the InGaAs MQWs. This allows the emission peak to match the cavity resonant peak under normal operation

Some features were also modeled using Crosslight® software, a finite element analysis tool for semiconductor device modeling. Crosslight is composed of a number of computer aided design simulation modules, which simulate the electronic and opto-electronic properties of semiconductor devices. The simulation packages are based on finite element analysis in two and three dimensions. There are a number of physical and numerical models utilized to calculate various parameters describing the performance of the device simulated. The APSYS module, with the quantum mechanical tunneling capability, was used to model the behavior of wide area BC-RCLEDs. APSYS is a general-purpose two dimensional finite element analysis and modeling software program, and was used to generate the following pertinent data:

4-1

- Current versus voltage characteristic

- Band diagrams under various bias conditions

- Spontaneous emission spectrum as a function of current

Because the preliminary testing was essential to developing the final design, a brief summary of the conclusions reached from each test is included. Tests include: 1) TJ growth process investigation, and 2) TJ-AR separation (TAS) determination, to establish an appropriate distance to insert between the TJ and AR to lessen the impact of the TJ on beam uniformity, total output, and wavelength shift.

## *4.2  Preliminary Tests*

To produce an optimal BC device, a quality TJ is key. Once an optimal TJ growth process was identified, it could be integrated into the growth with the other device layers. Fabrication of RCLEDs has been perfected over many years and many standard growth processes exist and were used as a template for this device

*4.2.1  Tunnel Junction Growth Process .*    Six different TJ samples were used for this investigation. All samples were grown by molecular beam epitaxy in a Varian Gen-II system. The various test samples are shown in Table 4.1. A more descriptive layer-by-layer presentation of each sample can be found in Appendix C. The wafers were labeled G2-3255, G2-3256, G2-3257, G2-3258, G2-3259, and G2-3260. Wafers 3255 and 3256 are identical growth runs to test system variation.

To form the TJ, degenerately doped n-type and p-type epitaxial layers were grown on n-doped GaAs substrates at a temperature of 680 $^oC$, which is a typical growth temperature for this structure. For high quality TJs (those with low resistivity) the p-n junction must have an extremely abrupt doping profile, creating a thin space charge region that will increase the probability of quantum mechanical tunneling [9]. Doping levels for the TJ layers are 1 x $10^{20}$ cm$^{-3}$ for the Be doped p-layer and 8 x $10^{18}$ cm$^{-3}$ for the Si doped n-layer. Si becomes amphoteric for dopant levels this large, if this is coupled with growths at high temperatures, a self-compensation

Table 4.1: Device labeling and description of the growth processes, to include adding structures, or altering the vacuum gas flow, and the growth temperature.

| Wafer Number | Growth Variation | Growth Temperature |
|---|---|---|
| G2-3255 | Standard | $575^oC$ |
| G2-3256 | Standard | $575^oC$ |
| G2-3257 | 30 sec As flow inserted | $575^oC$ |
| G2-3258 | 20 Å smoothing layer inserted | $575^oC$ |
| G2-3259 | Remove 3.5 sec As flow after each $\delta$-doped layer | $680^oC$ |
| G2-3260 | Remove 3.5 sec As flow, added 20 Å smoothing layer | $680^oC$ |

of the doped layer can occur. To mitigate these issues, $\delta$-doping was used to establish a high doping level throughout the n-layer. The growth of 10 Å $\delta$-doped layers was repeated 20 times, resulting in a 200 Å n-doped layer. Also, it has been reported that reducing the substrate temperature below 400 $^oC$ controls the self-compensation effect [32], but because this layer is in the AR, it is preferable to grow it at the same temperature as the QWs.

Samples 3255 and 3256 were produced by growing the $n^{++}$ layer directly on the $p^{++}$ layer, resulting in the formation of the TJ. The next sample, 3257, has a 30 sec As flow inserted into the growth. The As overpressure step allows n dopant (Si) to clear out of the chamber reducing the possibility of self compensation in the $p^{++}$ layer. Sample 3258 has a 20 Å undoped smoothing layer added to the structure, between the n and p regions, to enhance the abrupt junction. By adding the smoothing layer, fewer dopants from the degenerately doped n layer will diffuse into the degenerately doped p layer during growth. In the baseline samples as well as sample 3257, a 3.5 sec As flow is done after each 10 Å $\delta$-doped layer is grown, but sample 3259 has these steps removed. The 3.5 sec As flow is done after each $\delta$-doped layer to allow time for the dopants to diffuse into the layer. Lastly, sample 3260 has the 3.5 sec As flow removed and the 20 Å undoped smoothing layer added. These modifications were expected to increase the chances of the formation of an abrupt TJ, thus reducing the

size of the space charge region, which will reduce the resistance of the structure. All modifications were the result of discussions with AFRL/RY personnel [35].

Another modification to the baseline growth process was to vary the growth temperature. Typically, GaAs structures are grown above 600 $^{o}C$ to produce high purity material, several of the growths were at 575 $^{o}C$ to reduce the likelihood of dopant diffusion from other layers. Only devices G2-3259 and G2-3260 were grown at the higher temperatures.

Electron beam (E-beam) evaporation was used to deposit 300 Å Ti, 500 Å Pt, 3500 Å Au, which formed the top p-contact metal. The rear surface of the wafer was evaporated 50 Å Ni, 170 Å Ge, 330 Å Au, 150 Å Ni, 3000 Å Au, which formed the n-contact. These metal compositions are the standard metallizations used at AFRL/RY. Ti and Ni are used as seed layers for adhesion, Au/Ge is a widely used n-ohmic metal alloy, the Pt layer is used as a barrier layer to prevent electromigration, and the gold is the contact surface.

A Tektronix Curve Tracer was used to produce an I-V curve for each device tested from the respective wafer samples. The I-V curves were used to aid in understanding the impact of the variations made during the growth process. The curve tracer itself, produced a linear I-V curve when the probe was placed in direct contact with the curve tracer base. This linear curve is shown in Figure 4.1. This slope is a conductance, and by taking the reciprical, the resistance of the apparatus, is found to be $R_{apparatus} = 1 \ \Omega$.

Processed and tested devices ranged in size from smallest to largest, $50 - 1600$ $\mu$m. The smallest devices were the most resistive, and least affected by the apparatus' resistance, while the large ones (larger than 200 $\mu$m ) were the least resistive and were greatly influenced by the curve tracer resistance. For this reason, only the 50 and 100 $\mu$m devices were analyzed for best TJ slope efficiency determination. Figure 4.2 shows I-V curves for all 50 $\mu$m devices tested. A quantitative comparison revealed that devices from wafer samples G2-3255 and G2-3258 showed the steepest
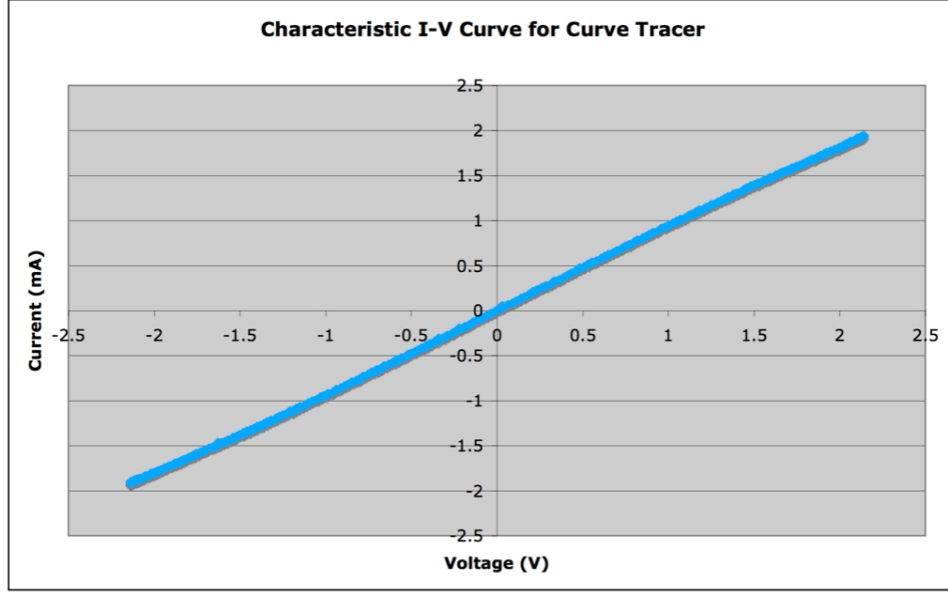
Figure 4.1:    The Tektronic curve tracer I-V curve. This linear I-V curve was produced by the curve tracer probe tip being placed in direct contact with the base.

slope, reflecting that these TJs had the highest probability of quantum mechanical tunneling at the lowest applied voltage. Figure 4.3 shows a plot of the measured I-V curve of a 50 $\mu$m device from wafer G2-3258, and Figure 4.4 provides a closer snapshot of the region of interest, curve-fitted, with the linear regression equation established. A slope of $\sim$0.2 A/V was observed in the measured data.

These TJs were modeled with Crosslight and plots of the unbiased and biased energy bands are shown in Figure 4.5 and Figure 4.6.    The green dotted line in the unbiased band diagram is the Fermi level, and the multiple green dotted lines in the biased band diagram are the quasi-Fermi levels that manifests under forward bias. The I-V curve of the modeled device is shown in Figure 4.7, and it has a slope of $\sim$ 0.2 A/V as well. Even though the curves do not look identical, the slope of the curve is the key for producing a model that is in close agreement with the measured values. Focusing on the voltage range from 0.0 to -0.8 V, the actual slope of the measured data is 0.1672 A/V, and the modeled data has an actual slope value of 0.1847 A/V. Again, each of these values are conductances, and by taking the reciprical, the resistance
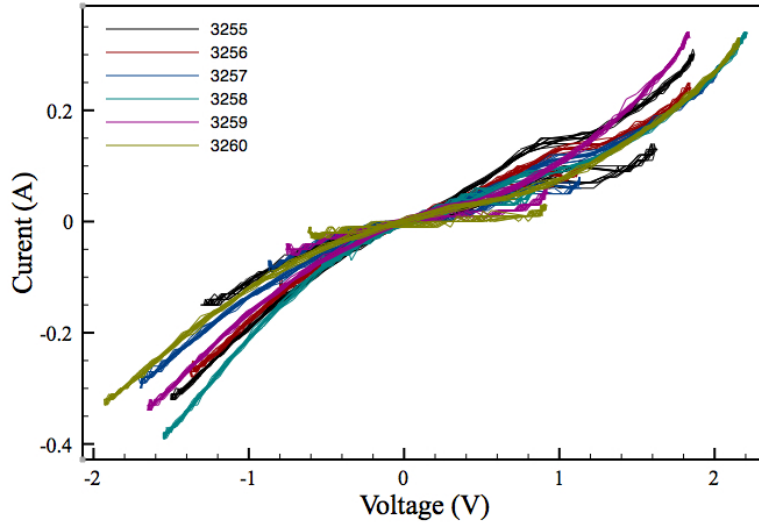
Figure 4.2:     Measured I-V curves taken from all 50 $\mu$m devices tested. Devices from wafer samples G2-3255 and G2-3258 show the best slope efficiency.
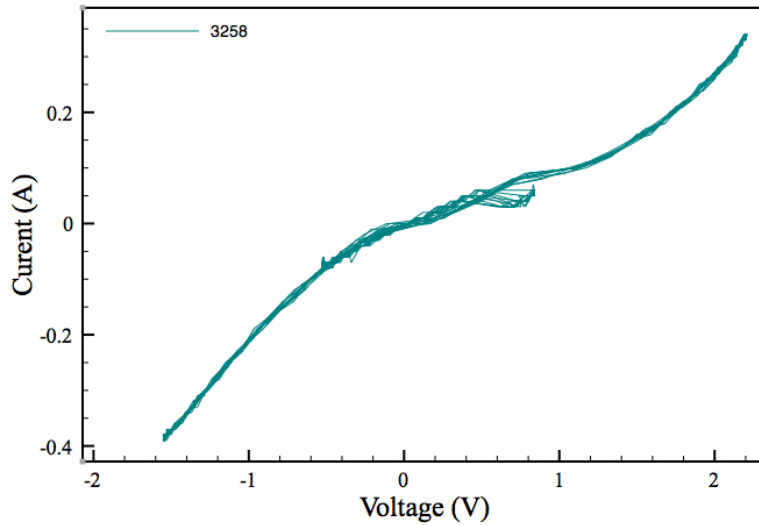


Figure 4.3:     Current-voltage characteristic recorded by the curve tracer. Focusing on the lower left portion of the curve, a slope of $\sim 0.2$ A/V was calculated.
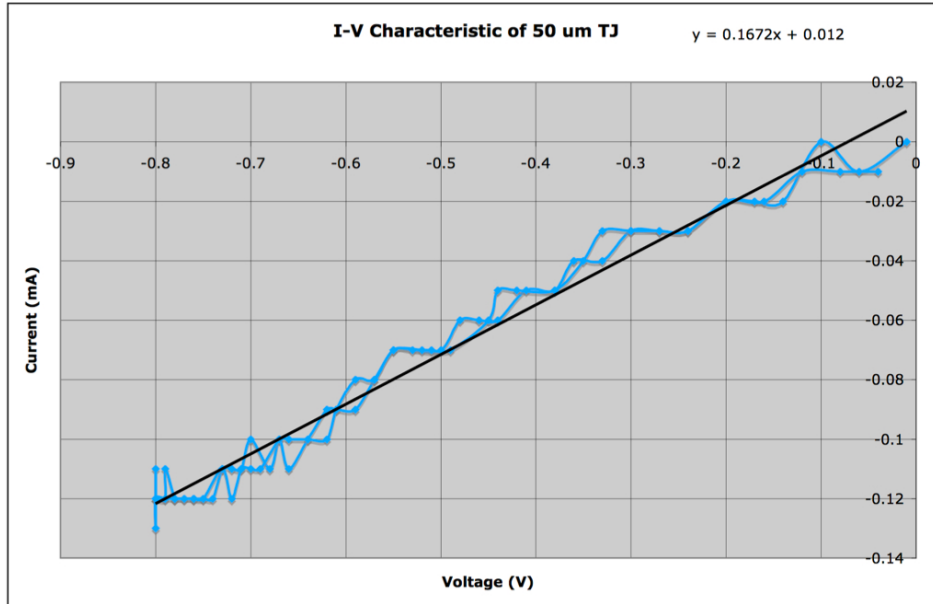
Figure 4.4:    A close up view of the lower left portion of the I-V curve of devices from G2-3256. A slope of $\sim 0.2$ A/V was calculated, and the steepest slope is most desirable. The multiple traces shown in the figure are a result of noise from the curve tracer.
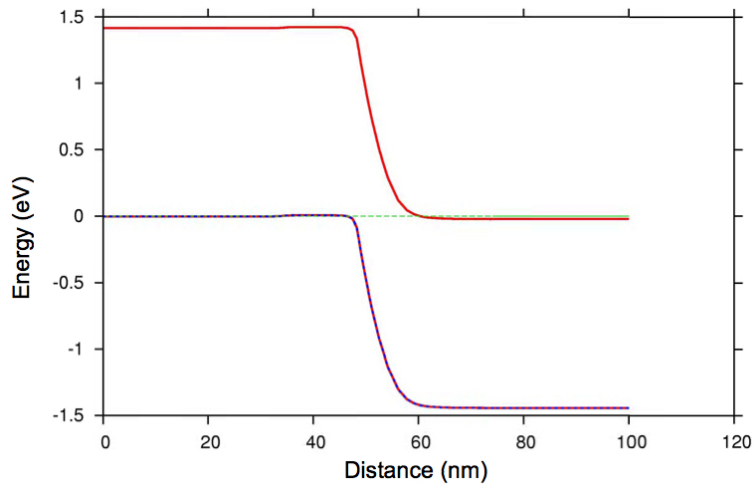


Figure 4.5:    The TJ under 0 V bias condition. The green dotted line is the Fermi level. Degenerate doping brings the conduction band and valence band into close proximity at the junction.
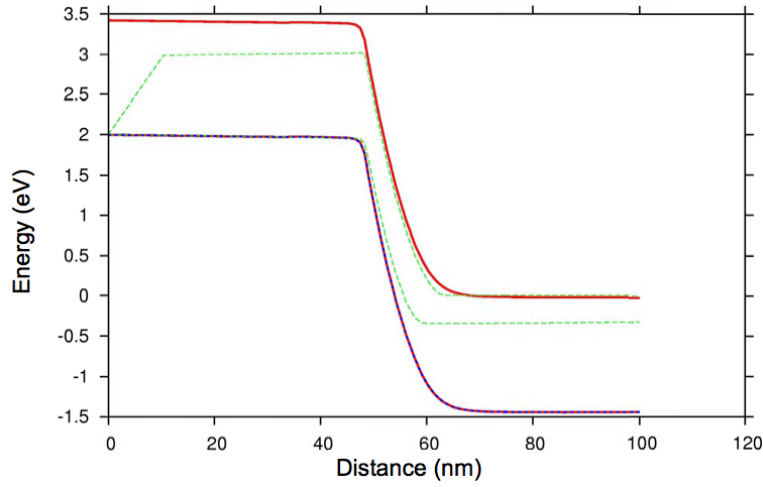
Figure 4.6: The TJ under forward bias condition. The green dotted lines are the quasi-Fermi levels. Under forward bias, the degenerate layers are separated by a thin forbidden energy gap, increasing the probability of electron tunneling.
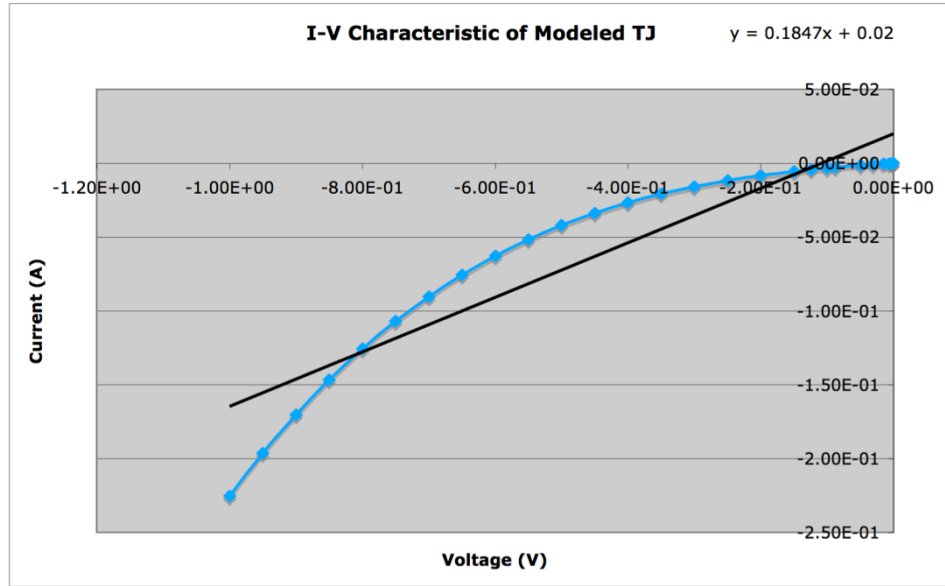


Figure 4.7: Current-voltage characteristic of TJ produced by Crosslight. The overall slope of this curve is $\sim 0.2$ A/V, showing good agreement with measured values.

is found. Therefore the measured resistance $R_{measured} = 1/0.1672 = 5.98$ $\Omega$, and the modeled resistance $R_{modeled} = 1/0.1847 = 5.414$ $\Omega$. Since the measured data was influenced by the curve tracer's resistance, $R_{apparatus}$ must be subtracted from $R_{measured}$, leaving the actual measured resistance $R_{actual} = 4.98$ $\Omega$. The difference between $R_{actual}$ and $R_{modeled}$ is about 8%, which proved to be acceptable for this investigation from subsequent device modeling.

Although the TJs grown for this test are suitable for our application, this series of tests show that the lower temperature devices produce a better slope, under reverse bias, in all devices. From this data, it was determined that G2-3256 and G2-3258 possessed the steepest slope, 0.2 A/V. The TJ growth process used for wafer G2-3256 was selected for use in this application, since the only difference between the devices on the two wafers is that G2-3258 has a 20 Å smoothing layer between the $p^{++}/n^{++}$ junction, suggesting a simpler growth process for G2-3256.

*4.2.2   TJ-AR Separation Layer Thickness Optimization.*   Highly doped layers represent carrier traps in semiconductors, and doping increases the number of imperfections, which lead to an increased number of traps, within the material. An increase in the number of scattering centers increases the probability of Shockley, Reed, Hall (SRH) recombination occurring. It is possible that a large doping concentration induces an increased number of traps and these traps can reduce the total output power. Additionally, TJs are heat sources, since they are resistive to a degree, and temperature greatly impacts device operation, as discussed previously. Finally, the TJ will exhibit a fairly strong electric field that could impact carrier flow. For these reasons we must isolate the TJ and the AR by spacer layers. A TJ-AR separation (TAS) investigation was conducted to determine an optimum location for the TJ with respect to the AR, and determine the impact this separation has on device uniformity, the amount of thermally induced wavelength shift, and device total output power.

Table 4.2:   The distance between the TJ and AR in the respective samples. The TAS layer is measured in Å.

| Wafer | TAS (Å) | Wafer Number |
|-------|---------|--------------|
| 1 | 3045.0 | G2-3263 |
| 2 | 1742.5 | G2-3262 |
| 3 | 250.4 | G2-3261 |
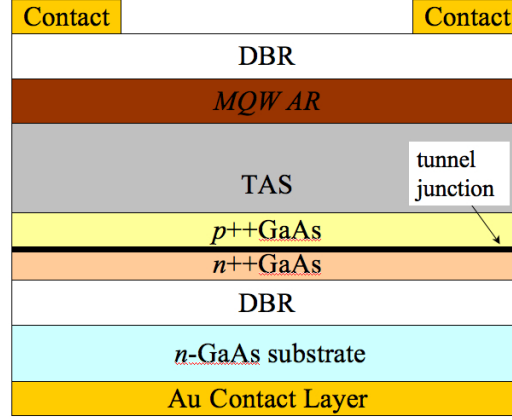


Figure 4.8:   Device layer structure showing the TAS layer in the device. The TAS layer thickness is varied to move the TJ away from the AR.

For these investigations, three different TAS distances were selected and are shown in Table 4.2. Each distance locates the TJ in a node within the RC. Figure 4.8 shows the layer structure, which includes, metal contacts, spacer layers, a MQW AR, the TAS layer, the TJ formed by degenerately doped n- and p-type layers and the GaAs substrate. Also, a set of DBR pairs form a cavity around the TJ and AR.

Data collection was done using a Cascade Microtech probe station with an IR camera mounted to a telescope to record the beam profile. An ILX Lightwave current supply was used to power the devices. In each device, the TJ was placed in a node to minimize carriers from being scattered by the TJ. All devices were 300 $\mu$m in diameter with a 5 $\mu$m wide metal contact ring on the surface, with a 30 $\mu$m section of the contact used for probing. The total cavity thickness of all of the devices used was $4\lambda/2$, or 5568 Å, with $\lambda = 980$ nm and $n_{GaAs} = 3.5$.

Additional devices were fabricated with sizes varying from 80 $\mu$m to 200 $\mu$m, to identify the limit to the effectiveness of the TJ as a current spreading layer in these devices. All of these additional devices were one stage BCLEDs with 25 $\mu$m metal contact layers.

*4.2.2.1 TAS Layer Thickness vs Uniformity .* From previous assessments, the TJ was expected to improve uniformity across the surface of wide area devices over that of the standard PIN LED, i.e. mitigate the current crowding issue. Up to this point, 130 $\mu$m devices had been tested with great success. With larger devices, good uniformity, $\sim 75\%$, was also observed at 300 $\mu$m, as shown in Figure 4.9. This figure was produce using the Spiricon image capture software to measure the pixel intensity across the surface of the device. Analysis revealed that when the TAS
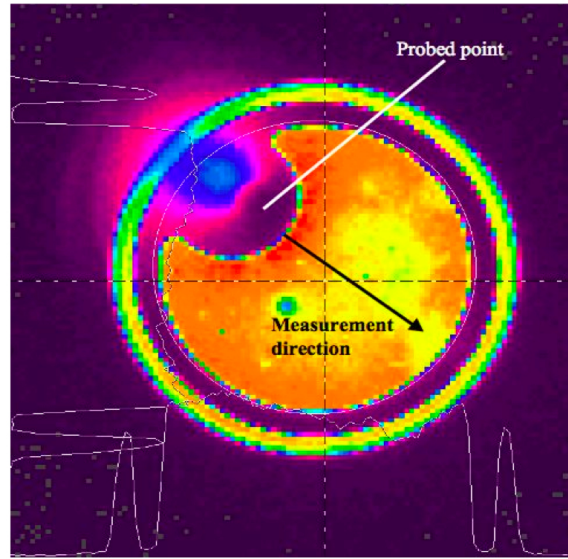


Figure 4.9: A 300 $\mu$m device with a 5 $\mu$m Au metal contact ring. A 30 $\mu$m section in the upper left corner of the picture, quadrant II, is labeled probe point. Measurements were taken, starting at the probe point and moving across the surface of the device. The probe point and the measurement direction are clearly labeled. This picture was taken with a 980M Spiricon IR camera using the laser beam analysis software from the manufacturer.

increased, the beam uniformity across the 300 $\mu$m devices improved. This was expected for reasons stated earlier concerning the TJ as a scattering center and heat
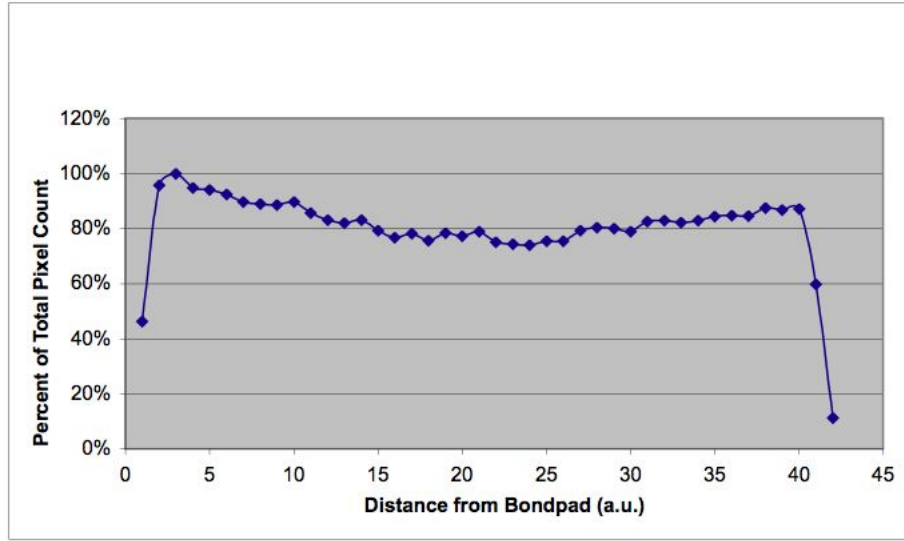
Figure 4.10:    Beam uniformity plot across surface of 300 $\mu$m device. The plot is from data points measured across the device from the 30 $\mu$m section to the opposite side. A pixel intensity variation of 22 % was observed across the surface of several devices.

source. As the scattering center is moved away from the location where a multitude of carriers exist, the less impact it will have on those carriers.

Figure 4.9 shows a photo from the IR camera showing the beam profile of a device from wafer G2-3262, TAS =1742.5 Å. Figure 4.10 shows a plot of the emission across the surface of a device from wafer G2-3262. A 25% drop in power was observed as the surface was measured across the device from the probe point. Wafer G2-3263 had devices that were inoperable and no discernable data was collected, but from the other wafers, several devices were extensively tested. Figure 4.11 shows a picture of a device from wafer G2-3161, TAS = 250.4 Å and Figure 4.12 shows a plot of the beam profile of the same device.   Approximately, a 50 % decrease in pixel intensity across the device is seen due to the thinner TAS layer.
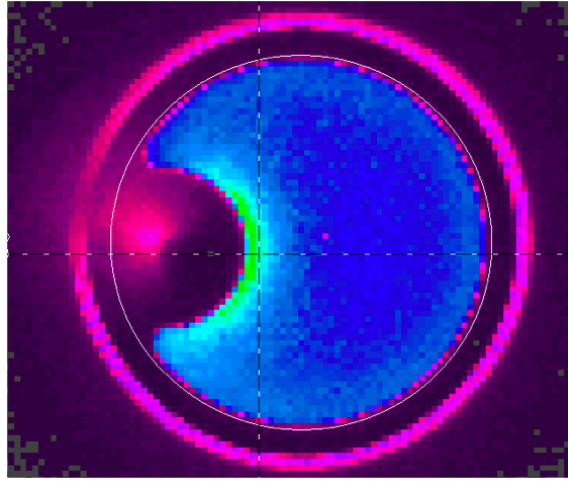
Figure 4.11:    A 300 $\mu$m device with 5 $\mu$m metal contact. The probe point and the measurement direction are the same as previously stated, from the probe point to the opposite side of the device. This picture was taken with a 980M Spiricon IR camera.
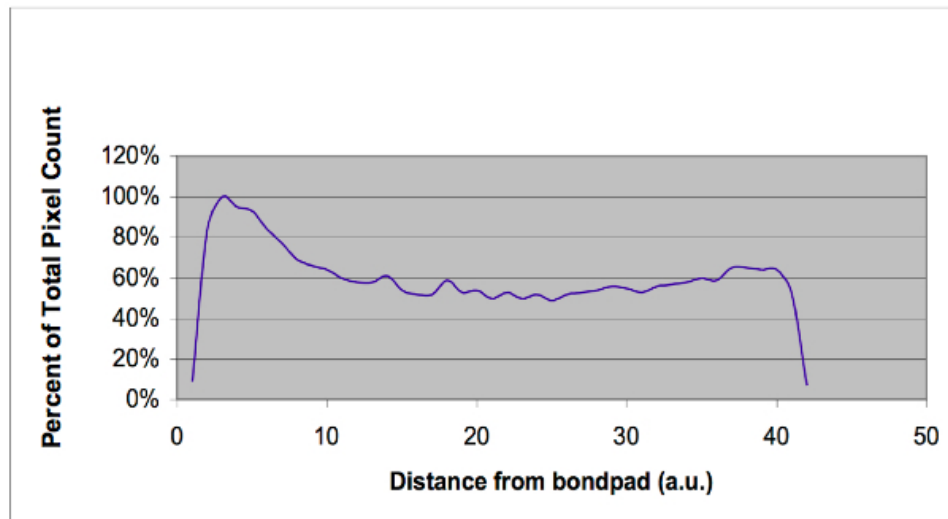


Figure 4.12:    Beam uniformity plot across surface of 300 $\mu$m device. The plot is from data points measured across the device from the probe point to the opposite side. A pixel intensity variation of nearly 50 % was observed across the surface of several devices.

*4.2.2.2 TAS Layer Thickness vs Wavelength Shift.* Since the final device will be a resonant cavity structure, it was necessary to determine the amount of wavelength shift, resulting from heating, under forward bias. The DBR layers of the mirrors forming the cavity increase in thickness, due to heating caused by biasing, and thicker layers will produce a red-shift in the resonant wavelength. The index of refraction also changes due to the increase in heat, but to a lesser degree. Recall from Equation 3.12 that the DBR layer thicknesses equal to $\lambda/4n$. As each layer becomes thicker, so does the optical distance traveled by the reflected energy, causing a phase difference between the incident wave and the reflected wave, resulting in non-constructive reflection, or destructive interference. Hence the cavity is no longer able to sustain a standing wave at the emitted wavelength inside the cavity, i.e. no resonance at that wavelength, but it does have resonance at a longer wavelength, a red-shift has occurred in the cavity.

An investigation to determine the amount of red shift was conducted, and the amount of red shift was observed and noted such that the final device could be designed with a cavity that has a resonance at the expected red-shifted wavelength. These tests were conducted on the same TJ devices used for the TAS determination. Devices were grown with the TJ located in resonant intensity nodes within the, very low resonance, resonant cavity of the devices, created by utilizing two top ($R \sim 0.2\ \%$) and three bottom ($R \sim 1\ \%$) DBR pairs. Numerous devices were tested from wafers G2-3261 and G2-3262, to determine the wavelength shift. The device under test (DUT) is connected to an ILX Lightwave Model LDP 3811 Precision Pulsed Current Source, capable of reaching current levels of 500 mA. A silica multimode fiber (core diameter = 63 $\mu$m) is moved above the DUT in the probe station, to couple a portion of the emission and channel it into a Hewlett-Packard Optical Spectrum Analyzer (OSA). In general, the devices selected for this experiment were the same devices used in the TJ location experiment.

Devices from wafer G2-3261, TAS = 250.0 Å, were damaged at current levels in the 215-220 mA range, and devices from wafer G2-3262 TAS = 1742.5 Å were damaged

at $\sim$ 300 mA, so the injection current levels did not exceed these values for the respective devices tested. Five devices from each wafer were tested and average slopes were found. Figure 4.13 and Figure 4.14 show average slopes for devices from each wafer sample tested, with regression equations for each group showing the wavelength shift, the slope of the line, in nm/mA. The slopes of the regression equations are of the form $\Delta\lambda_0/\Delta I$, expressing the amount of wavelength shift due to current change.
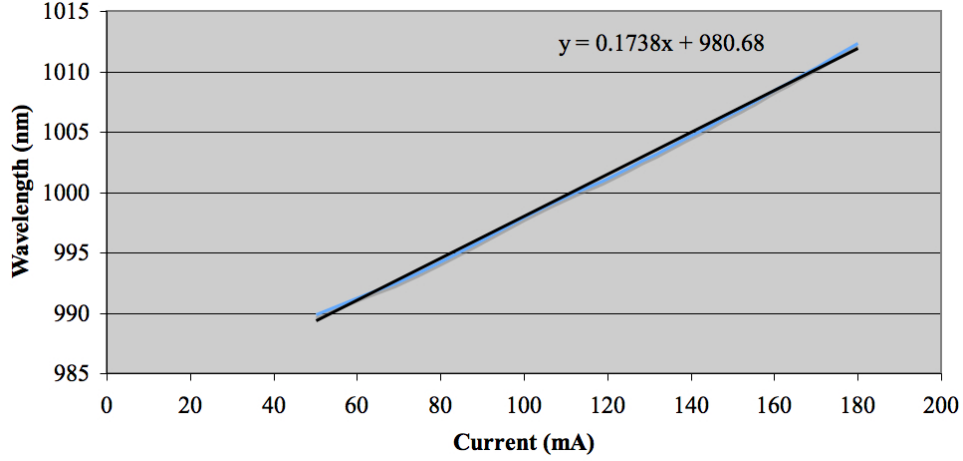


Figure 4.13: The regression plot for devices from waver G2-3261, TAS = 250.4 Å. The average slope gives the wavelength shift per mA of current. For these devices, the amount of shift is $\frac{\Delta\lambda_0}{\Delta I} \sim 0.17$ nm/mA.
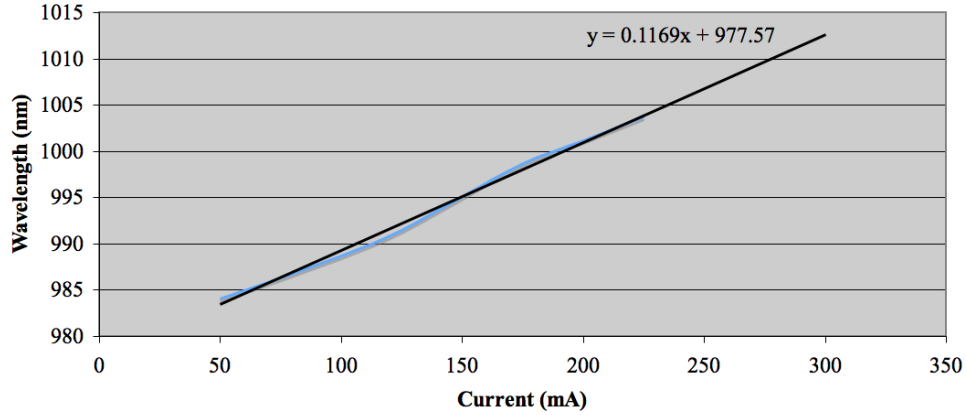


Figure 4.14: The regression plots for devices from wafer G2-3262, TAS = 1742.5 Å. The average slope gives the wavelength shift per mA of current. For these devices, the amount of shift is $\frac{\Delta\lambda_0}{\Delta I} \sim 0.12$ nm/mA.

Modeled data from Crosslight was generated for comparison with the measured values for this experiment as well. One would expect the red-shift to coincide with the increased injection current, as seen from the measured devices. With the model, no discernable differenced in the wavelength of the spontaneous emission was observed with varied current, but with a change in temperature, a very noticeable red-shift occurred. This occurred because no internal heating was used during the simulations. Attention is given to the spontaneous emission rate since spontaneous emission is the light producing phenomenon of interest in LEDs. Figure 4.15 shows plots of the spontaneous emission rates at 300 $K$ and at 373 $K$. The figure shows that
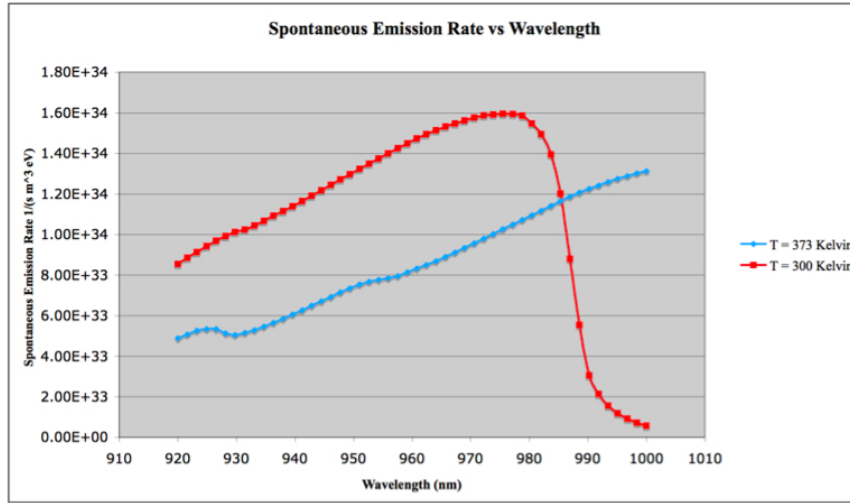


Figure 4.15: Spontaneous emission rate vs wavelength. Plots of modeled data generated at 300 $K$ and 373 $K$, showing a red-shift (increase) in wavelength as the temperature increases. The red curve has a peak at 980 nm and the blue curve is shifted to peak value of $\sim$ 1003 nm. Although this trend is observed from the temperature set by the user at the onset of model execution instead of with increase injection current level, it is consistent with the measured data collected.

a thermally-induced red-shift does occur with an increase in temperature, in this case, it is the temperature established at the onset of the model execution (300 K), and the temperature due to injection current (373 K). A similar shift in wavelength existed in all modeled devices with various TAS values. A temperature increase is the result of an increase in injection current, and at a higher temperature, a shift in the spontaneous emission rate is seen. One can argue that the increase in temperature

4-16

will be larger as the TJ is brought into closer proximity with the AR, and by varying the temperature during successive model executions, the model is effectively modeling the affect of temperature increases induced by larger injection currents, which results in a red-shift in wavelength emitted.

Table 4.3 shows the regression equations and slopes for each set of devices measured. It can be concluded that as the physical separation between the TJ and the AR (TAS) is increased, the amount of red-shift in wavelength emitted from the device reduces. This test concludes that the smallest red-shift of $\Delta\lambda_0/\Delta I = 0.12$ nm/mA occurs due to heating from a device with a TAS = 1742.5 Å, and the wavelength will change according to the regression equation

$$\lambda_0 = 0.1169I + 977.57 \tag{4.1}$$

where $\lambda_0$ is the design wavelength of interest in $nm$, and $I$ is the injection current in A.

Table 4.3:   Identifies the wafer and the calculated slope. The trend shows that when the TJ is moved away from the AR, a smaller red shift occurs.

| Wafer | TAS Thickness (Å) | Equation | $\frac{\Delta\lambda_0}{\Delta I}$ $(nm/mA)$ |
|---|---|---|---|
| G2-3261 | 250.4 | Y = 0.1738x + 980.676 | 0.17 |
| G2-3262 | 1742.5 | Y = 0.1169x+977.57 | 0.12 |

From the modeled data collected, the change in wavelength ($\Delta\lambda_0$) as a function of temperature change ($\Delta$T) is

$$\frac{\Delta\lambda_0}{\Delta T} = \frac{(1003 - 980)}{(373 - 300)} = 0.315 \ nm/K \tag{4.2}$$

A relationship between the change in temperature ($\Delta$T) as a function of the change in current ($\Delta$I) can now be determined:

$$\frac{\Delta T}{\Delta I} = \frac{\Delta T}{\Delta\lambda_0}\frac{\Delta\lambda_0}{\Delta I} = 0.381 \ K/mA \tag{4.3}$$

*4.2.2.3   TAS Layer Thickness vs Total Power.*   The final set of prelim-
inary experiments was done to observe the affect of TAS thickness on the total output
power. A silicon (Si) photodetector was attached to a Hewlett Packard Semiconduc-
tor Parameter Analyzer (HP-SPA) to record the device output power. The detector
was placed directly above the device at a distance about 1 cm. Although some energy
may have been undetected due to the emission cone of the device, it is believed that
over 95% of the energy was captured and measured. The SPA provided power for
the detector and measured the optical energy, which was then converted to a current
by the Si photodetector. A power conversion factor was used to convert the optical
energy to get a power reading.

As in previous testing, several devices were extensively tested from each wafer.
As the TAS was increased, the total output power increased, which suggests that
the maximum TAS of 3045.0 Å is optimal. This could not be confirmed through
testing because devices from wafer sample G2-3263 were inoperable. Figure 4.16
shows average power versus current (L-I) curves for all devices tested. An increase
in total output power of 5.5 mW, from 3 mW to 8.5 mW ($\sim$ 65 %), occured as
TAS increased from 250.0 to 1742.5 Å. Total power data was also generated using
Crosslight®, for the 300 $\mu$m mesa devices at temperatures of 300 $K$ and 384 $K$ and
different TAS values, and plotted in Figure 4.17. Modeled temperature values were
selected based on the relationship described by Equation 4.3, for current levels up to
300 mA, the maximum value used in the TAS layer characterization tests. Figure 4.16
showed the maximum power occurring at $\sim$ 225 mA. Using this value, the expected
junction temperature is $\Delta T = 220$ x $0.381 = 83.8$ $K$. From a careful inspection of
the plots, two observations can be made: 1) holding the TAS constant and varying
the temperature resulted in the most significant increase in output power, $\sim$ 2 mW
increase occurred with each device, an average increase of 40 % per device; 2) holding
the temperature constant and varying the TAS resulted in an increase in output power
as the TAS increased, but to a smaller degree, $\sim$ 10 % increase per device.
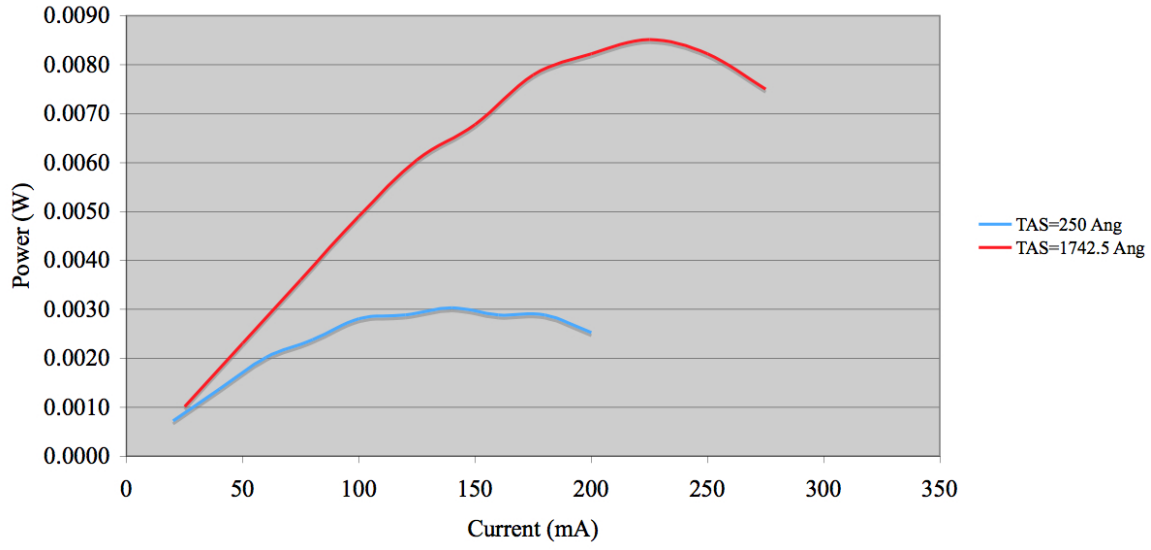
Figure 4.16:    A plot of the total power from two wafer samples with TAS =250.0 Å for G2-3161 and TAS = 1742.5 Å for G2-3262 Å. As the TAS increased, so does the total output power.
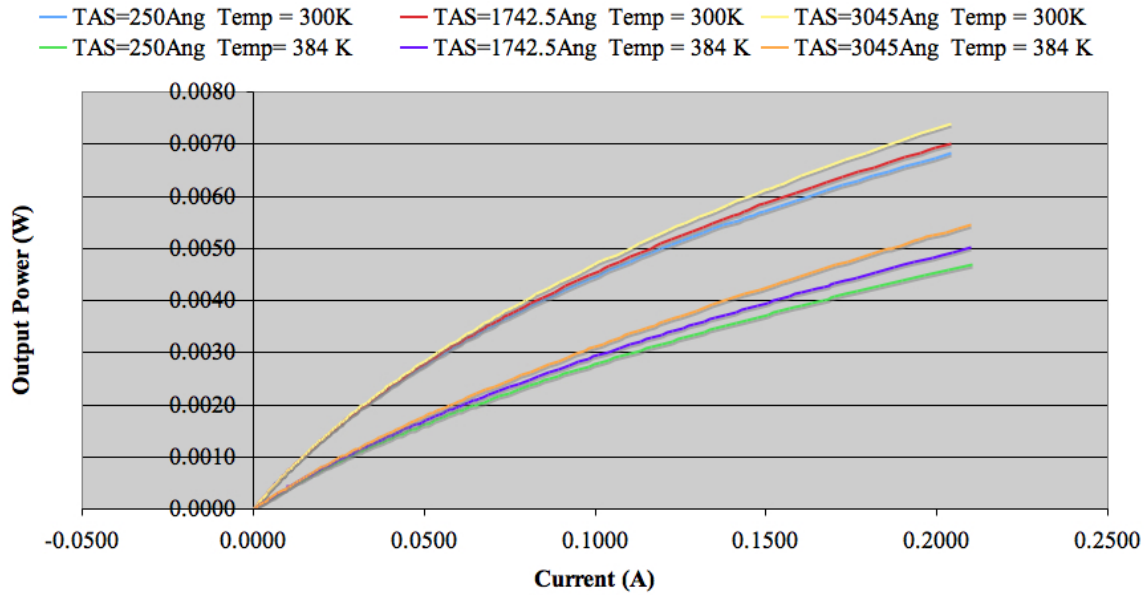


Figure 4.17:    A plot of the total simulated device power of devices at 300 K and 384 K, with TAS at 250, 1742.5 and 3045 Å. As the TAS increased, so does the total output power. Another interesting observation was the significant decrease in output power with the change in temperature, which was on average about 2 mW.

The modeled and measured data consistently express the same message that physical separation between the TJ and the AR improves the total output power from the device. There is a maximum TAS thickness, even though it was not identified during this study. As the TAS layer thickness is increased, the total cavity length will subsequently increase, which will reduce the overlap between the cavity resonant mode peaks and the spontaneous emission intensity, decreasing the overall device efficiency. One must keep in mind the various scattering mechanisms of the TJ, to include heating, electron and hole interband recombination centers (traps), and strong E-field, will impact the total output and, it has been demonstrated that separating the TJ and AR by a substantial distance reduces that impact.

## 4.3    Final Device Design

The data collected and analyzed from the preliminary tests directly lead to the final design of the STREMER. The research goal was to produce a wide area LED with a rectangular geometry having an aspect ratio of 0.006, and a minimum power rating large enough to deliver the needed energy on target for the HRIS. Efficiency is always a concern with semiconductor designs, but in this case, is a secondary issue.

The ideal structure consists of multiple ARs separated by TJs for current spreading and photon recycling. By stacking the ARs the total power is maximized, and as reported by Siskeninetz [53] three AR separated by a TJ made from a 200 Å $n^{++}$ and a 200 Å $p^{++}$ layer, grown one on top of the other, is the maximum number that can be utilized without affecting the emitted power. Adding a fourth stage resulted in a significant decrease in power. It is believed that this drop is due to total thermal impedence. Each active region is 380 Å and made of triple quantum wells, consisting of 60 Å undoped $In_{0.2}Ga_{0.8}As$ layers, separated by 100 Å undoped GaAs barriers.

Testing has shown that heating largely influences the operation of these devices. Equation 4.1 showed the wavelength shifts with increased injection current in 300 $\mu$m devices, and larger injection currents result in a larger shift in wavelength. Although the STREMER is expected to operate under a relatively large injection cur-

rent, possibly on the order of 1 A, it has significantly larger surface area than devices previously tested. The larger area will dissipate more heat, resulting in a smaller shift in wavelength. This, coupled with heatsinking, will greatly reduce the device temperature even more, and subsequently the wavelength shift. Also, packaging techniques, referred to as *epi-side down* mounting, that extract significant amounts of heat, have been reported [24] [38] [41], with semiconductor lasers having injection current values much larger than 1.20 A. Comparison between epi-side up and epi-side down mounted devices show a reduction in wavelength shift of ∼30 % [24] [38] [41]. Additionally, [63] shows significant heat dissipation by using gold-plated heat spreading layer on an etched-pillar device. Previous tests done in support of this work also show a large reduction in thermal resistance with an increase in device size. In-spite of the lack of an actual operating wavelength at this juncture, device design can proceed using $\lambda_0$ instead, as detailed below, and the wavelength can be substituted after further thermal analysis is completed.

DBR mirrors are placed at the top and bottom of the stacked ARs forming a cavity. The top DBR is made of 4 pair of n-doped $Al_{0.5}Ga_{0.5}As/Al_{0.9}Ga_{0.1}As$ layers each separated by a graded layer. The bottom layer is of the same composition but with 20 DBR pairs of n-doped material. The index of refraction of the high index layer, $Al_{0.5}Ga_0.5As$, is $n_h = 3.5$, while the index of refraction of the low index material, $Al_{0.9}Ga_{0.1}As$, is $n_l = 3.2$. From Equation 3.12, and using these indicies, each individual DBR layer thickness, $(d)$, as a function of $\lambda_0$, can be determined:

$$d_h = \frac{\lambda_0}{4(3.52)} = 0.0714\lambda_0 \tag{4.4}$$

$$d_l = \frac{\lambda_0}{4(3.20)} = 0.0781\lambda_0 \tag{4.5}$$

and $\lambda$ is therefore

$$\lambda = \frac{\lambda_0}{n_{GaAs}} = \frac{\lambda_0}{3.5} = 0.284\lambda_0 \tag{4.6}$$
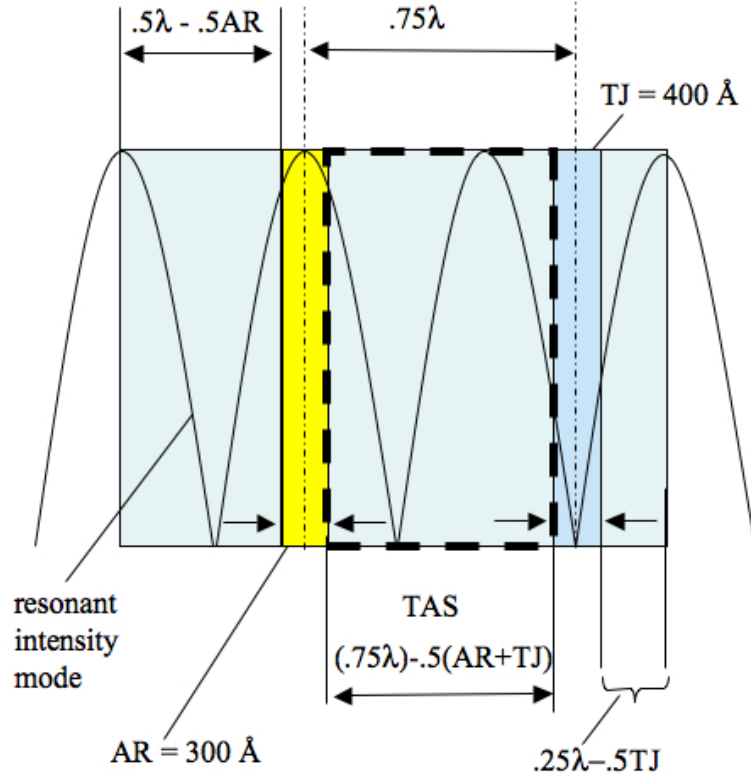
Figure 4.18: Notional depiction of a section of the STREMER microcavity. Shown are the constituents: AR and TJ with the requisite spacing in between for the least TJ impact. The resonant intensity mode is shown, with the AR in an antinode and the TJ in a node. This section is $\frac{3}{2}\lambda$ long.

where $\lambda_0$ is in nm.

For the microcavity to sustain a standing wave, or have a resonance, the wave must have nodes at the mirror surfaces. For this reason, the cavity length must be integer multiples of $u\frac{\lambda}{2}$, where $u$ is an integer number. Additionally, each of the three ARs need to be in a resonance peak antinodes for the most efficient transfer of energy, and each TJ should be placed in a node, since it is a large scattering center. To design the cavity, multiple AR-TAS-TJ sections are used. Figure 4.18 shows one of the AR-TAS-TJ sections used to build the cavity. Each section is designed with a TAS layer that is $\frac{3}{4}\lambda - \frac{1}{2}(AR + TJ)$, to make sure the AR and the TJ is appropriately placed. For a three stage device, three sections are necessary, making the total cavity $\frac{10}{2}\lambda$ long. The full cavity design is depicted in Figure 4.19, and the energy band diagram
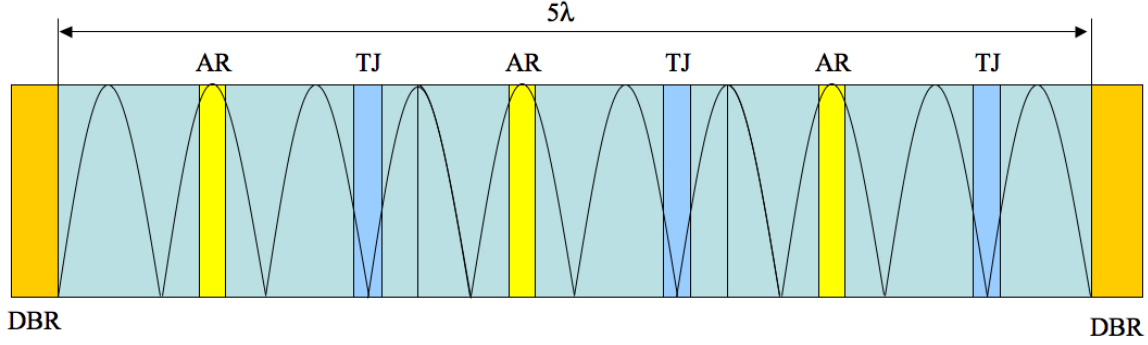
Figure 4.19:    Notional depiction of the STREMER full-sized microcavity. Shown are the constituents: AR and TJ with the requisite spacing in between for the least TJ impact. The resonant intensity mode is shown, with the AR in an antinode and the TJ in a node. This cavity is $\frac{10}{2}\lambda$, or $5\lambda$ long.

Table 4.4:    STREMER design values based on 1 A injection current and no heat sinking.

| $\lambda_0 = 10945$ Å | |
|---|---|
| Parameter | Value (Å) |
| DBR layer - low index | 857.7 |
| DBR layer - high index | 772.7 |
| TAS layer thickness | 1941.9 |
| Cavity length | 15546.9 |

is shown in Figure 4.20. Clearly distinguishable features include the multiple QW and the TJ, which comprise each stage.

Consider the case where the STREMER operates at injection current levels up to 1 A, and using no heat sinking, so the design wavelength is calculated using Equation 4.1:

$$\lambda_0 = \quad 0.1169(1000 \ A) + 977.6 \tag{4.7}$$

$$\lambda_0 = \quad\quad 1094.5 \ nm$$

Table 4.4 shows the values needed to design a basic STREMER without heatsinking, which were also the values used to model the final device. The modeled, final device produced the L-I characteristic shown in Figure 4.21. This L-I curve is for a 200 $\mu$m

4-23
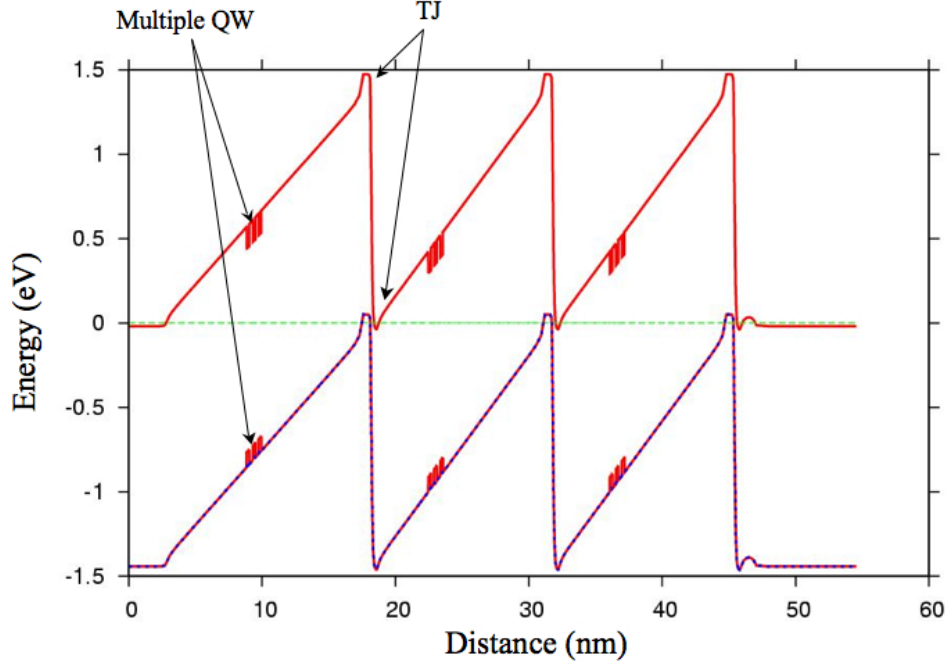
Figure 4.20:    The energy band diagram for the three stage, BC-RCLED STREMER, produced using Crosslight. The multiple QW and TJ, of each stage, is clearly labeled.

modeled STREMER, and shows a drive current up to 500 mA, and output power of ∼ 9 mW. The STREMER is expected to operate under drive currents much larger than 500 mA, and produce much larger output power, due to the larger device dimensions and proper heat sinking. Physical devices, with the same dimensions, but no resonant cavity, were tested with drive currents up to 300 mA, producing output power of ∼ 3.17 mW. Closer inspection of Figure 4.21 shows that at 300 mA, the output power of the modeled STREMER is ∼ 6.5 mW, almost double the measured value, but of the same order of magnitude. It is believed that not modeling the effect of heat, in the model devices, account for the difference between the measured and modeled values.

A qualitative analysis was performed based on reports detailing the demonstrated scalability of vertical cavity devices, in this case lasers, in an arrayed format [30]. It has been reported that devices in an arrayed configuration show linear power scaling, limited, in general, by thermal roll-over [63]. Borrowing from this fact and operating under the hypothesis that it is conceivable that if several of the 200 $\mu$m
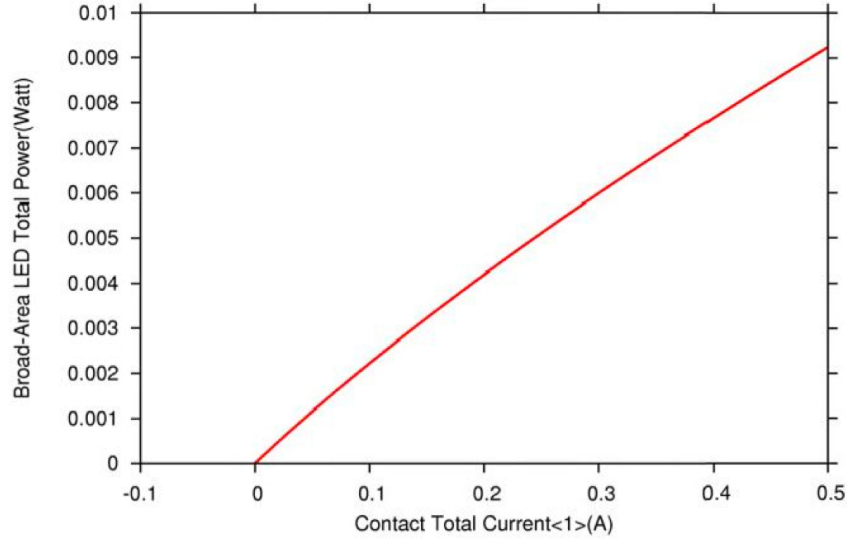
Figure 4.21: Modeled total power output from the STREMER device. This shows that for a 200 $\mu$m device, at a drive current of 500 mA, the total output power is $\sim$ 9 mW.

devices tested, which produced an output power of 3.2 mW, are placed in an array that matches the surface area of a single STREMER section, which is 140 x 10000 $\mu$m, or 0.014 $cm^2$, a power scaling calculation can arrive at a value that is relatively close to what could be expected. Again, heating is an issue, and this calculation does not take that into consideration, and it also assumes uniform injection current. To equal the area of a STREMER section, 35 of the 200 $\mu$m devices would be necessary, and if each produced an output power of 3.2 mW, the total output from a section would be 112 mW. Likewise, a much larger current would be necessary to drive this much larger device. Again using the scaling assumption to perform the calculation, if each device required 200 - 300 mA, the much larger section would require drive currents on the order of 7 - 10 A, which is not unheard of for high-power devices [40].

## 4.4 Summary

This chapter presented the results of several preliminary experiments, which were completed as part of the larger investigation. The information obtained from each of these tests was key to determining the physical characteristics of the final

STREMER device. Several key findings include: 1) having a TAS that physically separates the TJ and AR, but allows the TJ to remain in a resonant intensity node is desirable, 2) growing the highly doped $n^{++}$ and $p^{++}$ layers under low temperature created a TJ with the best slope efficiency compared to other growth processes used, 3) because heat will be generated within the device, a thermally induced wavelength shift will occur in the amount of $\sim 1$ Å /mA of drive current for TAS=1742.5 Å. Since a resonant cavity will be used, it must be designed to accommodate that shift, 4) the total output power is directly proportional to the TAS, 5) it is theoretically possible to produce 140 x 10000 $\mu$m STREMER sections with output power levels of over 100 mW.

For an illuminator to be suitable for the HRIS, it needs to be designed and fabricated as follows: TJs should be used as current spreading layers to prevent current crowding that reduces the total output power from the device; multiple AR, separated by TJs, are needed to increase the total output power from the device; the layers forming the TJ should be grown at 575 $^o C$ for best TJ characteristic slope under reverse bias; the TAS should be 1742.5 Å , or about $\frac{3}{4}\lambda - \frac{1}{2}(AR+TJ)$ , which allows the TJ to be placed in a node, and provides adequate separation between the TJ and the AR to minimize the affect of the TJ on the total output power and the uniformity of the device; the cavity needs to be designed to sustain a resonant wavelength that is the result of a thermally induced red shift. By adopting these characteristics, an optimized STREMER can be developed to meet the requirements of the imaging system.

# V. Final Experimentation

## 5.1  Introduction

This multi-faceted research effort, which includes semiconductor device design, development, optimization and fabrication, in addition to optical beam train design, and remote sensing principles, culminates in a remote sensing demonstration that brings all facets together. This demonstration is a proof-of-concept experimental mock-up of the HRIS system, involving an illuminator and one sensor, an IR camera. Future demonstrations can be done with the second camera integrated into the setup, as well as utilizing the image-processing algorithm. The purpose of this demonstration was to show the ability of wide area LEDs to deliver sufficient energy 5000 cm down range to a target, under ambient lighting conditions, and collect the reflected energy from the target with a collocated sensing device, an IR camera. In addition to the remote sensing demonstration, STREMERs, of the BCLED variety, were fabricated and characterized, to assess their total output power and the beam uniformity. Before final testing could begin, the required energy-on-target and the optical telescopes, for the camera and the source, were determined. The next section reviews the process for calculating the source size and designing the source delivery and detector receiving telescopes.

## 5.2  Pretest Calculations

For the final demonstration, a source of adequate power was needed to deliver the energy to the target, which would produce a target return signal at the camera's focal plane large enough to be detected. The source power calculation was discussed in Chapter 2. Likewise, to deliver the energy to the target, a source telescope was necessary to shape the beam to the requisite configuration. Also, a detector telescope was needed to collect the return energy for the IR camera and the process used to design both telescopes is presented.

Table 5.1 shows some commercially available, high-power infrared LEDs, along with their rated power levels. The device manufactured by Opto Technology boasts

Table 5.1:  High powered infrared LEDs and their manufacturers. The OSRAM was selected for usage in this investigation.

| Manufacturer | λ (nm) | Output Power(W) | Comments |
|---|---|---|---|
| Opto Technololgy | 870 | 9 | 9 chips (5A) |
| Vishay | 950 | 0.035 | 100 mA drive current |
| OSRAM | 940 | 0.500 | 500 mA |
| American Bright LED | 850 | 0.282 | 500 mA drive current |

an output power of 9.0 W, which is by far the largest power level in Table 5.1; however, this device is a collection of smaller devices, which could present a problem with image processing. At the projected distance, the illuminator is magnified to the desired spot size, and if many smaller devices are used to construct a single device with a large output, the distance separating the individual smaller devices could manifest itself in the magnified stripe delivered down range. The projected distance between the individual devices could be on the order of the separation between successive projected stripes, which could cause difficulty in processing returned signals.

All choices presented in the table are viable, but the OSRAM device was selected for use in this investigation because it has relatively high power and was readily available. The OSRAM device is also a collection of smaller devices, interconnected to result in a single device with a larger total output power. The same potential problem discussed with the Opto device applies to the OSRAM device as well. By choosing a device that has a much larger power rating than needed, the range of the system can be extended beyond 5000 cm, however, for this investigation, the 5000 cm range will be used.

*5.2.1  Telescope Design .*    For the remote sensing demonstration, a Spiricon Laser Beam Diagnostics infrared camera, model SP-980M, was used to capture and measure the energy delivered to the target. This particular camera has an interline transfer readout with a spectral response of 190-1100 nm, typical of silicon photodetectors. A high pass filter, with a cutoff wavelength of 800 nm, was used to narrow

Table 5.2: Parameters of the beam train for the CCD camera. A two-optic telescope was needed to capture most of the energy reflected by the target. From the POV of the detector, the detector is magnified by Optic #1 then reimaged and magnified by Optic #2, to deliver the appropriately sized spot on target.

| Parameter | Optic #1 | Optic #2 |
|-----------|----------|----------|
| Magnification | 10 | 625 (666.7) |
| Lens Diameter (cm) | 2.54 | 5.08 |
| Focal Length | 2.54 | 8 (7.5) |
| Object Distance (cm) | 2.8 | 8.01 (7.51) |
| Image Distance (cm) | 25.4 | 5000 |
| Image Height | 4.8 | 3000 (3200.2)) |

the noise producing energy spectrum received at the detector. A data sheet for the camera, giving key information about the camera, can be found in Appendix B.

A two-lens optical system (telescope) was used to achieve the desired FOV at the target, down range from the camera. Table 5.2 lists the details of the camera's telescope. The parenthetical numbers are the actual values calculated, but are not used since finding optics with the exact value was not possible in some cases. In this instance, choosing optics with features that surpass the calculated value was more than adequate.

To design the proper beam-train for the camera, a common design technique was used. The smallest dimension of the camera's detector was imaged at the target distance, with the same target dimensions. The detector's dimensions are 0.65 x 0.48 cm$^2$. Since the smallest side is 0.48 cm, it was used to calculate the beam-train needed to image a target 3000 cm long. A depiction of the camera's telescope is shown in Figure 5.1. The first stage of magnification utilized Optic #1 (O1), with a magnification of M =10, which magnified the detector's smallest dimension to 4.8 cm. This magnified real image (RI) became the object for Optic #2 (O2), which had a magnification of M= 625. A final image height of 3200.2 cm at a distance of 5000 cm using the second optic (O2) was achieved.

In order to capture as much of the emitted energy from the source as possible, a mixture of refractive and Fresnel lenses were needed. The OSRAM sources have an
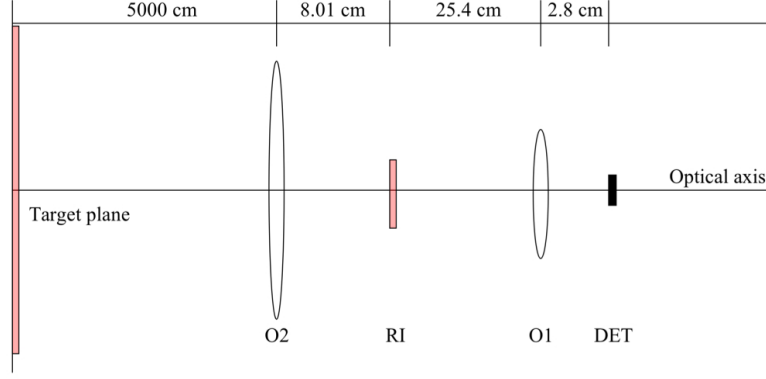
Figure 5.1: Notional telescope for the IR camera. Shown are the optics (01 and 02), the image (RI), the target plane, and the optical axis. The distances between each is also noted. The camera is represented by DET.

exit cone of $120^o$, and a half angle cone of $60^o$. This angle restricted the effective focal length (EFL) of the lens that could be used to capture the energy from this source. In order to capture all of the energy exiting the device in the full cone, a Fresnel lens, with an $f/\# = 0.2$, EFL $= 5$ cm, and diameter, D $= 25$ cm, was used. The Japanese supplier, Nihon Tokushu Kogaku Jushi Co., LTD, was selected to provide the Fresnel lens. Figure 5.2 shows a notional depiction of the source's telescope. The radiated energy comes from a source with dimensions, 1 x 1 mm$^2$, and will travel from the source to the Fresnel lens (O1), which couples the energy into the source telescope. By placing O1 at $S_o \sim 6$ cm away from the source, the maximum half-angle emission captured is $\sim 65^o$. The source is then re-imaged at a distance, $S_i$=30 cm, from O1, and magnified by a magnification of $M_1$=5. The real image (RI) travels a distance $S'_o$ to a cylindrical lens (O2). Lens O2 magnifies RI in one dimension, by a magnification factor ($M_{stripe}$), and that image is located at the target plane and has the desired length of 3000 cm.

The telescope magnification, $M_{stripe}$, is determined by

$$M_{stripe} = \frac{y_i}{y_o} \tag{5.1}$$
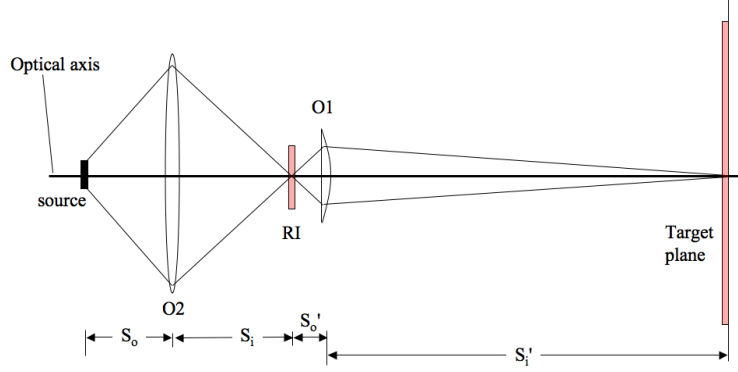
Figure 5.2: Illustration of the telescope designed to deliver source energy to the target plane at 5000 cm down range. The spot size at the target is 18 cm x 3000 cm.

where $y_i = 3000$ cm, the length of the stripe at the target, and $y_0 = 0.5$ cm, which is the source dimension magnified by $M_1$; this ratio produces a magnification, $M_{stripe} = 6000$. The focal length of O2 ($F_{O2}$) needed to produce the appropriate stripe is determined by

$$F_{O2} = \frac{S_i'}{M_{stripe}} \tag{5.2}$$

When the distance to target, $S_i' = 5000$ cm, the object distance of the cylindrical lens needed is $S_0' = 0.83$ cm. The final telescope magnification, $M_{scope}$ is the ratio of the source dimension and the final stripe length, or $M_{scope} = 30000$. Although $S_0'$ needs to be 0.83 cm, finding a commercially available cylindrical lens with this focal length was not possible. A focal length that is shorter than this will provide the necessary magnification, so the actual value of $F_{O2}$ used was 0.7 cm. A second cylindrical lens with an EFL = 138.9 cm was needed to magnify the new image of the source (0.5 cm) to produce an image at the target with a width of 18 cm (M = 36). A thorough search of the major optics suppliers, to include Thor Labs, Melles Griot, and Edmunds Optics was not fruitful. A cylindrical lens to meet this requirement would have to be specially made and this was a viable option. A suitable substitute was to measure the power delivered to the target at the range of interest, and calculate

the irradiance delivered, then, compare it to the irradiance required for detection. Table 5.3 summarizes the details of the source telescope.

Table 5.3:    Parameters of the beam train for the COTS source. A two-optic telescope was needed to capture most of the energy from the source with an exit cone of 120$^o$.

| Parameter | Optic #1 | Optic #2 |
|---|---|---|
| Magnification | 600 | 5 |
| Lens Diameter (cm) | 5.08 | 25 |
| Focal Length (cm) | 0.83 (0.7) | 5 |
| Object Distance (cm) | 0.83 (0.7 | 6 |
| Image Distance (cm) | 5000 | 30 |
| Image Height | 3000 (3200.2) | 5 |

For the STREMER, no beam train could be designed using standard off-the-shelf glass optics that would capture all optical energy. The largest available lenses were 2" (5.08 cm) in diameter. Since the STREMER is about 3 cm long, a 2" optic is not a possible solution, but the Fresnel lens is a viable option. Additionally, typical LEDs have emission cones of 120$^o$, and a resonant cavity could be used to redirect the emitted energy into a smaller cone. If the RC can produce an half-angle exit cone of less than 12$^o$, then the Fresnel lens could be used to achieve the appropriate stripe dimensions. RCs that produce exit cones as narrow as 30$^o$, 15$^o$ half-angle, have been reported [33].

## 5.3   Test Equipment

All device testing was accomplished in the Test and Instrumentation Laboratory at AFRL/RYDP. A Summit 9600 thermal probe station by Cascade Microtech was used to probe all devices tested. An HP SPA was used to provide power to the devices in the probe station and the photodetector. This overall test setup is shown in Figure 5.3. Two current sources were used, including the ILX Lightwave LDP 3811 precision pulsed current source, which produced a drive current up to 500 mA, and a Lumina Power LDD600 current controlled current source, producing a drive current up to 40 A. A Keithly 197 Auto-ranging microvolt digital multimeter (DMM)
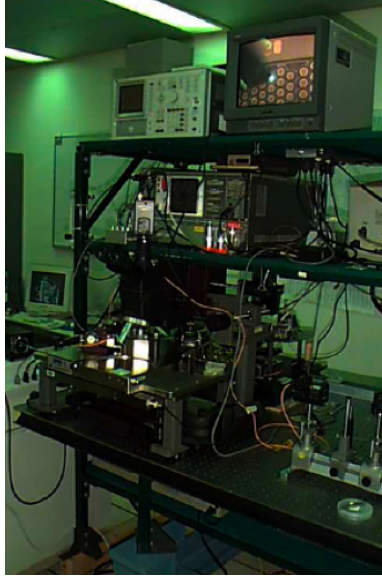
Figure 5.3: Cascade Summit probe station used for all characterization experiments. The probe station was used in concert with an ILX Lightwave current source and an HP-SPA.

was used in conjunction with a Melles Griot SL1007 integrating sphere, as shown in Figure 5.4, to measure the total output power of all devices.

A Spiricon 980M IR camera was used to capture the return signal from the target and record the intensity. The camera was connected to a Dell PC running the Spiricon laser beam diagnostic software and to the computer monitor. The diagnostic software performed photon counting, where the total output power level is displayed as the total number of pixels energized on the camera CCD array. Neutral density filters were employed to prevent camera saturation, which enabled more accurate readings. The Spiricon 980M IR camera is shown in Figure 5.5 and Figure 5.6.

A shroud was placed over the camera to simulate a protective housing that may be used in a fielded version of the system. This protective housing would provide added shadowing for the IR camera, further reducing the background noise signal by limiting the amount of extraneous radiation coupled into the telescope, making the collection optic the only telescope entry point. All glass lenses were purchased from Thor Labs and the acrylic Fresnel lens, shown in Figure 5.7, was purchased from RHK
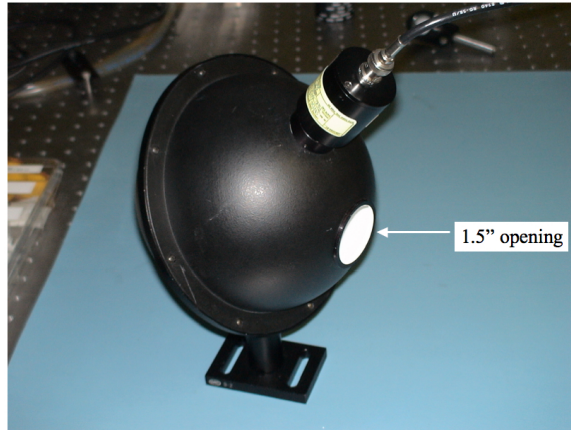
Figure 5.4: Melles Griot 6 integrating sphere with 1.5" opening. This sphere was used for total power tests.
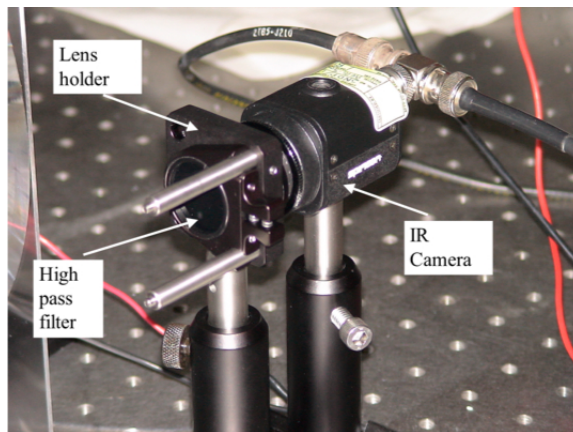


Figure 5.5: Spiricon 980M IR camera with an 800 nm high pass filter in place covering the open aperture of the camera.
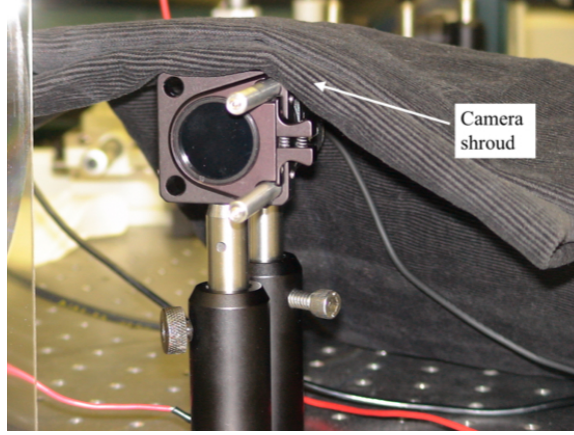
Figure 5.6:    Shrouded IR camera and 800 nm highpass filter. The shroud simulates any housing that would hold the camera in an actual fielded system. The shroud (or housing) would block additional background light.
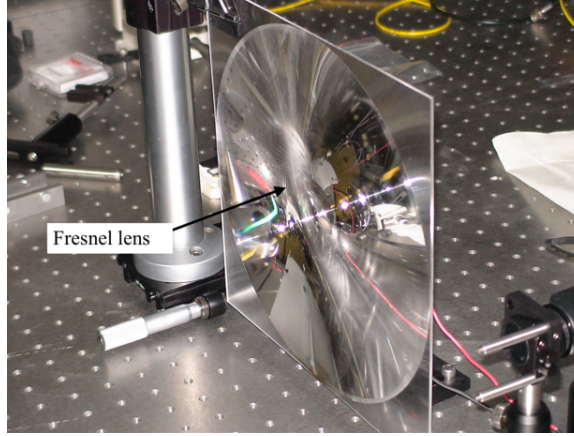


Figure 5.7:    Fresnel lens with D = 25 cm and EFL = 5 cm. Shown as part of the source telescope.

Japan Inc. Finally, a piece of cardboard, shown in Figure 5.8, was used to simulate the target. All energy delivered to this target was at normal incidence.

## 5.4   Device Fabrication

All material growths, fabrication and testing was completed at AFRL/RY. Although several wafer samples were grown for preliminary experiments, a material growth for the final BC-RCLED design was not accomplished. The device was instead modeled with Crosslight Finite Element Modeling software utilizing the data

Figure 5.8:    Cardboard target hung on a protective laser barrier. This target simulates the ground.

Table 5.4:    The fabricated devices tested, identified by their label. Also shown is the structure of the device tested.

| Wafer Label | Device Structure |
|-------------|------------------|
| G2-3039 | PIN Structure |
| G2-3069 | 4 stage BCLED |
| G2-3152 | 1 stage BCLED |
| G2-3181 | 3 stage BCLED |
| G2-3262 | Low resonance BC-RCLED |

collected from the preliminary investigations. The fabricated devices tested did not have the resonant cavity structure, however, the TJ was inserted as a spreading layer and for photon recycling in the multi-stage devices. These BC-LED wafers were used to fabricate devices for final characterization, and the wafers processed and their structural makeup, are shown in Table 5.4. More detailed epitaxial growth layers can be found in Appendix C. All devices were fabricated using material that was epitaxially grown with a Varian Gen II molecular beam epitaxy (MBE) system. The sample wafer material used included a p-i-n LED, 2, 3, and 4 stage BCLEDs. The PIN structure is a standard diode, and the remaining devices fabricated were BC-LEDs with Esaki TJs incorporated. The TJs were formed by growing a heavily doped $n^{++}$ layer on a heavily doped $p^{++}$ layer. The layers were degenerately doped so that the

conduction band in the n$^{++}$ material is approximately even with the valence band in the p$^{++}$ material. This allows electrons to tunnel through the narrow barrier that results from such extreme band bending due to the high doping. A three-step process was designed to produce the STREMERs and several wide area square mesas for further TJ investigations. The sizes of the square mesas were 80, 110, 140, 170, 200, and 250 $\mu$m, and were selected to bridge the gap from previous tests by Siskaninetz [53] on devices of 50 $\mu$m and myself on 300 $\mu$m devices. The STREMERs were designed with 150, 200 and 250 $\mu$m wide mesas, and lengths of 500, 1000, 2000, 4000, and 10000 $\mu$m. These stripe sizes were selected so that they can be combined to form the requisite aspect ratio during packaging. Table 5.5 shows the required length needed to produce the proper aspect ratio for a given device width.

Table 5.5:    The needed device lengths to create the proper aspect ratio of 0.006 given the device width.

| Width ($\mu$m) | Required Length (mm) |
|---|---|
| 150 | 25 |
| 200 | 33 |
| 250 | 42 |

From previous experimentation, current crowding has been observed when probing mesas on the top of the stack. Due to this effect, an extra processing step was added to the STREMER's process to insert an isolation layer. A conformal contact was used that started at the base of the device and traveled along its sides up to the top of the mesa, where it contacted the semiconductor surface. A SiN isolation layer was placed between the metal contact layer and the wafer surface, including the side-walls of the device. The isolation layer isolates the metal from the semiconductor surface in all areas except for the top of the stack over a 25 $\mu$m area around the top of the mesa. This forces current to flow only at that contact point. As shown in Figure 5.9, the metal overlaps the SiN and makes contact with the top of the mesa around the top perimeter, leaving an open aperture. The SiN is also deposited along
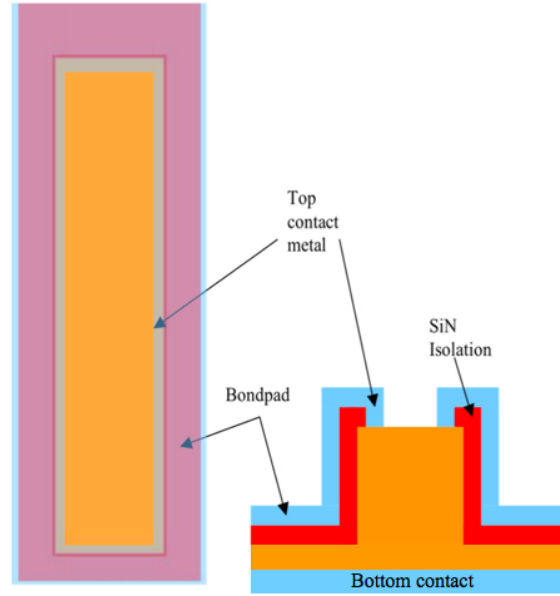
Figure 5.9: A depiction of the STREMER shown from the top and side view. An isolation layer is between the top metal contact and the wafer surface except for on the top of the mesa.

the mesa sides and at the base, extending outward from the mesas base, about 50 $\mu$m, to allow probing and bonding.

Figure 5.10 shows an intensity reading from the Sprircom 980M IR camera, displaying the beam profile from a 500 $\mu$m device. A 130 $\mu$m wide metal contact is used to probe the device. Evidence of current crowding can be observed under the metal contact, with a majority of the electrons injected into the device traveling directly beneath the metal, while some migrate outside the metal width before recombining. This causes the non-uniform emission pattern from the device shown. Its believed that an isolation layer will help prevent electrons from entering the device beneath the probe strip and, thus increase the uniformity of the beam by mitigating current crowding.

The device fabrication process is proprietary information of AFRL/RY, and is not given in detail, however, the devices were fabricated using standard cleaning and photolithography procedures, using inductively coupled plasma etching, electron-beam evaporation and various sputtering methods for metallization. The standard
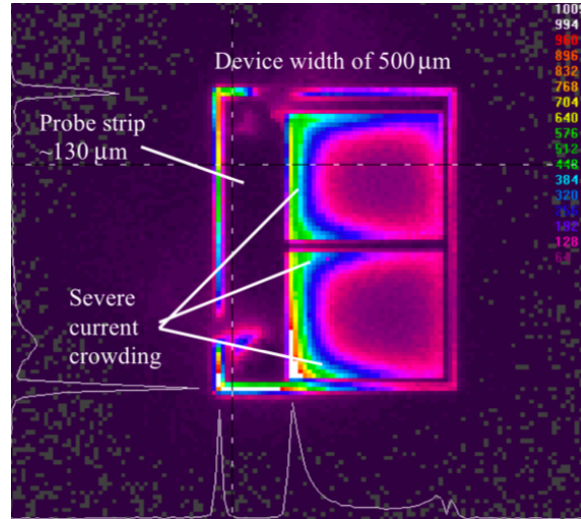
Figure 5.10: An intensity plot of a 500 $\mu$m, single stage device, with 130 $\mu$m wide metal contact. Evidence of current crowding can be seen under the metal contact. A large amount of radiative recombination occurs while very few electrons and holes recombine and produce light in other parts of the device.

p-metal recipe used at this facility is a Ni/Ge/Au/Ni/Au stack. Instead of this stack, an n-metal deposition was initially adopted, which consisted of Ti/Au, since the Ge sputter target was damaged during earlier processing. The p-metal produced a non-ideal ohmic contact, but current was still able to be injected into the devices for characterization. Metallizations performed by E-beam evaporation deposits a discontinuous metal layer at the top and the base of the mesa. This is due to the large mean free path of gas molecules at high vacuum, making the evaporation a highly directional deposition technique. Since a continuous, conformal layer is needed, approximately 6000 Å of Ti/Pt/Au was sputtered on the surface of the wafer. The backside of the wafer was evaporated with the same metal composition. A second series of devices were later fabricated with the proper n-metal composition.

Figure 5.11 shows a depiction of the final packaged device; with three of the 150 $\mu$m x 10000 $\mu$m devices used to create the desired aspect ratio. Multiple wire bonds are shown, and are used to enhance the uniformity across the devices. During the packaging of the final devices, a problem with the metal contacts on the surface and the back of the wafer adhering to the semiconductor was discovered. Although
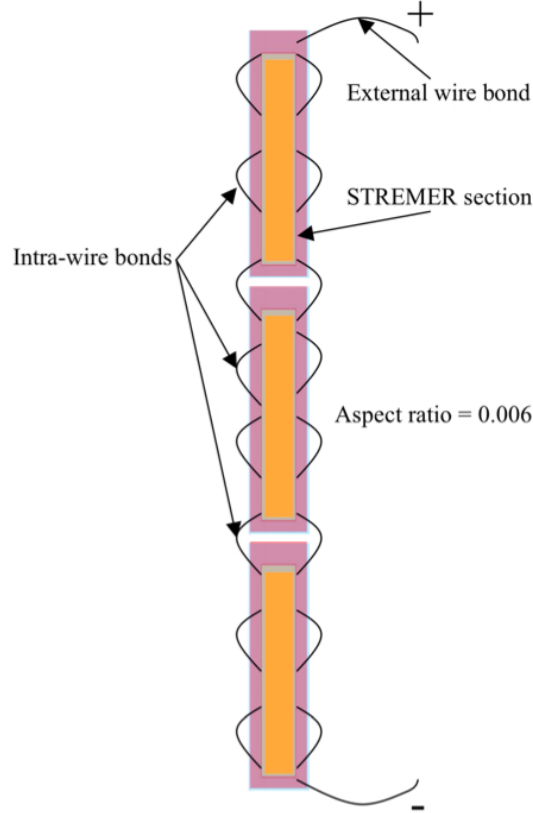
Figure 5.11:    Depiction of the STREMER showing wirebonding patterns and the leads for current injection.

some tests were done on the STREMER sections with drive current up to 500 mA, STREMER power tests could not be accomplished, nor could a current rating be determined, due to a metal adherence problem. Thus final determinations had to be inferred from the data collected for the devices tested.

## 5.5   Final Testing

The final testing reported in this section includes results from the beam uniformity versus current density investigation, total power tests, and the remote sensing demonstration. Data was measured and modeled with Crosslight$^\circledR$ to determine final values in each case.

*5.5.1   Beam Uniformity vs Current Density .*    Single stage BC-LEDs were used to investigate the current spreading capability of the TJ in devices with mesa widths ranging from 110 to 250 $\mu$m. An IR camera was used to capture a pixilated image of the beam exiting the device. An average relative variance was calculated for each device tested, with all values having arbitrary units. The total current handling capability was determined by gradually increasing the drive current from 10 mA up to device failure or when roll-over occurred. Since this experiment was done to assess the beam uniformity only, total power out is not a concern, and no power measuring instrumentation was utilized; the pixel intensity registered by the camera was used to determine roll-over. A series of gray scale pictures of the optical emission from the devices were produced using the Spiricon camera, where each pixel in the image captured by the camera, has a gray scale value that corresponds to the relative optical intensity emitted from the device. A bright gray colored pixel corresponds to a relatively large optical intensity being delivered to that pixel, while a darker gray pixel corresponds to a relatively small optical intensity being delivered. Several pictures depicting beam profiles from several devices, at various current injection levels, were produced and used for statistical analysis to determine the relative beam profile variance for each device . An in-house developed code was used to analyze the gray scale pictures captured by the Spiricon 980M. The camera measures pixel intensity and the in-house code records the grayscale value of each pixel. Each pixel value is then used to calculate a mean-pixel and variance value across the device surface. These mean and variance values are assigned to each picture, making it possible to quantify the uniformity of the beam across that surface. An average relative variance is calculated for each set of devices, according to size, with all values having arbitrary units. Typically, the application determines what is an acceptable variance in beam uniformity. Although for this specific application, 3-D remote sensing, a strict adherence to uniformity values is not required. A 20-25 % variability was determined to be acceptable, primarily from discussions with other researchers at AFRL [34].

Table 5.6: Current density for all device sizes at the point where the relative variance surpasses the accepted range, 0.20-0.25. The 110 $\mu$m devices failed before larger current densities could be achieved. Only devices 110 $\mu$m and 140 $\mu$m have current densities that are near the benchmark value.

| Device Size ($\mu$m) | Variance | Current Density ($mA/cm^2$) |
|---|---|---|
| 110 | 0.15 | 1,983,471 |
| 140 | 0.23 | 991,736 |
| 170 | 0.25 | 415,225 |
| 200 | 0.31 | 175,000 |
| 250 | 0.26 | 48,000 |

For each device size group, the current density values where the variance approaches the accepted cuttoff value range, 0.20-0.25, is shown in Table 5.6, and a detailed presentation of each device's variability is presented in Appendix E. Table 5.6 shows how the variance changes with device size and current density. To determine what a typical current density might be, consider the OSRAM LEDs. A device having a current rating of 1 A, a surface area of 1 x $10^{-4}$ $cm^2$, creates a current density of approximately 1 x $10^7$ $mA/cm^2$. Using this as a benchmark, the current densities were calculated for the in-house developed devices. Table 5.6 also lists the device sizes and the current densities, for comparison with a benchmark value calculated using the OSRAM LEDs. From Table 5.6, it can be concluded that the 110 and 140 $\mu$m devices have current densities near the benchmark, and maintain a variance lower than $\sim$ 0.25. It can also be seen that a larger current density is possible in the 100 $\mu$m device, while maintaining a good relative variance, $\sim$ 0.20-25. This analysis assumes that 1 x $10^6$ mA/cm$^2$ is a typical drive current density for devices of this size, per the OSRAM current rating. The uniformity of the OSRAM device is not known and cannot be compared or commented on. Figure 5.12 shows a gray-scale image of a 140 $\mu$m device taken by the Spiricon IR camera. There are noticeable darker regions near the center of the device, which indicates that a smaller intensity is emitted from the center than that occurring at the edges. This particular device has a relative variance of $\sim$ 0.21 at a current density of $\sim$ 9.2 x $10^5$ mA/cm$^2$.
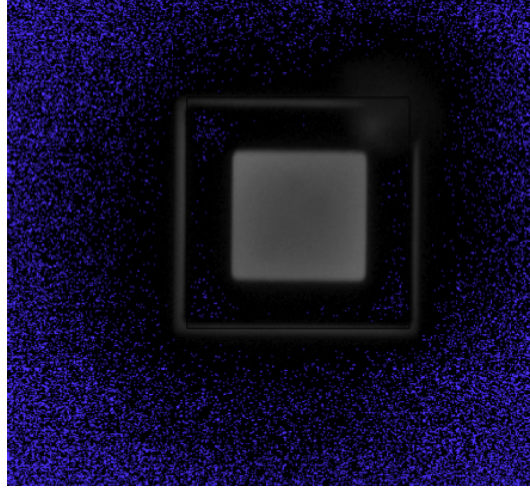
Figure 5.12: A gray-scale IR image of a one-stage 140 $\mu$m device under forward bias. Pixel intensities are shown, with a noticeable variation between the edges and the center of the device. The lighter grey edges indicate a higher optical intensity.

*5.5.2 Total Power Measurements.* Total power measurements are part of the characterization experiments done on all devices. Modeling was a key part in the determination of the total power of the in-house developed devices. For the total power measurements, an integrating sphere was used, along with a digital multimeter and a 40 A current source, to record the maximum total output power from all devices tested. The devices were mounted using a custom designed holder, and abutted to the opening of the sphere. The integrating sphere collects the energy and converts it into current, which is measured by the DMM. This current is then multiplied by a conversion factor, and a final value for the total optical power is obtained. The conversion factor at this wavelength, was determined by a previous calibration by AFRL/RY laboratory personnel, and at 940 nm has a value of 1.454 x $10^{-4}$ A/W.

*COTS Devices*

The COTS LEDs were purchased from OSRAM GmbH and are part of the IR Dragon high-powered LED line. All five of the devices tested were the Dragon IRED SFH 4231-7 (940 nm). The SFH 4231-7 data sheet can be found in Appendix D and a picture of one of the OSRAM devices mounted for testing, is shown in Figure 5.13. Of particular importance was the exit cone of these LEDs, since the OSRAM devices have
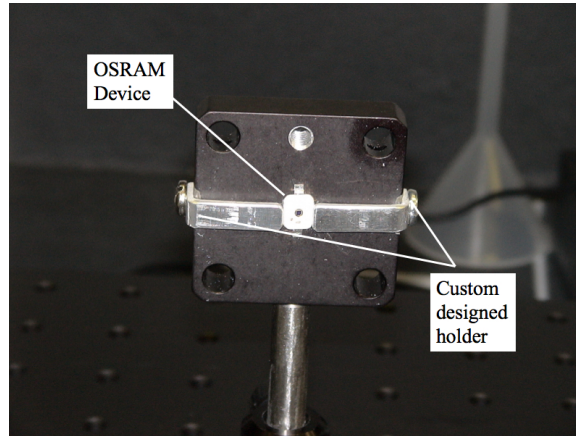
Figure 5.13: The OSRAM SFH 4321-7 device mounted in custom holder for remote sensing demonstration.

an exit angle cone of $120^o$, a sufficiently large lens was required to capture emitted energy, otherwise, a lot of energy will not be coupled into the telescope and available for usage. Since the key for a successful field test is to deliver the requisite energy on target, the loss of any energy was of great concern.

The COTS devices were also tested to verify the rated power was achievable using the field test setup with the integrating sphere abutted to the holder. The COTS devices were advertised to deliver 500 mW at 1 A drive current. Table 5.7 shows the measured power and the average power of all tested devices, which is 541 mW. To capture the energy, a Fresnel lens with D = 25 cm, F = 5 cm was used, which was necessary to produce the appropriately sized spot at the target. This was the largest commercially available lens that could be purchased off the shelf. Previous calculations verified that a lens of this size should be able to capture all of the energy emitted from a device with an emission cone of $120^o$ or less. With the source 5.4 cm away from the Fresnel lens and the integrating sphere placed 51.75 cm away from the Fresnel lens, the total power was recorded at $\sim$ 20 mW with 100 mA drive current, 10 % of the total rated current. A total power of 20 mW represents about 40 % of the total available power at that drive current, suggesting that the Fresnel lens does not capture all of the energy. Some energy is lost due to the lens inability to transmit 100 % of the energy captured. Also, some energy is lost due to the abberations created

Table 5.7:    The measured power for a sampling of OSRAM devices.

| Device | Drive Current (A) | Power (mW) |
|--------|-------------------|------------|
| 1 | 1.04 | 526 |
| 2 | 1.04 | 542 |
| 3 | 1.04 | 537 |
| 4 | 1.04 | 549 |
| 5 | 1.04 | 550 |
| | Average | 541 |

by the Fresnel lens, and energy trapped in the lens that may travel laterally within the lens.

### STREMER

Because the STREMER is an experimental device, additional testing was conducted prior to the power measurements. The STREMERs are devices made from smaller sections, with final devices that are relatively large, having a longest dimension of about 2.5 cm. Each individual section was probed to verify proper functionality. The ILX current source, with a maximum drive current of 500 mA, was used to drive the devices. This setup used a microscope directly above the devices to allow near field imaging. The maximum current from the ILX was sufficient to adequately drive only the 1000 and 2000 $\mu$m long STREMER devices to high level injection. This was determined by viewing the intensity image from the IR camera. Devices larger than 2000 $\mu$m, only showed intensities that were qualitatively about one-half of the intensity level captured by the smaller devices, indicating that the 500 mA current source was not sufficient to push the STREMER into a high level injection condition. Figure 5.14 shows a 150 x 1000 $\mu$m device under a 500 mA drive current with a neutral density filter, ND = 1, in place over the camera's detector to prevent detector saturation.

Again, there was difficulty achieving good adherence between the gold metal contact layer, the silicon nitride isolation layer, and the semiconductor surface using the available sputtering and evaporation systems used in device fabrication. Multiple attempts were made to adjust the deposition process for better adhesion, without

140 x 1000 μm
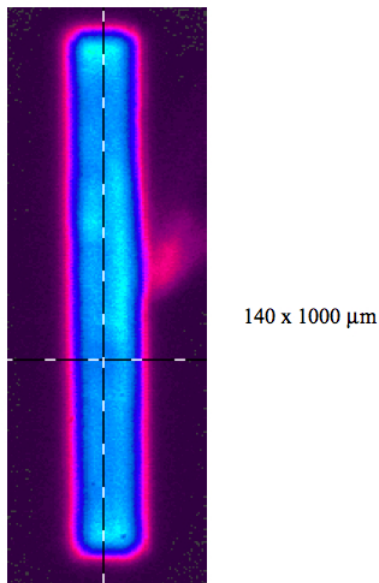
Figure 5.14:    A 150 x 1000 $\mu$m STREMER under a 500 mA drive current. A neutral density filter, ND = 1.0, is placed in front of the camera collecting the energy emitted from this device to prevent detector saturation.

success. For this reason, remote sensing demonstrations using the STREMERS could not be accomplished, but valuable data was obtained from using the OSRAM LEDs in the remote sensing demonstration.

*5.5.3   Remote Sensing Demonstration.*    The Remote Sensing Demonstration was performed to verify that a system could be designed that would deliver sufficient energy on target using COTS devices. The Remote Sensing Demonstration setup required a combination of refractive and Fresnel lenses to capture the maximum amount of emitted energy and shape the beam to the desired spot size to delivered it a distance of 5000 cm. The full-scale experiment was not accomplished in real-world condition, rather, a scaled version was completed instead in the Optoelectronics Laboratory at AFRL/RY, with fluorescent lighting simulating the solar background. An Optronic Laboratories OL 770 Multi-Channel Spectroradiometer was used to measure the radiation spectrum of the laboratory lighting, and the measured intensity spectrum is shown in Figure 5.15. This measurement was taken with the spectroradiometer placed in the same plane as the detector, and pointed toward the target. A 5.08 cm lens,
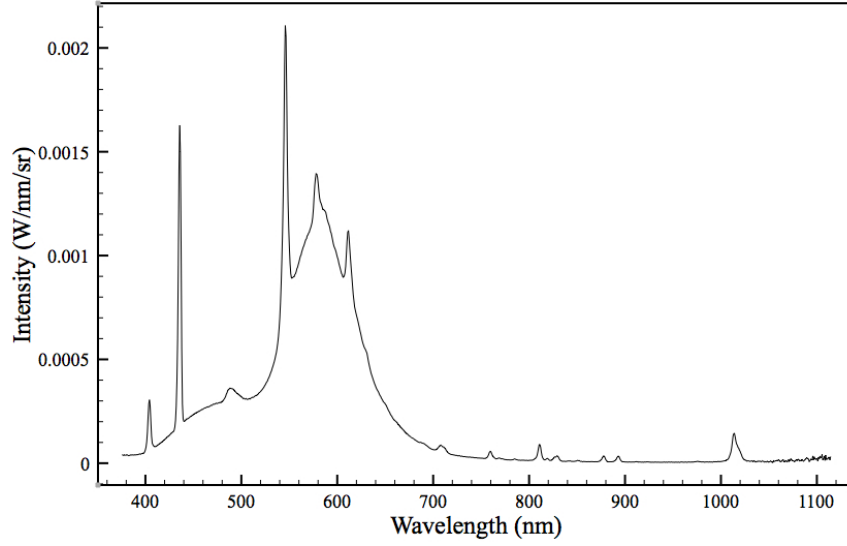
Figure 5.15:    The radiation spectrum of the laboratory lights used as a *solar-like* background noise generator.  The spectrum was measured by a spectroradiometer from Optronic laboratories.

with a 7.5 cm focal length, was used to collect the energy from the target, and an 800 nm long-pass filter was in place, in front of the aperture. Lastly, a tarp was placed over the spectroradiometer setup. All of these steps were done to create the similar ambient lighting condition experienced by the detector within the camera.

For the scaled demonstration, the background noise was generated by the fluorescent lighting in the lab, and an analysis was performed over the band of interest, 0.8 - 1.1 $\mu$m, which has smaller values than the actual solar radiation over the same spectrum. Figure 5.16 shows a view of the irradiance spectrum from the fluorescent lights, found by dividing the intensity spectrum of Figure 5.15 by the range squared. Figure 5.17 shows a plot of the curve used to model that spectrum, over the band of interest. The curve used to model that spectrum is given by
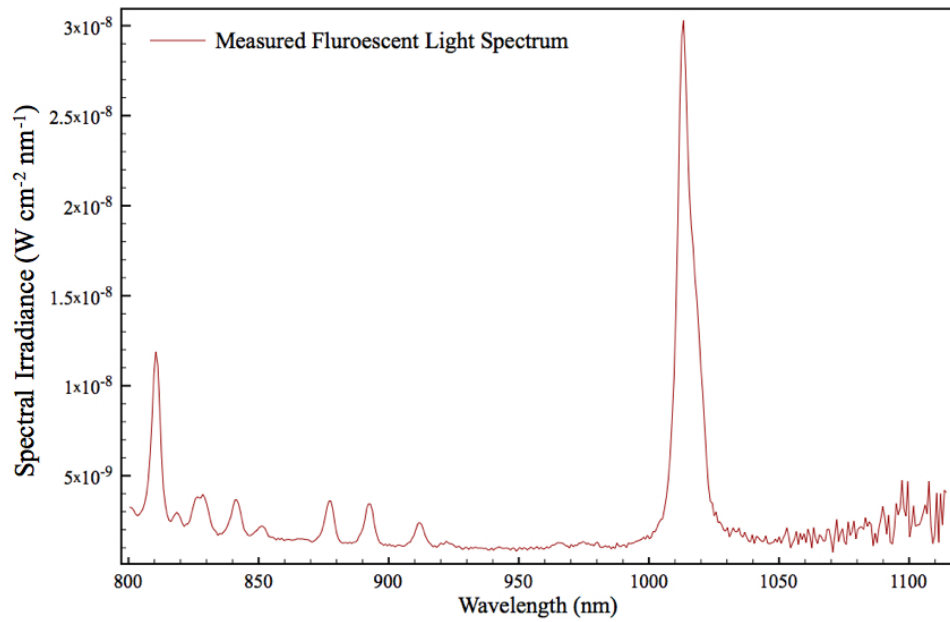
Figure 5.16:    The radiation spectrum of the laboratory lights from 0.8 - 1.1 $\mu$m used as a *solar-like* background noise generator, and the curve used to model it, given by Equation 5.3.
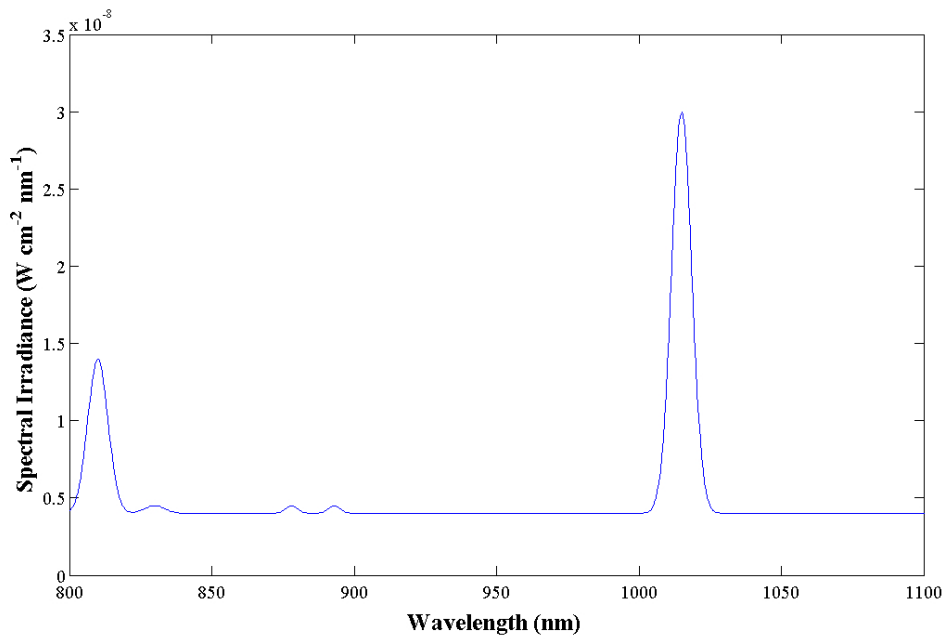


Figure 5.17:    Curve used to model the radiation spectrum of the laboratory lights from 0.8 - 1.1 $\mu$m. The curve is given by Equation 5.3.

$$E_{spec-lights} = 4.9 \text{ x } 10^{-9} + 1.8 \text{x} 10^{-8} \exp\left[-\left(\frac{\lambda - 810}{5}\right)^2\right] +$$

$$0.5 \text{ x } 10^{-9} \exp\left[-\left(\frac{\lambda - 830}{5}\right)^2\right] +$$

$$0.5 \text{ x } 10^{-9} \exp\left[-\left(\frac{\lambda - 878}{5}\right)^2\right] +$$

$$0.5 \text{ x } 10^{-9} \exp\left[-\left(\frac{\lambda - 893}{5}\right)^2\right] +$$

$$2.6 \text{ x } 10^{-8} \exp\left[-\left(\frac{\lambda - 1015}{5}\right)^2\right] \qquad (5.3)$$

where $E_{spec-lights}$ is the spectral irradiance in W cm$^{-2}$ $\mu$m$^{-1}$ and $\lambda$ is the wavelength in $\mu$m. The noise due to the fluorescent lab lights, $\Phi_{lights}$, can be found by integrating Equation 5.3 over the band of interest, which gives $\Phi_{lights} = 106$ pW. The shot noise current produced by the fluorescent lights in the lab, $i_{shotlights}$, was calculated using Equation 2.8 - Equation 2.10, and was found to be $i_{shotlights} = 3.2 \text{ x } 10^{-17}$ A. Lastly the shot noise current produced by the solar spectral irradiance, $i_{shot}$, which was found to be $i_{shot} = 5.5 \text{ x } 10^{-17}$ A.

As shown in Equation 2.10, the noise current is calculated by integrating over the band of interest, which for these purposes is 800 - 1100 nm. By reducing this band-width, from 300 nm, to a much narrower band, centered around the source emission wavelength, the noise current can be reduced. Notch filters can be found, allowing a much smaller band-width to be transmitted, but are more expensive than typical long-pass filters, like those used in this investigation. By reducing this noise current, a larger SNR will be acheived.

A one-tenth scaled version of the full size experiment was conducted using a cardboard target placed 500 cm down-range to simulate the target. For this demonstration, the beam was not reshaped into a stripe, as the focus is on the amount of power delivered to the target. Once the total power delivered to the target is known,

the irradiance value can be determined using the area of the stripe at the target. A shroud was placed around the camera to simulate the light-blocking effect of a protective housing for the sensor system. Protective enclosures are often used with LIDAR systems. Measurements were all taken at normal incidence, and represent the baseline condition.

### OSRAM Devices

For this demonstration, the integration time($\tau_{int}$) for the Spiricon camera was assumed to be 330 msec, and the detector QE ($\eta_{det}$) was assumed to be 0.6. Also, the reflection coefficient of the cardboard target used was 0.718 [62]. Although this value is the reflectivity for white paper, it is acceptable for this application. The source telescope was able to couple and transmit about 20 mW (40%) of the scaled total energy emitted from the OSRAM 4321 to the target at 500 cm, producing a signal current value of $i_{sig} = 3.6 \times 10^{-12}$ A. The noise current produced by the fluorescent light energy listed above, was $i_{shotlights} = 3.2 \times 10^{-17}$ A.

In a full-scale experiment, the target range is increased to 5000 cm, and the supply current to the COTS device is increased to 1 A. A target reflection coefficient of 0.06 is used, which represents asphalt. The expected energy coupled into the source telescope remains at 40 %, suggesting that $\sim$ 216 mW will be delivered to the target. Using the same detector parameters mentioned above, the noise current produced by the solar energy, $i_{shot}$, was found to be 5.5 x $10^{-17}$ A. These conditions produce a signal current $i_{sig-full} = 3.95 \times 10^{-15}$ A. The resulting SNR will be $\sim$ 20 dB, which is sufficient to meet the established criteria. Figure 5.18 shows a plot of the SNR vs LED power under conditions similar to those used in the remote sensing demonstration. The plotted data suggests that $\sim$200 mW source is sufficient to produce a SNR of 20 dB at a range of 50 m, using a collection optic with a diameter of 2.54 cm, which is in good agreement with the 216 mW value obtained from the scaled experiment. The source telescope is not as efficient as expected, only transmitting about 40 % of the available energy, where some systems are over 90 % efficient [26]. An optical
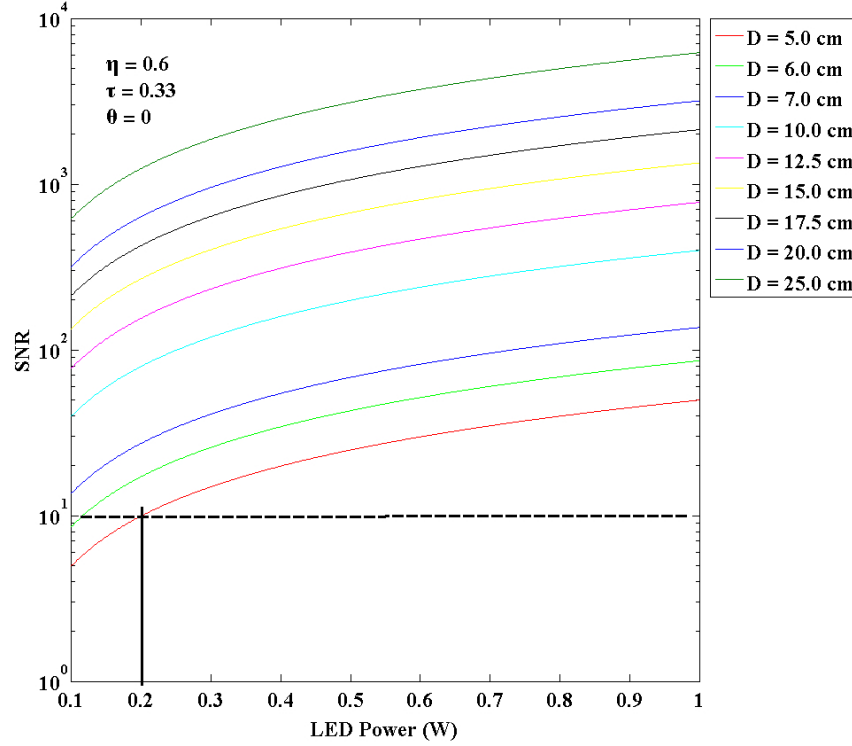
Figure 5.18:    SNR vs LED power for a system with illuminator at normal incidence to the target.

system with a larger efficiency would result in a much larger SNR. No efficiency was determined for the detector telescope. For this stage of development, optical system efficiency is a secondary concern.

A Spiricon 980M CCD was focused onto the cardboard target via the source telescope with a scaled IFOV. Since both the camera and camera telescope would more than likely be enclosed in an actual system, a black tarp was placed over them to simulate this enclosure. The tarp blocked a large percentage of the ambient light, in addition to a high pass filter ($\lambda = 800$ nm), that was placed in front of the camera to filter extraneous light energy. Also placed over the detector were ND filters, with values ranging from 0.3 to 2.0, to prevent detector saturation.

Full-color pictures of the target, under light condition, were taken. Light condition is when all lab lights are turned on, to include the optics table light located directly above the source and the camera. The pictures are from the one-tenth scale
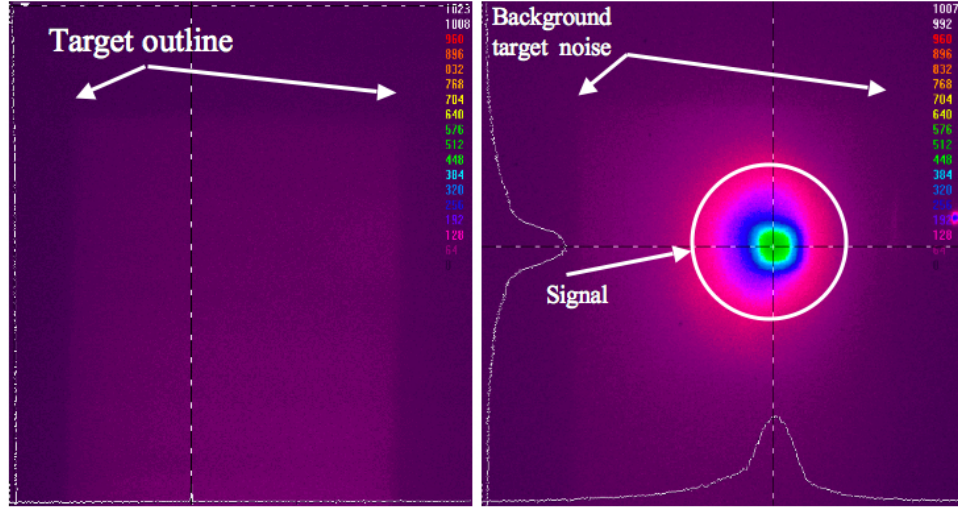
Figure 5.19:    These images show the background return under light condition with and without the LED energy incident on the target . The outline of the cardboard target can be seen in both cases, The image size, at the target, is $y_i = 9.59$ cm at the target plane. These pictures are a qualitative measure of the energy delivered to the target.

experiment conducted in the laboratory. They show the target without and with the LED source energy incident, and are presented in Figure 5.19. The full-color images show a qualitative representation of the energy distribution at the target. The SNR shown in these pictures was calculated to be $\sim$50 dB. The same process used to determine the SNR for the scaled experiment was adopted for the full-scale experiment. Because the scaled experiment confirms the calculated results, results for the full-scaled experiment are presented with high confidence.

As stated previously, vehicle platforms may view the target area at normal incidence or at an angle. The worst case condition for these applications exist when the sensor is mounted on the AGV, resulting in an incidence angle of $\theta = 1.54$  rad. Figure 5.20 shows how the diameter of the collection optic impacts the device power needed to maintain the SNR desired at the aforementioned angle. An optic with a minimum diameter of 12.5 cm is needed to ensure that the device power needed is less than 0.5 W. NTK Co., Ltd. offers several Fresnel lenses that range in size from
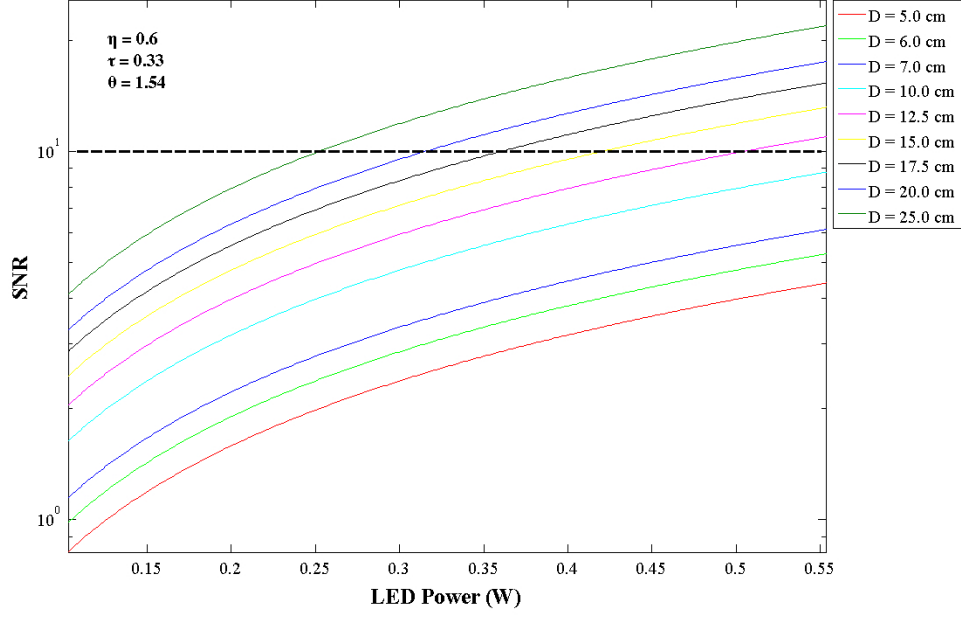
Figure 5.20: SNR vs LED power for system mounted on an AGV, with incidence angle $\theta = 1.54$ rad.

10 to 140 cm. Since the optimized STREMER will deliver $\sim 330$ mW of power, a lens with minimum a diameter of at least 20 cm is needed.

## 5.6   Summary

This chapter presented the calculations done to design the telescopes for the camera and the source. The final design used traditional refractive lenses, as well as Fresnel lenses, to deliver the maximum amount of power to the target as possible, and to capture as much of the return signal as possible. A brief description of the test instruments used, with photos, was also included. Finally, the results from the uniformity testing and the final remote sensing demonstration were offered and summarized. Results of the uniformity experiments suggested that the maximum current spreading distance of this as-designed TJ is 140 $\mu$m.

The one-tenth scale laboratory experiment was conducted to validate the theoretical determination, that a source with output power of $\sim 216$ mW would be needed to achieve a SNR of 20 dB. COTS devices were used for the experiment, and demon-

strated the capability of wide area LEDs to function as an illuminator for imaging applications. The data collected from the devices tested in the laboratory, using fluorescent lighting as a noise generator, was extrapolated to determine the results of a full-scale demonstration, with the energy at normal incidence to the target, and at an angle expected when the sensor is placed on an AGV. The latter represents the worst case operational condition, under which a lens 20 cm in diameter is necessary to achieve the 20 dB SNR, when $\tau_{int} = 330$ ms and the $\eta_{det} = 0.6$.

# VI. Conclusion

## *6.1  Research Accomplished*

The research goals established at the onset of this endeavor were developed from requirements motivated by the need for high-speed, 3-D image acquisition. The current state-of-the-art for 3-D image acquisition utilizes traditional point and line scanners, and use sophisticated ways of producing stripe-like image patterns on the target areas, and sweeping these patterns over the FOV of the scene. Several problems with using these methods have been identified, to include image inaccuracies, and long time lags in the frequency of arrival of the data received. This dissertation has presented an illumination source capable of delivering a solid striped image pattern to the target, that, when integrated into the HRIS, will enable real-time 3-D image acquisition, and address the inherent problems outlined in this dissertation.

The work completed over the course of this study has demonstrated the use of an Esaki TJ as an effective current spreading layer in large area LEDs. The TJ has been studied and used in other applications, but none have quantified the upper limit of it's ability to perform current spreading in large-area LEDs. By setting a minimum variability in uniformity across a device, in this case 0.25, and a minimum current density, in this case $1 \times 10^6$ A/cm$^2$, we have determined that a mesa width of 140 $\mu$m is the maximum size at which our TJ could maintain effectiveness as a current spreading layer. The TJ is a key enabling technology in the development of the wide-area STREMER, because it permits the fabrication of a device capable of producing a energy pattern with an aspect ratio of 0.006, and a relatively uniform emission from the device.

This work has also produced a design for a large area BC-RCLED (STREMER) for integration into the HRIS prototype, eliminating the need for multi-gimbaled point or line scanners, or the need to utilize a bank of point scanners. By synthesizing the Esaki TJ, DBR mirrors to form a RC, MAR, and MQW into an LED, we have developed a device with a very large surface area, expected to have relatively good beam uniformity, deliver energy in a relatively narrow emission cone ($30^o$ or less),

and deliver an output power of over 330 mW. Using this device as the illuminator for the HRIS, the data acquisition time is greatly reduced, because the entire FOV can be acquired with only one sweep of the area, which cannot be done with current scanners.

Additionally, we have determined the range of key parameters needed to design the HRIS, to include the angle of incidence, the quantum efficiency of the detector, the integration time, the size of the collection optic, and we modeled the impact of adjusting each parameter. As stated earlier, our device will have an output power of over 330 mW, which is sufficient for the purpose of meeting the 20 dB SNR requirement established for a robust system, delivering energy to a target 5000 cm away. By adjusting any one of the parameters mentioned, the SNR can be increased, or the range extended, while keeping the source power constant.

Lastly, we have demonstrated that the STREMER is an effective, active illuminator for the HRIS, by performing a scaled remote sensing demonstration. The demonstrations used COTS devices, and verified the theoretical methodology, which determined that $\sim$216 mW of power would be needed to achieve the 20 dB SNR at an angle of incidence, $\theta = 90^o$, the condition utilized in the scaled demonstration. Although the demonstrations did not represent the exact solar condition, the data obtained from the experiment was extrapolated to represent ambient solar conditions and direct comparisons could be made.

By reaching these four milestones, we have meet all of the research goals established at the onset of this work, and advanced the field of 3-D image acquisition by producing a design for a key component for the HRIS. The next section discusses, in more detail, the process to optimize the device design, and, the remote sensing demonstration.

## 6.2  Summary of Results

Although the TJ has many benefits, it does come with some limitations. Since it is a scattering center, it needs to be properly placed relative to the AR, to limit its negative affect on device efficiency. Experiments to minimize this impact were conducted when the TJ was placed in multiple positions relative to the AR (the TAS distance) and the total output power was measured. It was clear that as the TJ was moved away from the AR, the total output power increased, suggesting that the maximum TAS possible is most desirable. Device designers utilizing TJs must still be mindful that if they are placed inside a resonant cavity, the TJ must be located in resonant intensity nodes for best device efficiency. This could cause the cavity to become very large, depending on the number of stages being used, creating other issues that can arise when using large vertical cavities, like reduced energy transfer efficiency between optical emission and the resonant intensity wave inside the cavity, reducing the device efficiency.

Testing showed that the TAS also impacted the beam uniformity across the surface of the device. During this testing, the TAS was varied and the uniformity of the beam was recorded, while holding the device size constant. It was concluded that as the TAS was increased, the uniformity improved. With the TAS = 1742.5 Å, uniformity across the surface of the device was $\sim 80\%$, and with the TAS = 250.0 Å, beam uniformity decreases to less than 50%. Since beam uniformity is directly tied to current crowding, it was suggested that the TJ would be a good current spreading layer for wide area LEDs. Although this was not the primary purpose for using a TJ in these devices, spreading was a beneficial by-product. A correlation between the current density and the variation in uniformity across the device was found, as shown in Table 6.1. For current densities smaller than those shown in the table, which correspond to a larger device area. Larger relative variance values were seen, which suggests that a larger beam nonuniformity will be the result. From this current density-relative uniformity variance relationship, it could be concluded that the 140 $\mu$m device is the largest device in-which the TJ can function as a good current

Table 6.1: Current density for all device sizes at the point where the relative variance surpasses 0.20. The 110 $\mu$m devices failed before larger current densities could be achieved. Only devices 110 $\mu$m and 140 $\mu$m have current densities that are near the benchmark value.

| Device Size ($\mu$m) | Variance | Current Density ($mA/cm^2$) |
|---|---|---|
| 110 | 0.15 | 1,983,471 |
| 140 | 0.23 | 991,736 |
| 170 | 0.25 | 415,225 |
| 200 | 0.31 | 175,000 |
| 250 | 0.26 | 48,000 |

spreading layer, in this case, one producing a relative variance of 20 - 25 % or better.

Plots of various design parameters were produced to guide development of the final HRIS. Parameters include, detector quantum efficiency ($\eta_{det}$), detector integration time ($\tau_{int}$), system range (R), and source power rating (P$_{source}$). For a given SNR and R, one can determine P$_{source}$ based on $\eta_{det}$ and $\tau_{int}$. Additionally, R can be extended, using the same source, by adjusting $\eta_{det}$ and $\tau_{int}$. For this particular case, given an SNR of 20 dB, and a R of 5000 cm, and assuming $\eta_{det} = 0.6$ and $\tau_{int} = 0.033$ sec, an LED source needs to have a power rating $\geq 321$ mW.

A key part of this effort was to design the BC-RCLED STREMER, with a unique emission surface area in a rectangular format, having a width-to-length aspect ratio of 0.006 , that can be used as an illuminator for the hybrid range-intensity sensor. From the data collected from this investigation, an optimized STREMER design could be determined. Figure 6.1 shows the STREMER cavity design. The STREMER has a $10\lambda/2$ cavity, three TJ-AR-TAS stages within the cavity, with the TJs in resonant intensity nodes, and the ARs in resonant intensity antinodes. To ensure that the TJ and the AR is properly placed, the TAS layer must be $\frac{3}{4}\lambda - \frac{1}{2}(AR + TJ)$, where $\lambda$ is the operating wavelength adjusted for the heat induced red-shift. The bottom highly reflective DBR consists of twenty pair of alternating layers of $Al_{0.5}Ga_{0.5}As$ and $Al_{0.9}Ga_{0.1}As$, creating a mirror with reflectivity of nearly 100%. The top DBR is the output coupler of the device, and consists of four pair of alternating layers of
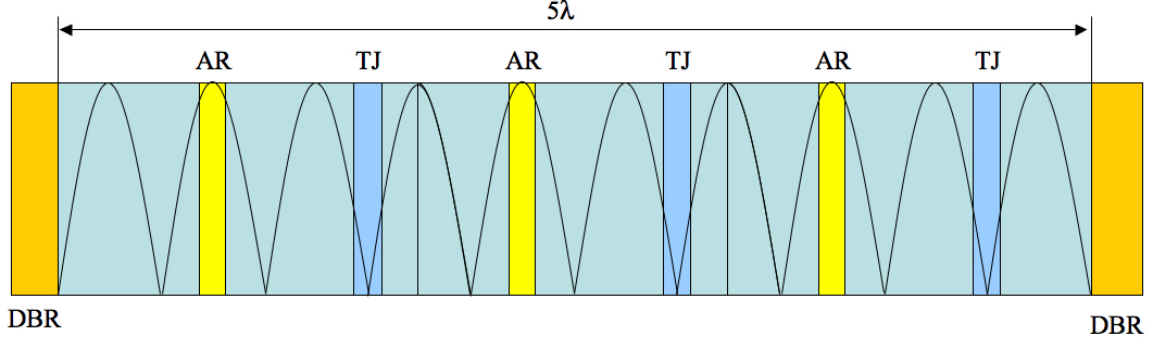
Figure 6.1:    STREMER cavity design. This is a three-stage device with TJs placed in resonant intensity nodes and the ARs in antinodes. The bottom DBR, on the left, is a 20-pair stack and the top DBR, on the right, is a 4-pair stack. The cavity is $10\lambda/2$ long.

the same structural constituency as the bottom DBR structure, with a reflectivity of around 75 %. To construct an efficient mirror to sustain resonance at the red-shifted wavelength, the layers of the DBRs need to be $0.0714\lambda_0$ for the $Al_{0.5}Ga_{0.5}As$ layer, and $0.0781\lambda_0$ for the $Al_{0.9}Ga_{0.1}As$ layer. The physical dimensions of the STREMER designed for the hybrid sensor is 140 $\mu$m x 3000 $\mu$m. These values create the necessary aspect ratio, 0.006, to deliver a stripe down range with dimensions 18 cm x 3000 cm. The STEMER is a set of three rectangular devices, as shown in Figure 6.2. A 200 $\mu$m STREMER was modeled and produced a total output of $\sim$ 9 mW. Total power measured was compared to the total power modeled, and revealed a discrepancy of $\sim$ 17 % between the modeled and actual values, suggesting the total power of a 200 $\mu$m STREMER BC-RCLED is $\sim$ 7.8 mW at 500 mA. Power scaling analysis reveals that it is possible to produce a STREMER device with total output power over 300 mW. The device's emission cone could not be modeled with the current version of Crosslight®, so no conclusive modeled data can be presented showing how the resonant cavity reduces the emission cone.

A successful remote sensing demonstration using a commercially available emitter, the OSRAM LEDs, and an off-the-shelf IR camera was accomplished. A target was placed at a range of 500 cm, and was partially illuminated by an OSRAM LED, and the return signal imaged by the IR camera. Because testing was conducted in
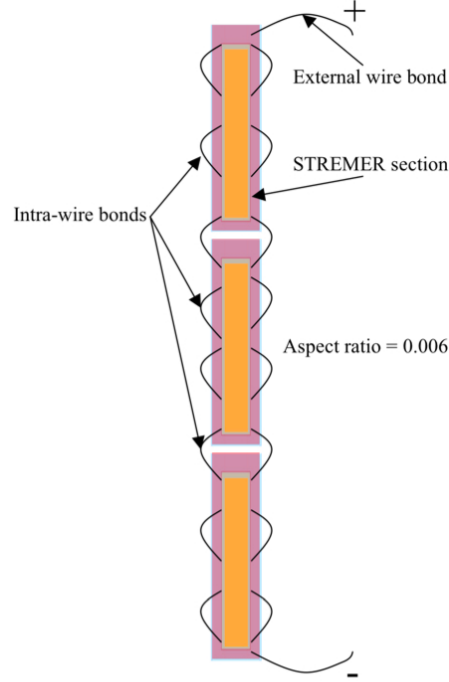
Figure 6.2: The schematic of the STREMER. The STREMER is made of three smaller devices, connected vertically, to create the required aspect ratio. It is wire bonded around its perimeter to improve beam uniformity.

the laboratory, fluorescent lighting was used to generate background noise, and these results were extrapolated to determine actual values. The noise current produced by the solar energy, $i_{shot}$, was found to be 5.5 x $10^{-17}$ A, and the noise current produced by the fluorescent lights was $i_{shotlights}$ = 3.2 x $10^{-17}$ A. The signal current produced during the one-tenth scale experiment was $i_{sig}$ = 3.6 x $10^{-12}$ A, and the extrapolated signal $i_{sig-full}$ = 4.0 x $10^{-15}$ A. The final full-scale SNR produced was ~20 dB at normal incidence.

With the sensor system mounted on an AGV, a likely incidence angle of 1.54 rad would be created. Under this, worst case condition, the STREMER delivers sufficient energy to the target, meeting the 20 dB SNR requirement, provided a collection optic of 15 cm or larger is used, with a detector having an integration time of 330 msec and quantum efficiency of 60 % or better.

Development of an in-house emitter with the proper aspect ratio of 0.006 was accomplished, but wafer growth could not be completed. Although fabrication and

testing on STREMER devices of the BCLED variety was accomplished, packaging for total power determination, current handling capability, as well as the remote sensing demonstration, could not be accomplished because of inadequate adhesion between the metal contact layer and the SiN isolation layer. This limitation needs to be overcome to complete the device characterization. Deposition of conformal metal on conformal SiN has neither been a primary focus of this effort, nor the focus of the researchers at this facility, so a suitable process did not exist. An alternative isolation layer could be silicon dioxide. Processing could have caused the problem, so a process to ensure greater adherence of conformal metal to conformal SiN needs to be developed.

### 6.3   Future Work

Although the STREMER was fabricated and tested, there were issues that limited its full utilization in this investigation. An isolation layer was used to separate the metal contact from the wafer and the side-walls of the STREMER device. Only a portion of the metal was in contact with the top of the mesa, preventing the opportunity of extensive current crowding under large area contacts. It is difficult to determine the full impact of using this layer, because adhesion became an issue. This could have come from contamination in the sputter chamber, or from processing steps. Several AFRL researchers [22] have indicated that adhesion of metal to SiN, whether sputtered or evaporated, is an issue. Developing a suitable process to address this problem is needed to fully exploit the STREMER. Alternately, a different isolation layer could be studied and utilized in the STREMER process. Once this is accomplished, a full-scale remote sensing demonstration can be completed using the STREMER.

Additionally, since the final STREMER design, a BC-RCLED, was not fabricated, the next logical step would be to grow wafers with the structure designed in Chapter 5, fabricate, and package the actual device. Once packaged, L-I and I-V curves can be produced and the total power from the device can be established, as

well as the maximum drive current. After this characterization, the full-sized remote sensing demonstration under ambient solar conditions could be accomplished. Once demonstrated using a single IR camera, a second IR camera can be integrated into the test set-up, and the data collected, and read into the image-processing algorithm. At this point, real-time data cannot be processed because the illuminator is not being modulated, or swept across a target area. Once it has been demonstrated that the cameras and the algorithm is operating within expected norms, a mask-set producing a device that can be modulated around a DC bias will be necessary, but, a very good isolation layer must be identified.

As stated earlier, placing the TJ as far away from the AR as possible is ideal, but large cavities are not as efficient as shorter ones. At some point, the cavity length will negate the benefit of using the TJ, and multiple stages. An investigation to determine the optimal cavity length could further optimize the proper placement of the TJ, the proper number of stages to use in the AR, and the best cavity length to accommodate all structures, to make the most efficient device possible.

*Appendix A.  Light Emitting Diode Research and Development*

## A.1  Early LED Research

Luminescence and incandescence are the two primary phenomena that characterize the release of electromagnetic energy (light) from matter. The latter is induced by raising the material to a requisite energy level. The high temperature in the material is the catalyst for electron excitation, which eventuates in electron relaxation, and hence, photon generation. An example of incandescence is the glow of a piece of iron when it is heated to within its melting point. Another example is the tungsten filament in light bulbs. Luminescence, on the other hand, has been referred to as a cool phenomenon since it takes place at low temperatures. It was first observed in biased semiconductors as early as 1907 by Round [42]. This early light producing semiconductor device was made of silicon carbide (carborundum). Researchers were working to fully characterize and exploit carborundum for radio frequency applications when electroluminescence was observed. Since that time, several researchers have observed and measured luminescence stimulated by electric charge from forward and reversed bias voltages. Initial occurrences of electroluminescence produced measured amounts that were very negligible, and concerted efforts ensued to increase luminescence levels. Arguably this was the birth of research and development work in understanding electo-optical devices. Over the past 100 years a large amount of work has been done to understand the mechanisms behind light generation in semiconductor materials.

Since the development of the first LED, making a more efficient device has been an ongoing effort. To do this, one must understand how these devices operate. There are two key factors that contribute to producing an efficient LED: Photon Generation (internal quantum efficiency) and Photon Radiation (extraction efficiency). Over the past 100 years since Round first observed electro-luminescence, much work has been done to optimize these two factors. To understand the impact each has on the overall device operation, one must understand how these factors are significant. For photon generation, understanding recombination theory is essential since it is the process that produces photons. Within this process are mechanisms that inhibit the

production of photons. These photon inhibitors need to be minimized, or eliminated from the device, to maximize its efficiency. The second factor, photon radiation, is a post recombination phenomenon. Once the photons are generated, they need to be expelled, or coupled, out of the device. The larger the number of photons coupled out of the device, the larger the output power of the device.

## A.2   Device Physics

*A.2.1   The Basic Diode Structure.*   Many improvements from what may be considered the basic device design have been made. These implemented changes have steadily increased the overall LED output power and efficiency. What follows is a discussion about the basic p-n junction diode at thermal equilibrium and under forward bias. Then attention will be given to several key improvements from the basic design that have been implemented through the years and are of value to this effort.

*A.2.1.1   The Homo-junction P-N Diode.*   A p-n junction diode is formed by growing a p-doped epitaxial layer of semiconductor material on an n-doped epitaxial layer, or substrate, forming a metallurgical junction between the respectively doped semiconductor materials. Since each layer, p and n, has an excess of loosely bound holes and electrons, contributed by acceptor ($N_a$), and donor ($N_d$) atoms, diffusion occurs across the junction. This diffusion is the process is one in which the loosely bound carriers reach equilibrium by moving to the lowest energy level allowed, within the newly formed two layer material. As the mobile particles diffuse, they leave behind immobile ionized atoms that have a net charge. Clearly, particles from the p-doped material will leave behind negatively charged ions, and particles from the n-doped side will leave behind positively charge ions as a result of the diffusion process. These immobile charges form a space charge region (SCR) that is depleted of any mobile carriers. An induced electric field results from the SCR. The electric field potential within the SCR, or depletion region, subsequently arrests the diffusion process by preventing any further carrier movement across the junction. At that point, newly

formed material system has reached equilibrium. At equilibrium, the system must obey the law of mass action which states that the product of the electron and hole concentrations in the material is constant, at a given temperature. This is modeled as

$$n_0 p_0 = n_i{}^2 \qquad (A.1)$$

where $n_0$ and $p_0$ are the electron and hole concentrations, and $n_i$ is the intrinsic carrier concentration.

The result of the diffusion process is modeled graphically by energy-band bending of the p-n structure at the metallurgical junction as shown in Figure A.3, where $E_C$ and $E_V$ are the conduction and valence bands, $E_F$ is the Fermi level, $E_F i$ is the intrinsic Fermi level, and $eV_{bi}$, $e\phi_p$ and $e\phi_n$ are all energy potential differences within the material system. The amount of bending represents the electrostatic potential difference ($eV_{bi}$ ) formed by the SCR, which prevents further diffusion by the mobile carriers. This built-in potential barrier, $V_{bi}$, is dependent on the amount of dopants in either material and is modeled by

$$V_{bi} = \frac{kT}{e} \ln \frac{N_A N_D}{n_i{}^2} \qquad (A.2)$$

where $N_A$ and $N_D$ are the acceptor and donor concentration, respectively, k is Boltzman constant, e is the charge of an electron, T is the temperature in Kelvin, and ni is the intrinsic carrier concentration of the semiconductor.

*A.2.1.2   The Hetero-junction P-N Diode.*     Like the homo-junction diode, the device is composed of doped semiconductor material that is epitaxially deposited or grown another material. Unlike the homo-junction device, the hetero-junction device is made of materials with different energy gaps, typically a wide bandgap material and a narrow bandgap material, as is the case with III-V materials like AlGaAs. By adding Al to GaAs, the bandgap can be changed. As the Al content in GaAs is increased, the bandgap widens. Consider an AlGaAs-GaAs system shown
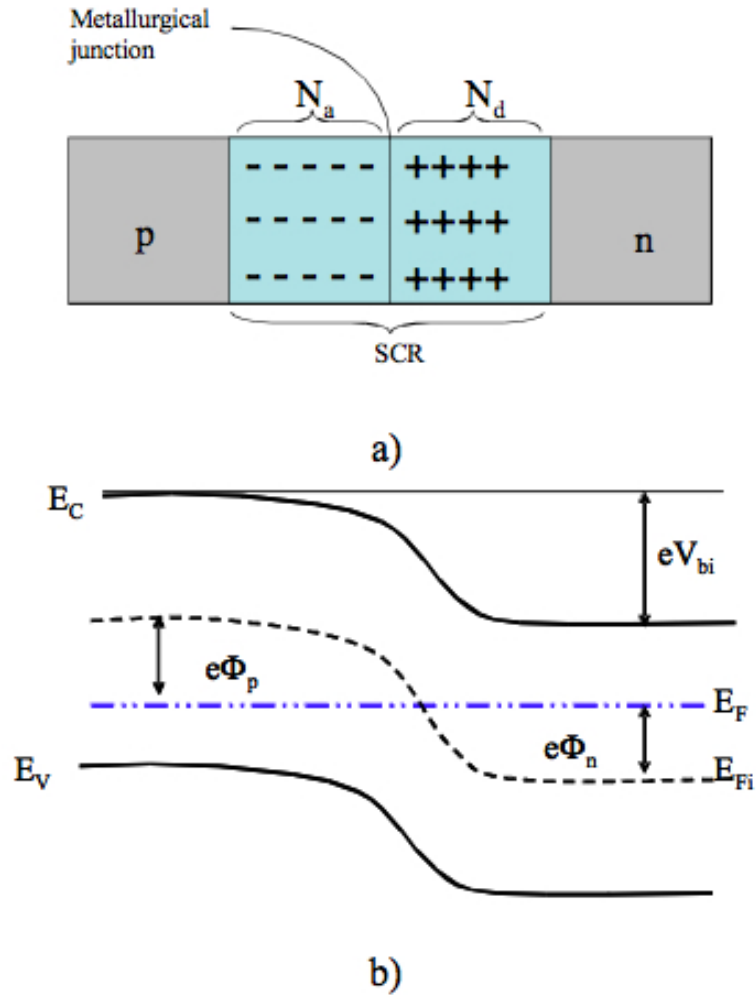
Figure A.1: Depiction of a p-n junction, showing (a) The space charge region and its constitutient charge at equilibrium; (b) the energy-band diagram of a p-n junction in equilibrium.
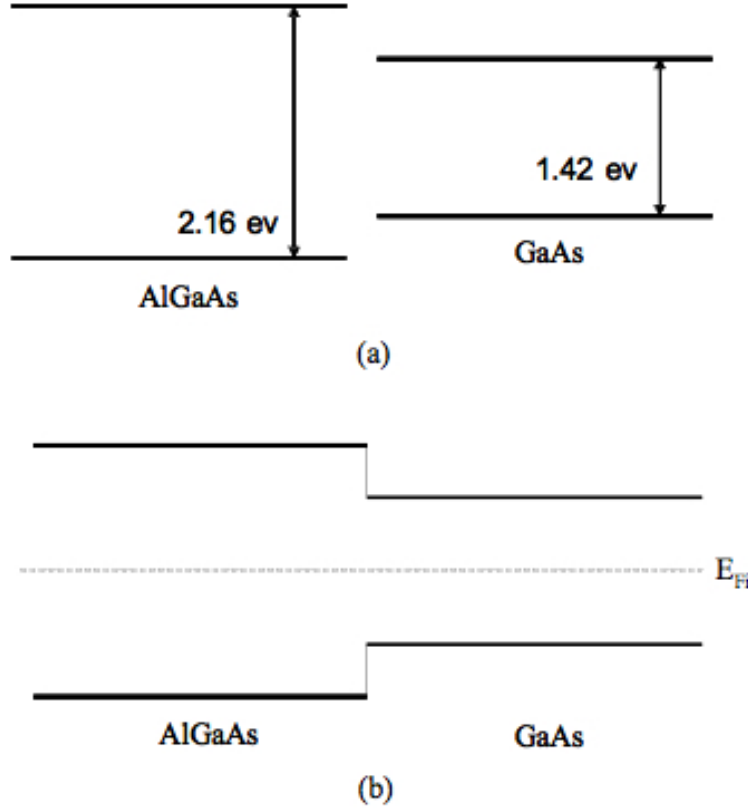
Figure A.2:    AlGaAs system (a) before and (b) junction formation.

in Figure A.2, which shows the notional material band structure before and after junction formation. This material system is widely due to lattice matching of AlAs and GaAs.

As with the homo-junction, the hetero-junction will establish equilibrium and the Fermi level will be constant throughout the entire material. Because the energy gaps are different, a potential barrier from the wide bandgap material to the narrow bandgap material will exist. This barrier can been used to increase the recombination probability, subsequently making a more efficient LED. This can be seen in a material system with AlGaAs-GaAs-AlGaAs epilayers, as shown in Figure A.3. The narrower energy gap GaAs creates the potential well characteristic of hetero-junction material systems. This type of material system is known as a double heterostructure (DH)

$E_{Fi}$
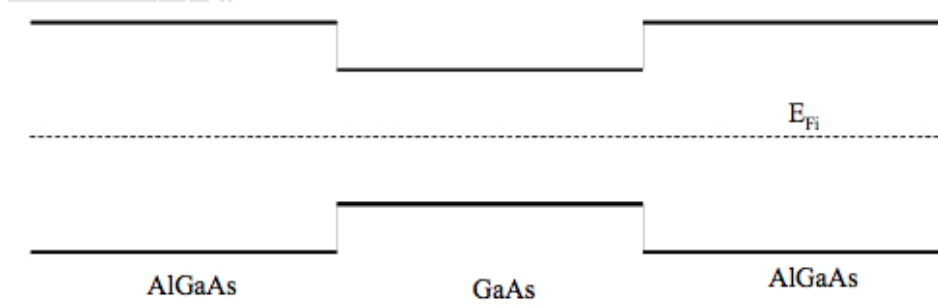
AlGaAs            GaAs            AlGaAs

Figure A.3:    Bandgap structure for AlGaAs-GaAs-AlGaAs system.

system. A doped hetero-junction diode will have the familiar band bending seen in
p-n junctions, along with the potential barrier well.

Fig 2-4. Bandgap structure for AlGaAs-GaAs-AlGaAs system.

*A.2.1.3  LED electrical characteristics.*    The application of a positive
potential across the p-n structure changes the energy-bands as shown in the doped
junctions. The applied voltage reduces the barrier voltage by $V_a$, and allows electrons
in the conduction band in the n type material to flow into the conduction band of
the p-type material; likewise with holes in the valence band of the p-type material.
Relative Fermi levels ($E_{Fn}$ and $E_{Fp}$) are created in the n-doped and p-doped materials
respectively once the structure is no longer in equilibrium. These levels adjust as the
number of electrons increase in the respective bands due to the positive potential
applied. As the holes and electrons flow across the junction, they enter oppositely
doped bulk regions. Now in the bulk regions, the injected carriers are small in number
with respect to the doping of the bulk material. These minority carriers ($\delta_{n,p}$) will
recombine with majority (bulk) carriers after they have traveled a certain distance
($L_{n,p}$) into the doped bulk material. This is the diffusion length. Depending on the
material and the type of dopant used, an average amount of time will elapse before
the minority carriers recombine with the majority carriers in the bulk regions. This
is the minority carrier lifetime ($\tau$) of the device. Minority carrier lifetime impacts
performance characteristics like device modulation speed. The application of a reverse
biased voltage can also produce current flow by different mechanisms. These include
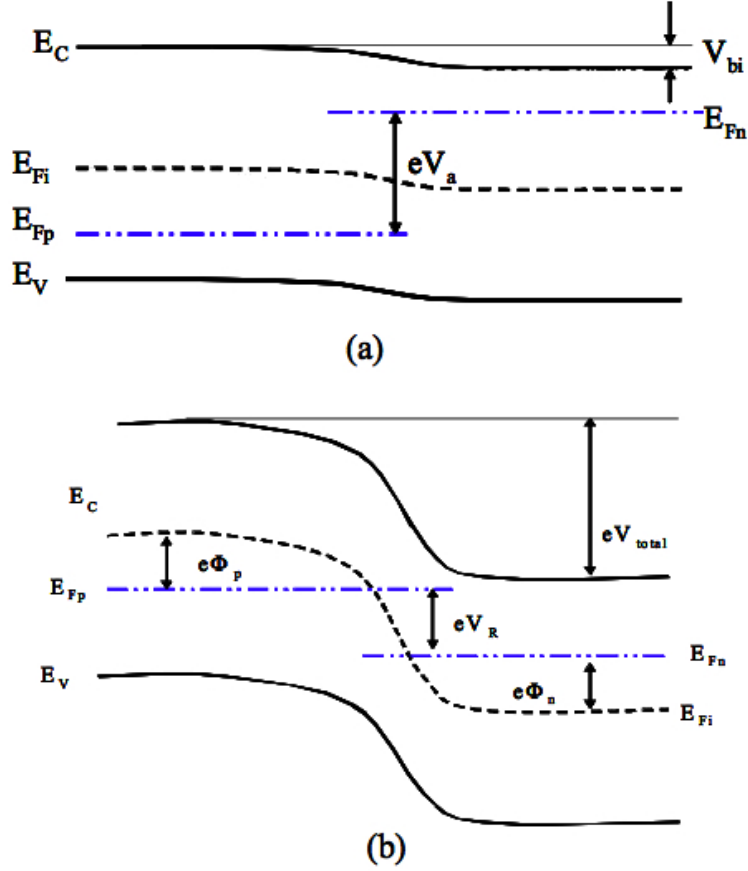
Figure A.4:    P-n junction structure under (a) forward and (b) reverse bias.

avalanche and tunneling phenomena call the Zener effect. A detailed explanation of the avalanche phenomena can be found in Sze [57]. An in-depth summary of the Zener effect will be discussed later in this dissertation. The forward and reverse bias condition band structures are shown in Figure A.4.

A typical current-voltage (I-V) characteristic curve is shown in Figure A.5. $V_a$ is a positive voltage potential applied across the p-n junction and $V_r$ is a reversed biased voltage. In the forward bias case, $V_a$ must be larger than $V_{bi}$ to induce current flow thought the device. Once this threshold is breached, the current through the device increases with increased applied voltage. Under reverse bias, a very small leakage current may exist. No significant current will flow under reverse bias until the reverse biased voltage reaches a certain value, $V_B$, the breakdown voltage. At this
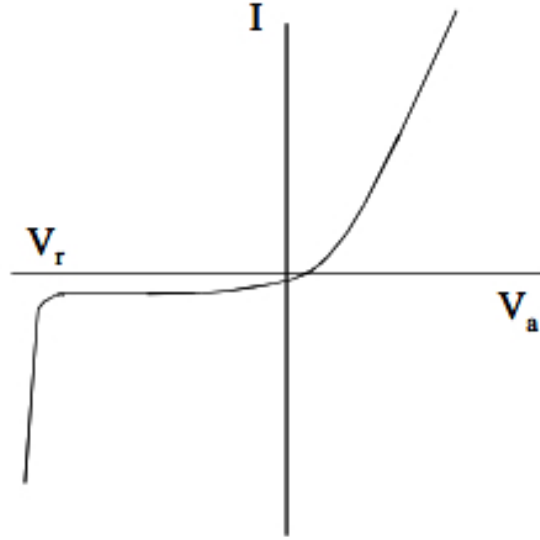
Figure A.5:    Ideal I-V characteristic of a typical p-n junction diode under forward and reversed bias.

value, current will flow through the diode until damage to the structure of the device is caused.

Under a forward bias, minority carriers will be injected across the SCR width, $W_D$, of a p-n junction, into the bulk majority material, will redistribute themselves (diffuse) and eventually recombine. The diffusion of the minority carriers into the majority bulk region occurs after traversing the SCR, over a characteristic length into the bulk material as shown in Figure A.7. $L_n$ and $L_p$ are the respective diffusion lengths of these minority carriers in this particular material. After the minority carriers have traveled the diffusion length, the probability of recombination is almost certain.

Diffusion constants ($D_n$ and $D_p$) can be inferred from the carrier mobilities of electrons and holes, respectively, in a semiconductor by the Einstein relation . The diffusion constant gives an indication of how well a carrier will redistribute themselves within a majority material. From this relationship, we can develop the following

(a)



(b)
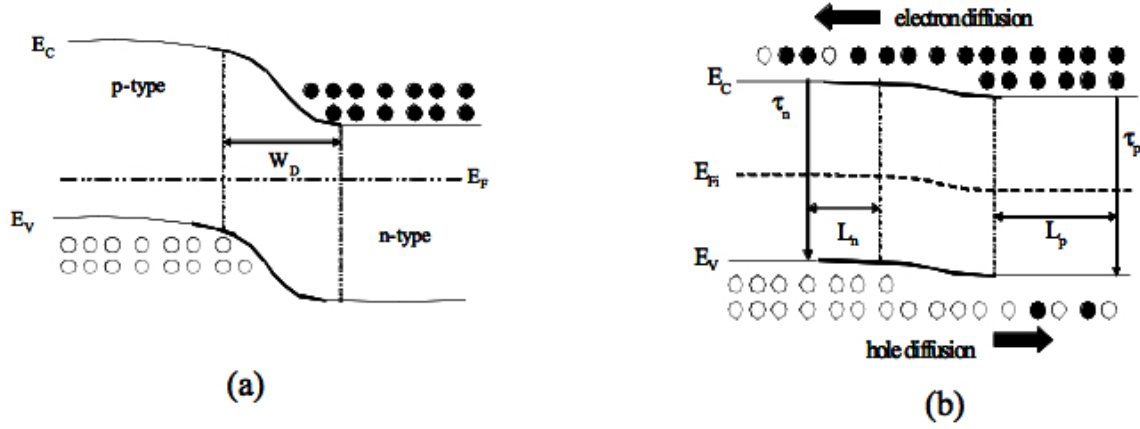
Figure A.6: Free carriers in the conduction and valence bands of p-n junction under (a) equilibrium condition and (b) under forward bias.

association

$$L_n = \sqrt{D_n \tau_n} \qquad (A.3)$$

$$P_n = \sqrt{D_p \tau_n} \qquad (A.4)$$

where $\tau_n$ and $\tau_p$ are the respective minority carrier lifetimes.

Since the underlying concern in designing light emitting devices is the creation of the optimum conditions for radiative recombination to occur, knowing the minority carrier distribution is essential. It is desirable to have a majority of carriers present in a confined region of the device because this proximity greatly increases the probability of recombination according to the basic recombination rate equation R = Bnp. Using hetero-junction material systems, the carrier distribution can be localized. By localizing the excited carrier distribution, we can statically increase the number of photons generated over a given period of time, hence the power generated. Figure A.7 shows a double heterostructure under forward bias. This diagram is a reproduction of one found in Schubert [46] . In this depiction, it is clear to see how the potential well formed by the difference in bandgap energy between the narrow and wide bandgap materials will trap holes and electrons in a well with width WDH. The carriers confined in the well are at an energy level equal to the narrow bandgap
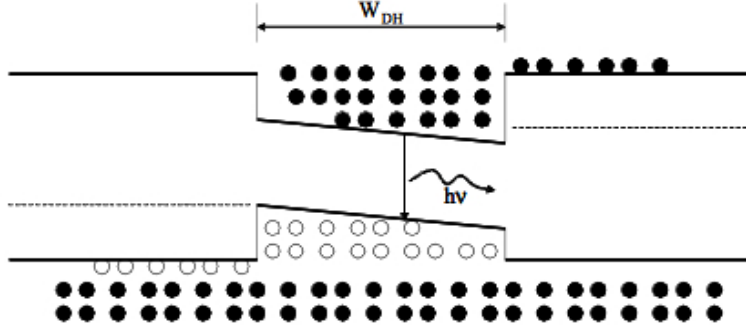
Figure A.7:    Double heterostructure p-n junction under forward bias.

energy. Recombination events have now been increased since many excited carriers are in close proximity and diffusion over long distances is not as likely to occur. Photons will be generated of energy corresponding to the narrow bandgap material. This structure is commonly seen in high intensity LEDs.

*A.2.2   Issues and Improvements concerning the Generation Factor.*    As discussed in earlier sections, when excess holes and electrons are in close proximity, they will recombine to re-establish equilibrium. Excess carriers can be brought into close proximity by biasing the junction. Recombination is the basis for current flow through the device and for energy emission. For light to be generated, we must have favorable conditions for recombination to occur. This section discusses some of the methods developed to promote favorable recombination conditions.

*A.2.2.1   Lattice Matching.*    The heterostructure system is constructed of different materials so the desired energy band profile can be formed. Building these structures is done by stacking semiconductor layers of desired thickness on top of on another. At the microscopic level, a junction between the different semiconductors is formed. There must be good agreement between the lattice constants of the materials used to minimize interface state formation at the junctions due to dangling bonds. Several III-V semiconductors have been studied and well characterized. One of the more familiar material systems is AlGaAs-GaAs. As mentioned earlier, the ability to

vary the lattice constant of the wide bandgap AlGaAs to closely coincide with the narrower GaAs material makes this combination a common choice for LED applications. Stacking can occur between layers of AlGaAs and GaAs with a small number of impurities created.

*A.2.2.2 Fabrication Process.* Impurities can be formed during semiconductor growth. Impurities create recombination centers within the device that can limit the number of photons generated, reducing the efficiency of the device. For this reason, extreme care must be taken to ensure the number of impurities is minimized. Fabrication methods have evolved over the years eventuating in the highly controlled techniques of today. These processes allow growth of monolayer thick, high purity semiconductor layers and structures. Producing high quality layers drives the number of recombination centers down. The presence of fewer recombination centers increases the probability of the desired radiative recombination to occur. Sze provides an extensive overview of how the number of recombination centers impact radiative recombination.

*A.2.2.3 Oxide Confinement.* Modern day processing techniques allow mass production of semiconductor devices. Since the topside of semiconductor wafers are used in many cases producing hundreds, if not thousands of devices at one time, electrical isolation is a must. As these devices are stacked structures, isolation can be achieved by etching isolation mesas under the devices. The outer surfaces of the mesas are where the semiconductor material is truncated, and hence dangling bonds exist. These bonds form surface states, which again, are luminescence killers. For this reason, it is essential to keep as many carriers as possible away from the outer edged of the mesa. That is, the ideal location for electrons and electrons is within the central portion of the device. To confine carriers, an oxidation step is included in the processing. This step oxidizes the edges of the semiconductor layers, which are left exposed due to the mesa etching. Oxidization converts the outer portion of

the semiconductor into an insulator, inhibiting electron flow in that portion of the material.

### A.2.2.4   Carrier loss within the double heterostructure (DH) system.

As mentioned earlier, one benefit of using a DH system is carrier confinement. Ideally, injected carriers, under low level injection (LLI), are confined between the barriers created by the wide bandgap materials on either side of the narrow bandgap material. Even though this barrier is usually much larger than kT, some confined carriers will escape over the barrier into the bulk material. This effect reduces the overall efficiency, since some of the potential photon generating carriers are lost. It has been shown that a significant leakage current can be generated from the carriers that escape confinement. The problem is exacerbated at high injection levels. Under high level injection (HLI) a much larger number of carriers are injected into the confinement region, which could lead to even larger leakage current from the confined region. The result is fewer carriers for radiative recombination and reduced device efficiency. To maintain the efficacy of the confined active region, blocking layers are added. Blocking layers are semiconductor layers with wider bandgaps than the wide bandgap material used in the DH system. Figure A.8 shows an example of an electron blocking layer. Since electrons have a higher mobility than holes, typically electron blocking layers are utilized.

### A.2.2.5   Resistance.   Although DH junctions offer a number of improvements over the homo-junction diode, there are some problems that are engendered by its use. One such problem is the resistance due to the interface of the DH. The origin of this resistance is depicted in Figure A.9. It shows a more accurate band diagram of a heterostructure material system taken from Schubert. Depicted is a narrow bandgap layer joined with a wide bandgap layer. Upon the junction formation, the electrons in the wide bandgap material will diffuse to the narrow bandgap material, causing the band bending. Any carriers that are moving must surmount or tunnel through the barrier to cross the junction. A large amount of thermal energy is needed is ei-
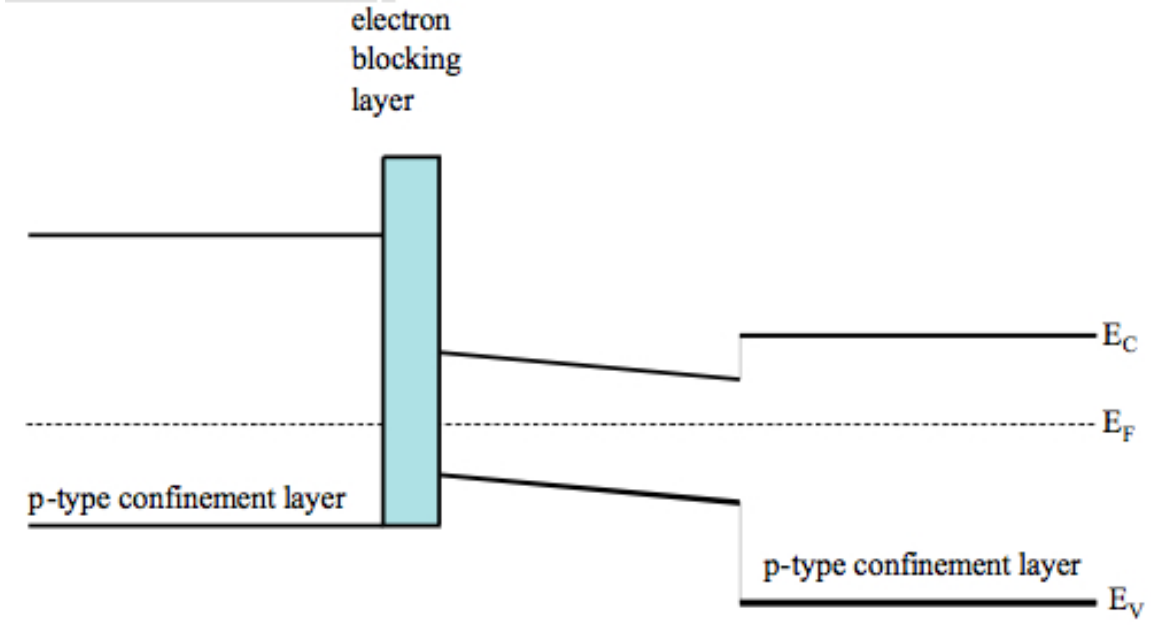
Figure A.8:     Notional depiction of dobpe DH system with an electron blocking layer inserted between the active region-bulk region junction.

ther case. Schubert states that grading the chemical composition of the material can eliminate the band discontinuities from the band structure as shown in Figure A.9. Eliminating these band discontinuities will allow more holes and electrons to diffuse into the potential well and increase the probability of radiative recombination.

*A.2.2.6 Active layer thickness.*     The narrow bandgap region of the DH is the active region. The width of the active region, i.e. the layer thickness, has a strong influence on the number of photons produced per carriers injected into this region. This ratio, photons to carriers injected, is the internal quantum efficiency, a familiar parameter used when describing the performance of LEDs. It has been shown that as the active region width is increased above the diffusion length of the carriers in the material, the benefit added by the potential well is negated. In contrast, if the active region becomes to thin, the potential well will overflow with carriers and some will be lost, arresting efficient recombination. Optimum well thicknesses for AlGaInP DH LED emitting at 565 nm of 0.15 to 0.75 $\mu$m have been reported .
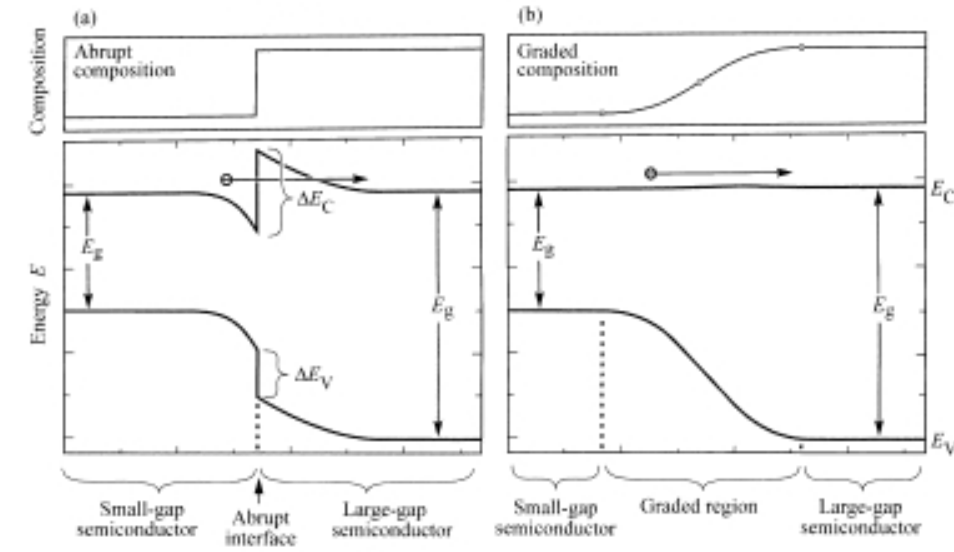
Figure A.9:    Band diagram of (a) abrupt n-n heterojunction and (b) graded hetero-junction of two semiconductors with different bandgap energy. The abrupt junction is more resistive than the graded junction due to the electron barrier at the abrupt junctions [47]

*A.2.2.7  Doping for improved internal efficiency.*    The various lay-ers of the stack can be doped, intentionally, to improve the radiative recombination probability (internal quantum efficiency). If intentional doping is employed, reaching optimum levels should be the goal. Consider the active region. If it is heavily doped, the p-n junction could be displaced at or near the junction defining the potential well. Under these circumstances, carrier spill over into the bulk region will occur and the efficiency will be reduced . For this reason, the active region is typically lightly doped or not doped at all. Figure A.10 shows a doping profile versus luminous efficiency for AlGaInP DH LED emitting at $\lambda$=565 nm [37]. Typically, the active region is left undoped, but levels of $10^{16}$ to $10_{17}$ cm$^{-3}$ for n and p type doping are not uncommon. Since the mobility of holes is lower than that of electrons, intentionally doped active layers are p doped to cause a more evenly distributed carrier population. Active re-gions have residual doping on the order of $10^{15}$ to $10^{16}$ cm$^{-3}$. For this reason, the confinement layers are doped.
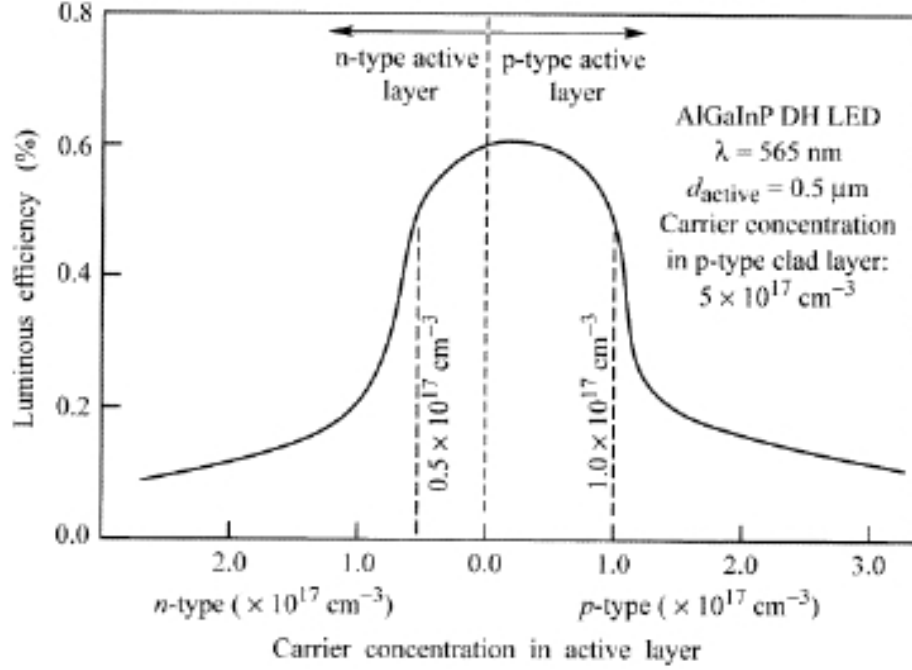
Figure A.10: Doping profile versus luminous efficiency for AlGaInP DH LED emitting at $\lambda$=565 nm (after Sugawara et. al.., 1992) [55]

When doping confinement layers, one must also seek to reach optimum doping levels. Since it is desirable that the resistance of the confinement layers are low, relatively high doing levels are used. Large resistance increases the device temperature, which reduces the radiative recombination events. Higher doping levels also counter the effect of the unintentionally doped active region. The confinement layer must have a higher doping than the active layer to define the location of the p-n junction. It has been shown15 that optimum doping ranges for confinement regions are from $10^{16}$ to 2 x $10^{17}$ cm$^{-3}$ for n type, and 5 x $10^{17}$ to 2 x$10^{18}$ cm$^{-3}$ for p-type materials.

*A.2.3   Issues Concerning the Radiation Factor.*   Once photons are generated, a maximum number must be extracted from the device into the radiating medium, which could be air or an optical fiber. The degree of success with which one can produce the most desirable extraction condition can be quantified by the quantum efficiency. The ratio between the number of photons emitted from the active region

per second to the number of photons injected into the LED active region per second is the internal quantum efficiency ($\eta_{int}$). The ratio of the number of photons emitted into space per second to the number of photons emitted from the active region per second is the extraction efficiency ($\eta_{extraction}$). The ratio of the number of photons emitted into space to the number of electrons injected into the LED active region is the external quantum efficiency ($\eta_{ext}$). Lastly, the overall efficiency, called the wall plug efficiency, is the ratio of optical output power to electrical input power. Creating conditions that make these ratios as large as possible is the goal of optimizing the radiation factor. Several photon annihilators that limit the above efficiencies exist in LEDs and a great deal of research has been done to control them. Some are discussed below along with the mitigation techniques.

*A.2.3.1 Shaping the device surface.* Characteristically, only a fraction of the photons produced will escape the device. Schubert [46] reports that the total power of the light being emitted from the device is only a fraction of the light produced by the active region. This relationship is modeled as

$$P_{escape} = P_{source} \frac{2\pi r^2 (1 - cos\phi_c)}{4\pi r^2} \tag{A.5}$$

where $P_{ecape}$ and $P_{source}$ are the powers leaving the device and produced by the active region respectively, $\phi_c$ is the angle of the escape cone, and r is the distance from the source to a point inside the semiconductor, in this case the surface. The parameter $\phi_c$ determines the shape of the emission pattern exiting the device. Figure A.11 from Schubert shows three surfaces and their polar plots. The plots are normalized to unity. Notice the decrease in emission percentage with angle for the planar LED. This plot is indicative of a Lambertian emission pattern. Also notice that a hemispherical LED surface is optimum for maximum photon emission at angles up to $\theta = 90^o$. Although the hemispherical surface allows emission for larger angles, this surface is difficult to fabricate. This shaping concept can and has been extended to the semiconductor die. The optimum LED with a point source would be spherical in shape, but again, very
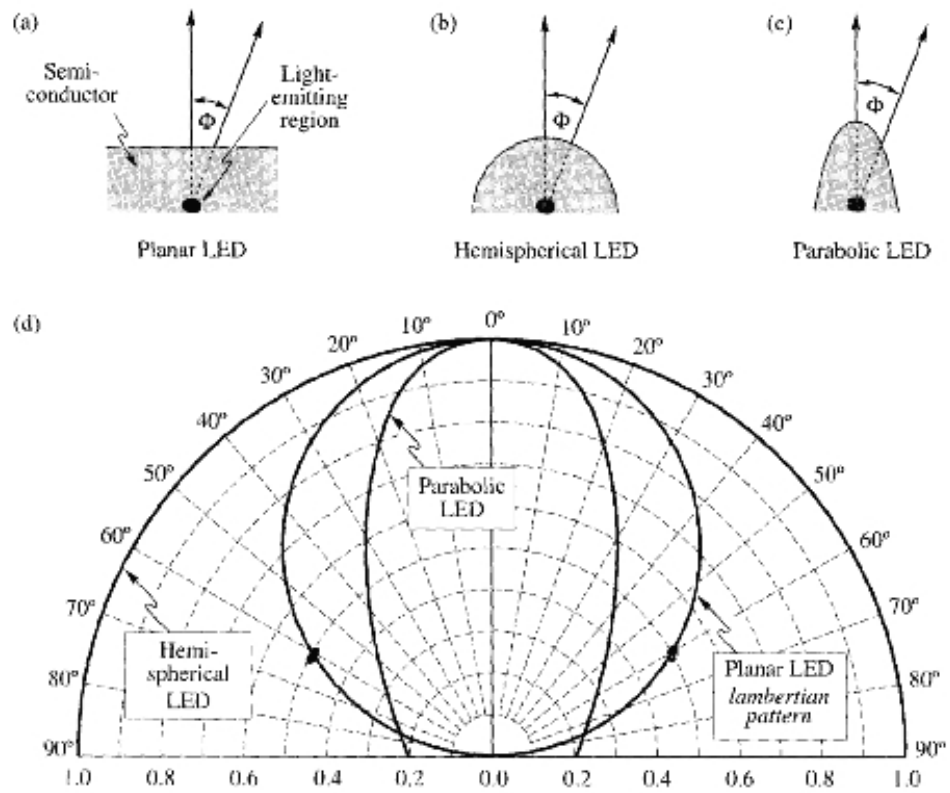
Figure A.11:    Some commonly used LED surfaces and their polar plots. The surface shape determines the emission pattern. Figure was taken from Schubert [46]

Table A.1:    Some typical anit-reflection coatings.

| Dielectric Material | Refractive Index | Transparency Range |
|---------------------|------------------|--------------------|
| SiO2 (Silica) | 1.45 | > 0.15 $\mu$m |
| Al2O3 (alumina) | 1.76 | > 0.15 $\mu$m |
| TiO2 (titania) | 2.50 | > 0.35 $\mu$m |
| Si3N4 (silicon nitride) | 2.00 | > 0.25 $\mu$m |
| ZnS (zinc sulphide) | 2.29 | > 0.34 $\mu$m |
| CaF2 (calcium fluoride) | 1.43 | > 0.12 $\mu$m |

difficult to fabricate. Several attempts to adequately shape semiconductor dyes have been made. These include hemispherical domes [4], inverted and truncated cones [11] . Two of the more common shaped devices include the rectangular parallelepiped device (edge emitter) and the cylindrical device (surface emitter). Roughened or textured surfaces have also been implemented to increase the extraction efficiency of LEDs.

*A.2.3.2   Antireflection layers.*    Light traveling in media with high index of refraction incident on a boundary with media of low index of refraction will experience reflection. Such is the case with high index semiconductors boundary with air. To mitigate this problem, antireflection (AR) layers are placed on the surface of the semiconductor. The AR coating is an intermediate index material which reduces the amount of reflection occurring back into the device. Some typical AR coatings are shown in Table A.1 [39] . The effect of AR coatings can be modeled by the reflectance equation given by

$$R = \frac{(n_s - n_{air})^2}{(n_s + n_{air})^2} \tag{A.6}$$

where R is the total power reflected from the air-semiconductor boundary. This equation shows that R increases as the difference between the indices of the air and the semiconductor is increased.

*Appendix B.  Spiricon 980M IR Camera Datasheet*

# Camera Selection Chart

Silicon CCD Cameras λ = 190nm to 1.1μm

| MODEL (1)<br>( ) = Numbered Notes | Spiricon<br>SP-980M | Spiricon<br>STC-700 | COHU 4812<br>(6) | PULNIX TM-7/<br>TM-6<br>(9,10) | UNITS | CONDITIONS |
|---|---|---|---|---|---|---|
| Number of Elements | 768 x 494 | 768 x 494 | 754 x 488 | 768x494/<br>752x582 | Pixels | H X V |
| LBA-PC Maximum<br>Digitized Resolution | 640 x 480 | 640 x 480 | 632 x 480 | 640 x 480/<br>756 x 572 | Pixels | H X V |
| Element Pitch μm<br>(21) | 8.4 x 9.8 | 11.6 x 13.5 | 11.5 x 13.5 | 8.4x9.8/<br>8.6x8.3 | μm | H X V |
| Area mm | 6.5 x 4.8 | 8.9 x 6.7 | 8.7 x 6.6 | 6.4 x 4.8/<br>6.5 x 4.7 | mm | H X V |
| Max Viewable Beam, mm<br>(2) | 4.7 | 6.5 | 6.4 | 4.7/4.7 | mm | 100% of Beam |
| Material | Silicon CCD | Silicon CCD | Silicon CCD | Silicon CCD | | |
| Spectral Response nm<br>(7) | 190-1100 | 190-1100 | 190-1310<br>(26) | 190-1100 | nm | |
| Readout | Interline Transfer<br>Interlaced | Interline Transfer<br>Interlaced | Frame Transfer<br>Interlaced | Interline Transfer<br>Interlaced | | |

### CW OPERATION

| | | | | | | |
|---|---|---|---|---|---|---|
| Full Video μW/cm² | 0.3 | 0.3 | 0.2 | 0.3 | μW/cm² | 632.8 nm |
| S/N (5) dB | 58 | 54 | 60(8) | 55 | dB | Full Video/RMS<br>Temporal Noise |

### PULSED OPERATION

| | | | | | | |
|---|---|---|---|---|---|---|
| Full Video nJ/cm² | 4 | 4 | 3 | 5 | nJ/cm² | 632.8 nm |
| Max. Pulse Rate (3) Hz | 30 | 30 | 60 | 30/25 | Hz | |

### MECHANICAL SPECIFICATIONS

| | | | | | | |
|---|---|---|---|---|---|---|
| Dimension Inch | 1.33 x 1.46 x 2.54 | 1.7 x 1.2 x 2.9 | 2.72 x 2.3 x 5.5 | 1.6 x 1.6 x 3.0 | Inch | H X W X D |
| Weight Oz | 3 | 3.4 | 15.5 | 6 | Oz | |

### APPLICATIONS (R=Recommended/Function Available)

| | | | | | |
|---|---|---|---|---|---|
| Electronic Shutter (4) | R | R | | R | |
| Full Resolution | R(10) | R(9,10) | R (CW only) (6) | R (9,10) | |
| Low Noise | | | R (Use 10-bit or<br>12-bit digitizer) | | |
| Interface Type | RS-170 | RS-170 | RS-170 | RS-170 TM-7<br>CCIR TM-6 | |
| Integration | | | | | |
| Remote Head | R(11) | R(11) | | R (11) | |
| Long Wavelength<br>(>1100 nm) | | | R(26) | | |
| Short Pulse YAG<br>at 1.06 μm | | | R(10) | | |
| CE Mark | R | R | R | R | |

*Appendix C.  Preliminary Test Devices Growth Descriptions*

Table C.1: Detailed presentation of each sample. Shown are variations made between each sample growth. Small modifications were made to observe the impact on TJ slope. All doping concentrations are in units $cm^{-3}$, and all temperature growths are in $^oC$. The labels in parenthesis are the dopants used in the GaAs material.

| G2-3255 | Temperature of Growth 680/606–575/528 $^oC$ |
|---|---|
| 5E18 n (Si) doped layer | 1000 Åcontact layer |
| 8E18 n (Si) doped layer | 200 Å$\delta$-doped layer |
| 1E20 p (Si) doped layer | 200 Å |
| 6E19 p (Si) doped layer | 500 Åcontact layer |
| G2-3256 | Temperature of Growth 680/606–575/528 $^oC$ |
| 5E18 n (Si) doped layer | 1000 Åcontact layer |
| 8E18 n (Si) doped layer | 200 Å$\delta$-doped layer |
| 1E20 p (Si) doped layer | 200 Å |
| 6E19 p (Si) doped layer | 500 Åcontact layer |
| G2-3257 | Temperature of Growth 680/606–575/528 $^oC$ |
| 5E18 n (Si) doped layer | 1000 Åcontact layer |
| 8E18 n (Si) doped layer | 200 Å$\delta$-doped layer |
| | As flow for 30 s inserted |
| 1E20 p (Si) doped layer | 200 Å |
| 6E19 p (Si) doped layer | 500 Åcontact layer |
| G2-3258 | Temperature of Growth 680/606–575/528 $^oC$ |
| 5E18 n (Si) doped layer | 1000 Åcontact layer |
| 8E18 n (Si) doped layer | 200 Å$\delta$-doped layer |
| (U) GaAs | 20 Åsmoothing layer |
| 1E20 p (Si) doped layer | 200 Å |
| 6E19 p (Si) doped layer | 500 Åcontact layer |
| G2-3259 | Temperature of Growth 680/606$^oC$ |
| 5E18 n (Si) doped layer | 1000 Åcontact layer |
| | As flow removed from each $\delta$-doped layer |
| 8E18 n (Si) doped layer | 200 Å$\delta$-doped layer |
| | As flow added here for 30 sec |
| 1E20 p (Si) doped layer | 200 Å |
| 6E19 p (Si) doped layer | 500 Åcontact layer |
| G2-3260 | Temperature of Growth 680/606$^oC$ |
| 5E18 n (Si) doped layer | 1000 Åcontact layer |
| | As flow removed from each $\delta$-doped layer |
| 8E18 n (Si) doped layer | 200 Å$\delta$-doped layer |
| (U) GaAs | 20 Åsmoothing layer |
| 1E20 p (Si) doped layer | 200 Å |
| 6E19 p (Si) doped layer | 500 Åcontact layer |

*Appendix D.   OSRAM Data Sheet*

## IR DRAGON
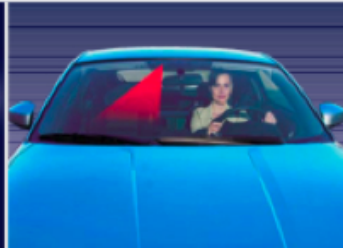


*IR DRAGON.*  *Seat occupancy.*  *Surveillance system.*

### Advantages

The IR DRAGON benefits are unique in the infrared galaxy.

### Intergalactic performance

Thinfilm technology allows the new IR DRAGON to achieve a wall plug efficiency of approx. 30 %. This corresponds to approximately half the value that can be achieved using semiconductor lasers and is superior to using spontaneous emitters.

### A star in reliability

The new IR DRAGON also has an extraordinarily long lifetime in DC mode, showing extremely stable behaviour. Furthermore, the package demonstrates a very good thermal design.

### Easy design and management

The top emitting die allows easy design of external lenses.

### A galaxy of applications

The wavelength is designed for all CMOS/CCD camera applications. Additionally the IR DRAGON is qualified for automotive applications.

### No visible red glow

The 940 nm version of the IR Dragon offers enough power for the camera sensor. At the same time, it does not emit any red light.

### Features

Explore the intergalactic features of the new IR DRAGON.

- IR DRAGON has dimensions of 11.0 x 6.0 x 1.8 mm.
- The packages come with two wavelengths of 850 nm and 940 nm.
- The IR DRAGON demonstrates high efficiency in a very small package with an emission area of 1 x 1 mm.
- Furthermore, the package is characterized by low thermal resistance and allows a maximum DC current of 1 A.
- Naturally, IR DRAGON is RoHS compliant and qualified for automotive applications.

### Applications

The new IR DRAGON is suited for all infrared illumination projects. With this product, you can leap into a new galaxy of applications.

The following examples are based on infrared illumination:

### Automotive
- Pre-crash sensor
- Seat occupancy

### Industrial
- Surveillance system (CCTV)
- Machine security systems

### Consumer
- Night vision flashlights for camera

### Technical Data
#### SFH 4230
Max. forward current (DC mode): 1 A
Thermal resistance: 15 K/W
Total radiant flux (@ If = 1 A): 440 mW
Total power consumption: 1.8 W
Wavelength: 850 nm
Active chip area: 1 mm$^2$

#### SFH 4231
Max. forward current (DC mode): 1 A
Thermal resistance: 15 K/W
Total radiant flux (@ If = 1 A): 500 mW
Total power consumption: 1.8 W
Wavelength: 940 nm
Active chip area: 1 mm$^2$

### IR DRAGON on Internet:
www.osram-os.com/ir-dragon/

**Opto Semiconductors**

**OSRAM**

*Appendix E.  Detailed Device Variance Data*

| current | 110 μm device | | 140 μm device | | 170 μm device | | 200 μm device | | 240 μm device | |
|---|---|---|---|---|---|---|---|---|---|---|
| mA | mean | variance | mean | variance | mean | variance | mean | variance | mean | variance |
| 0 | 0 | 0 | 0 | 0 | 0 | 0 | 0 | 0 | 0 | 0 |
| 10 | 13.66 | 0.02 | 6.24 | 0.10 | 0.91 | 0.15 | 1.96 | 0.13 | 0.78 | 0.18 |
| 20 | 43.11 | 0.03 | 21.47 | 0.06 | 3.70 | 0.08 | 7.32 | 0.14 | 3.54 | 0.14 |
| 30 | 78.97 | 0.04 | 40.33 | 0.07 | 7.32 | 0.14 | 14.53 | 0.14 | 7.41 | 0.26 |
| 40 | 37.41 | 0.05 | 60.37 | 0.08 | 11.09 | 0.14 | 22.40 | 0.19 | 11.58 | 0.28 |
| 50 | 50.00 | 0.05 | 82.19 | 0.08 | 15.24 | 0.17 | 30.43 | 0.18 | 16.03 | 0.29 |
| 60 | 63.43 | 0.06 | 31.87 | 0.10 | 19.47 | 0.19 | 38.67 | 0.16 | 20.57 | 0.26 |
| 70 | 76.65 | 0.06 | 40.00 | 0.12 | 23.65 | 0.19 | 2.90 | 0.31 | 25.36 | 0.25 |
| 80 | 89.66 | 0.06 | 46.34 | 0.12 | 27.88 | 0.19 | 3.67 | 0.33 | 30.65 | 0.22 |
| 90 | 5.46 | 0.17 | 54.57 | 0.12 | 32.15 | 0.18 | 4.35 | 0.43 | 2.25 | 0.72 |
| 100 | 6.15 | 0.14 | 59.08 | 0.11 | 35.83 | 0.17 | 4.96 | 0.41 | 2.63 | 0.66 |
| 110 | 6.86 | 0.12 | 4.57 | 0.19 | 40.70 | 0.17 | 5.73 | 0.43 | 3.01 | 0.74 |
| 120 | 7.68 | 0.11 | 5.00 | 0.23 | 44.00 | 0.16 | 6.48 | 0.49 | 3.44 | 0.81 |
| 130 | 8.35 | 0.15 | 5.47 | 0.28 | 3.31 | 0.47 | 6.91 | 0.47 | 3.79 | 0.75 |
| 140 | 8.97 | 0.13 | 6.10 | 0.27 | 3.41 | 0.49 | 7.64 | 0.45 | 4.18 | 0.78 |
| 150 | 9.77 | 0.13 | 6.57 | 0.25 | 3.76 | 0.42 | 8.28 | 0.48 | 4.59 | 0.73 |
| 160 | 10.25 | 0.15 | | | 4.09 | 0.48 | 8.85 | 0.46 | 4.92 | 0.74 |
| 170 | 10.97 | 0.14 | | | 4.20 | 0.48 | 9.42 | 0.47 | 5.32 | 0.75 |
| 180 | 11.18 | 0.15 | | | 4.53 | 0.44 | 9.85 | 0.44 | 5.66 | 0.70 |
| 190 | 12.10 | 0.15 | | | 4.83 | 0.48 | 10.30 | 0.45 | 5.88 | 0.70 |
| 200 | 12.49 | 0.17 | | | 5.01 | 0.50 | 10.91 | 0.44 | 6.38 | 0.70 |
| 210 | 13.03 | 0.16 | | | 5.07 | 0.50 | 11.42 | 0.44 | 6.76 | 0.65 |
| 220 | 13.48 | 0.17 | | | 5.51 | 0.48 | 12.57 | 0.41 | 6.99 | 0.65 |
| 230 | 13.80 | 0.15 | | | 5.64 | 0.48 | 13.09 | 0.41 | 7.30 | 0.65 |
| 240 | 13.76 | 0.14 | | | 5.84 | 0.53 | 13.49 | 0.42 | 7.65 | 0.62 |
| 250 | | | | | 6.18 | 0.54 | 14.02 | 0.40 | 7.94 | 0.61 |
| 260 | | | | | 6.34 | 0.54 | 13.99 | 0.39 | 8.24 | 0.61 |
| 270 | | | | | | | 14.94 | 0.38 | 8.44 | 0.60 |
| 280 | | | | | | | 14.91 | 0.38 | 8.80 | 0.57 |
| 290 | | | | | | | 16.07 | 0.38 | 9.20 | 0.56 |
| 300 | | | | | | | 16.52 | 0.36 | 9.19 | 0.57 |
| 310 | | | | | | | 16.66 | 0.36 | 9.54 | 0.54 |
| 320 | | | | | | | 16.70 | 0.36 | 9.96 | 0.53 |
| 330 | | | | | | | | | 9.89 | 0.54 |
| 340 | | | | | | | | | 9.99 | 0.53 |
| 350 | | | | | | | | | 10.39 | 0.53 |
| average variance | 0.11 | | 0.15 | | 0.34 | | 0.37 | | 0.56 | |

Figure E.1: Shown is the mean and variance values for each set of devices, according to their sizes. A variance of 0.20 has been identified as a "good" uniformity indicator. For each size group, the point where the variance surpasses 0.02 is indicated. At that point, the current density is such that the TJ in the devices of that size, cannot sustain adequate current spreading, and uniformity is impacted. Also shown is the overall average variance of each device over the safe current injection range for each device of that size.

## Appendix F.  Parametric Study Plots

The graphs in this Appendix shows SNR vs LED Power, varying $\eta_{det}$, $D_{optic}$, $\tau_{int}$, and $\theta$. A dotted line is drawn across each plot, indicating where the desired SNR (20 dB) exist on the plot. The plots are grouped accordingly:

- In Figures 1-3, $\tau$ is set at 0.33, 0.033, and 0.0033 respectively, while $\theta = 1.54$ rad, and $\eta = 0.3$.

- In Figures 4-6, $\tau$ is set at 0.33, 0.033, and 0.0033 respectively, while $\theta = 1.54$ rad, and $\eta = 0.9$.

- In Figures 7-11, $\tau$ is set at 0.33, 0.033, 0.0033, 0.00033, and 0.000033 respectively, while $\theta = \pi/4$ rad, and $\eta = 0.3$.

- In Figures 12-16 $\tau$ is set at 0.33, 0.033, 0.0033, 0.00033, and 0.000033 respectively, while $\theta = 1.54$ rad, and $\eta = 0.9$.

In each case, several $D_{optic}$ values are given, which represent the SNR achieved with an optic of that size. As the various parameters are changed, the SNR achieved is altered.

Figure F.1:    SNR vs LED power plot with $\theta = 1.54$ rad, $\eta = 0.3$, $\tau = 0.33$.
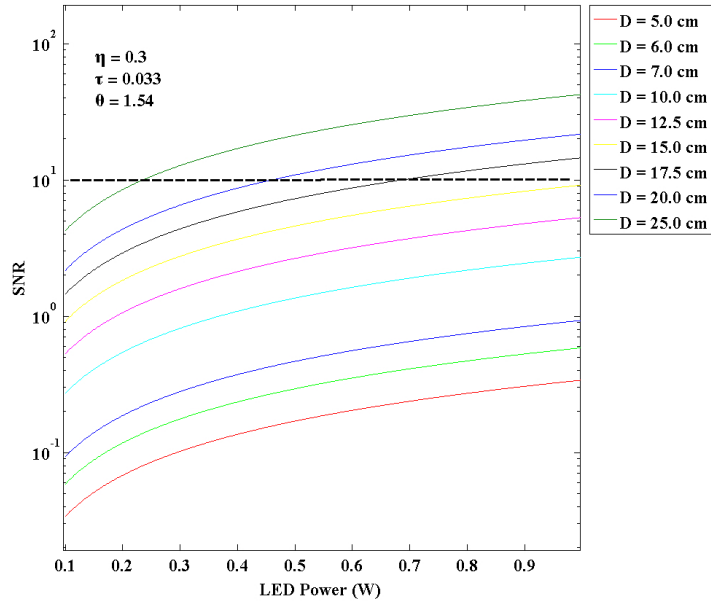


Figure F.2:    SNR vs LED power plot with $\theta = 1.54$ rad, $\eta = 0.3$, $\tau = 0.033$.

sn
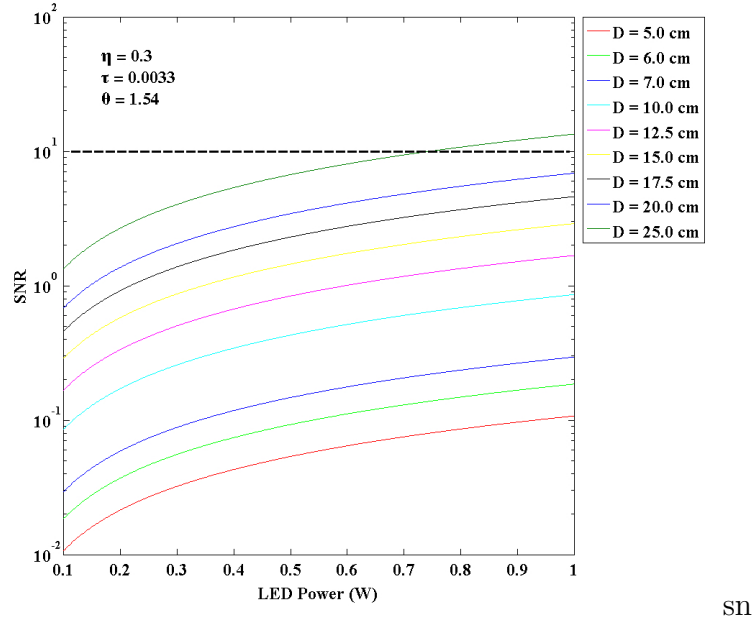
Figure F.3:    SNR vs LED power plot with $\theta = 1.54$ rad, $\eta = 0.3$, $\tau = 0.0033$.
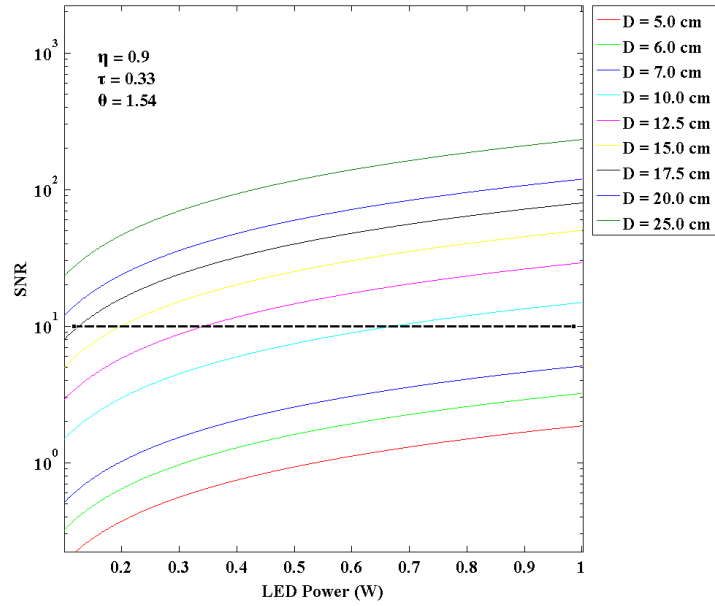


Figure F.4:    SNR vs LED power plot with $\theta = 1.54$ rad, $\eta = 0.9$, $\tau = 0.33$.
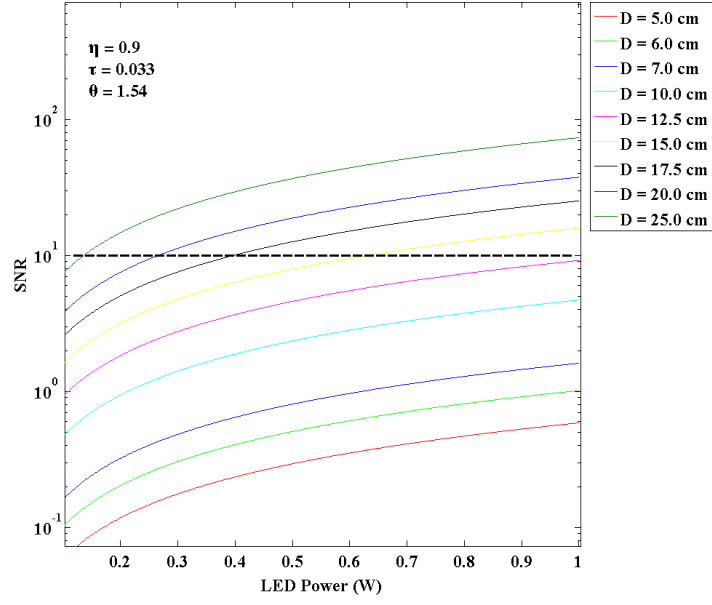
Figure F.5:     SNR vs LED power plot with $\theta = 1.54$ rad, $\eta = 0.9$, $\tau = 0.033$.
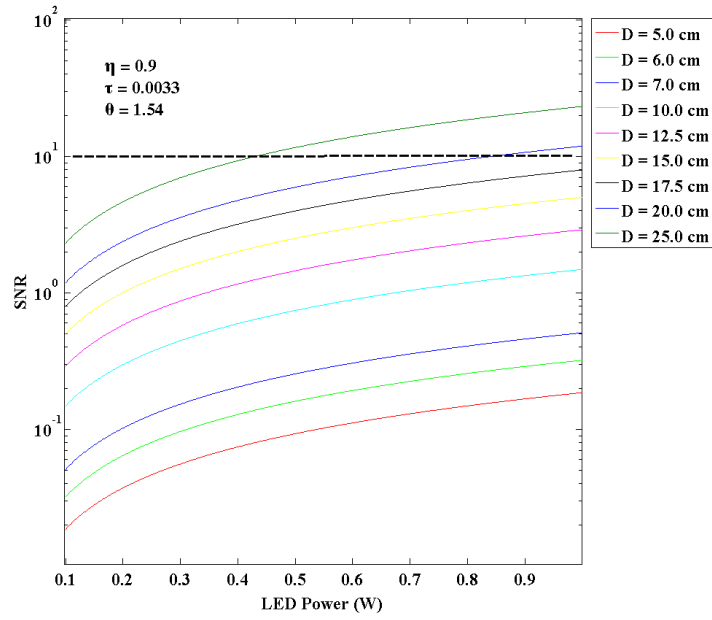


Figure F.6:     SNR vs LED power plot with $\theta = 1.54$ rad, $\eta = 0.9$, $\tau = 0.0033$.
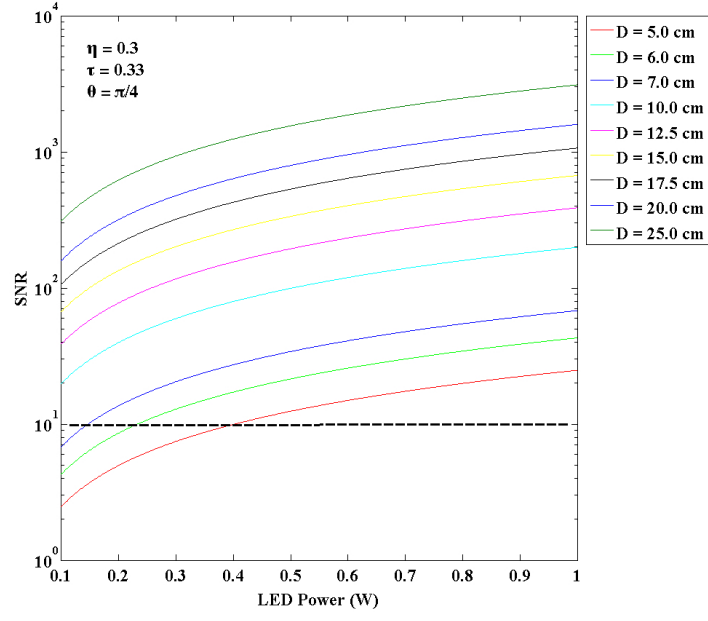
Figure F.7:    SNR vs LED power plot with $\theta = \pi/4$ rad, $\eta = 0.3$, $\tau = 0.33$.
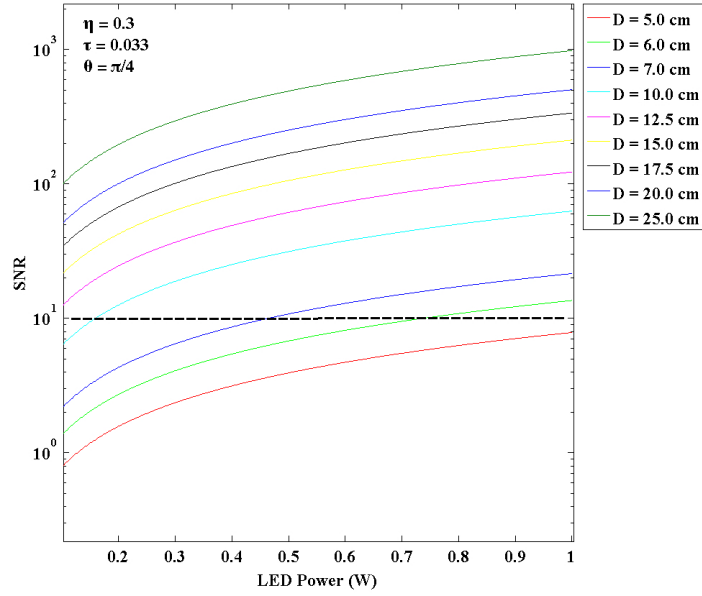


Figure F.8:    SNR vs LED power plot with $\theta = \pi/4$ rad, $\eta = 0.3$, $\tau = 0.033$.
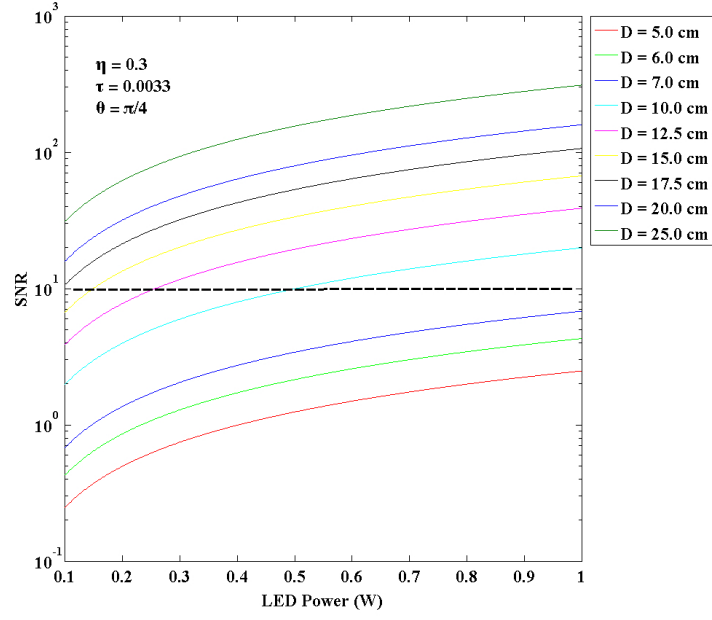
Figure F.9:    SNR vs LED power plot with $\theta = \pi/4$ rad, $\eta = 0.3$, $\tau = 0.0033$.
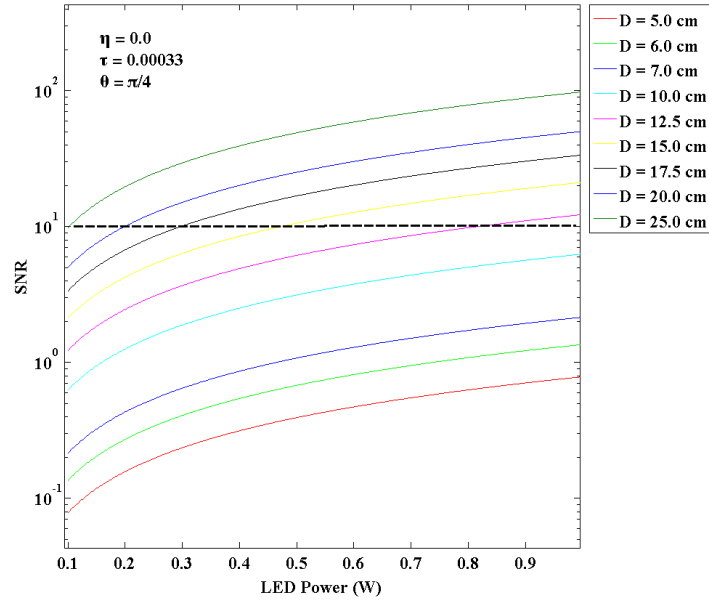


Figure F.10:    SNR vs LED power plot with $\theta = \pi/4$ rad, $\eta = 0.3$, $\tau = 0.00033$.
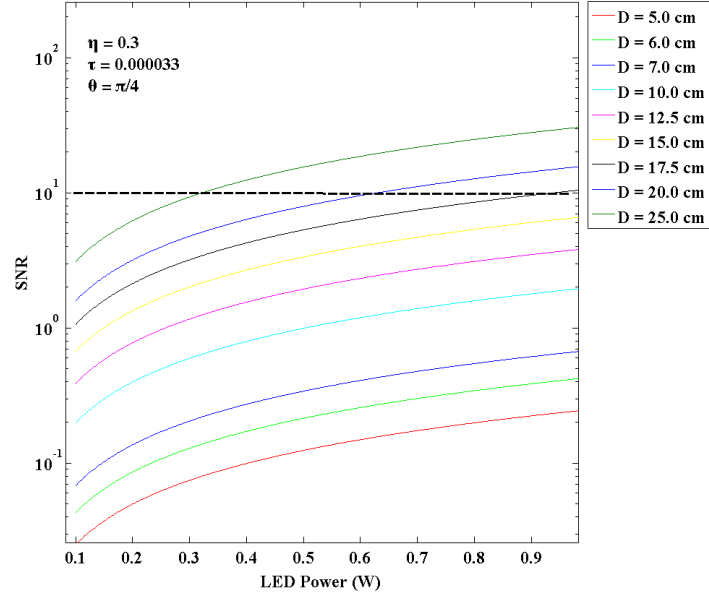
Figure F.11:    SNR vs LED power plot with $\theta = \pi/4$ rad, $\eta = 0.3$, $\tau = 0.000033$.
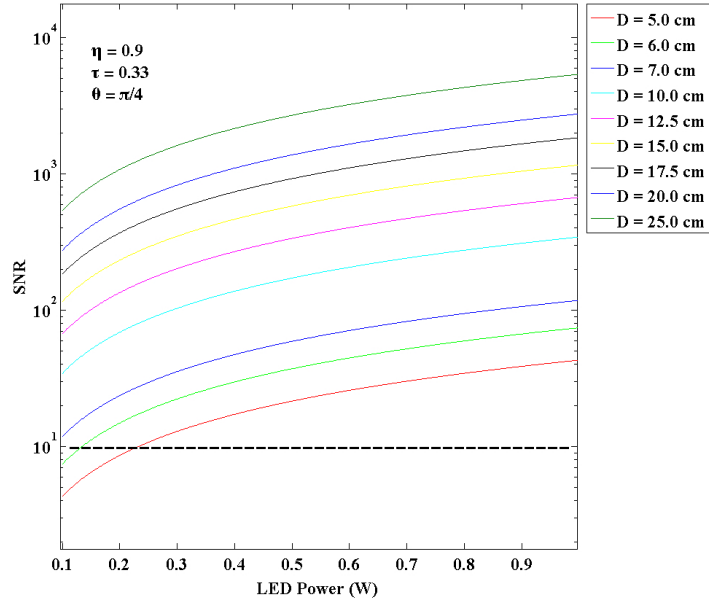


Figure F.12:    SNR vs LED power plot with $\theta = \pi/4$ rad, $\eta = 0.9$, $\tau = 0.33$.

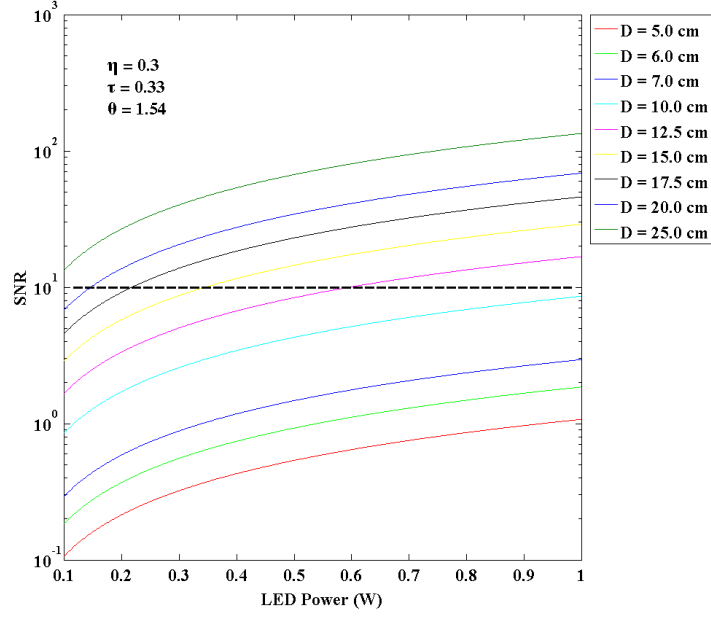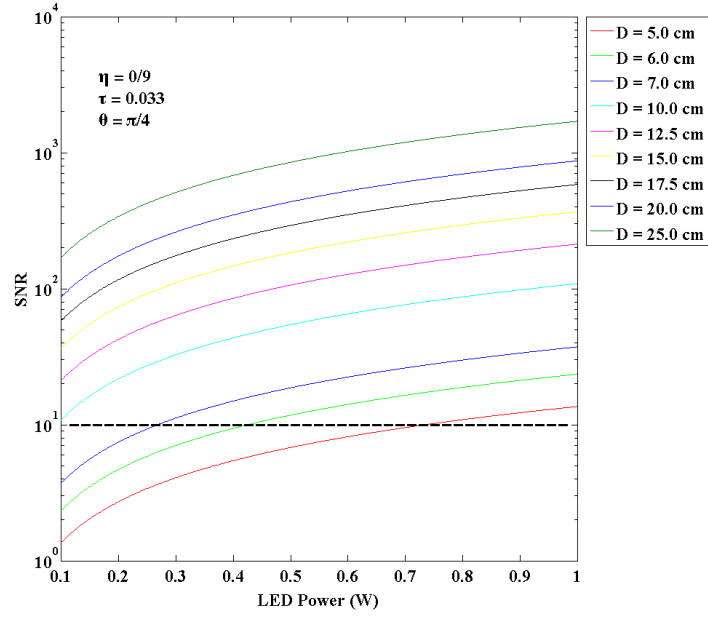Figure F.13:   SNR vs LED power plot with $\theta = \pi/4$ rad, $\eta = 0.9$, $\tau = 0.033$.
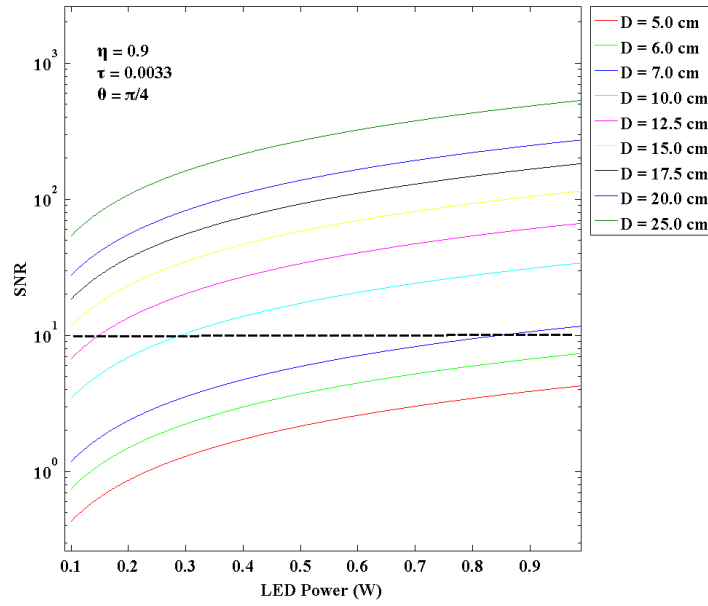


Figure F.14:   SNR vs LED power plot with $\theta = \pi/4$ rad, $\eta = 0.9$, $\tau = 0.0033$.
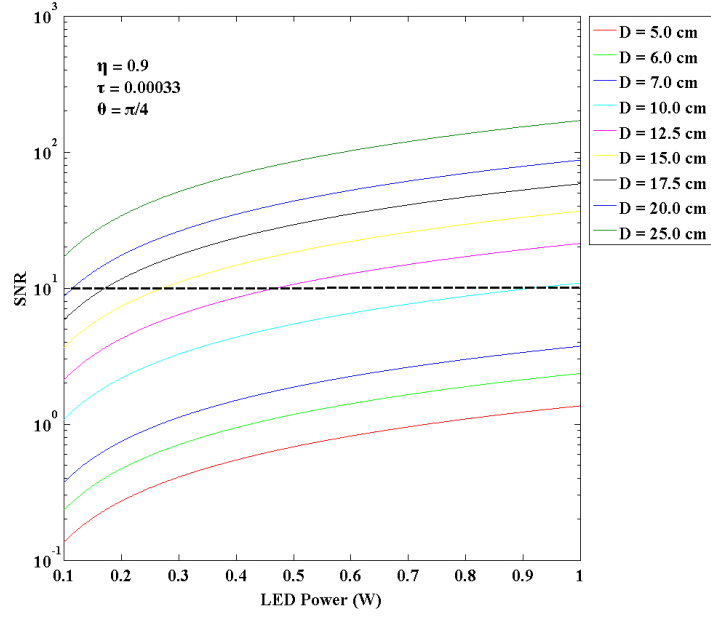
Figure F.15:    SNR vs LED power plot with $\theta = \pi/4$ rad, $\eta = 0.9$, $\tau = 0.00033$.
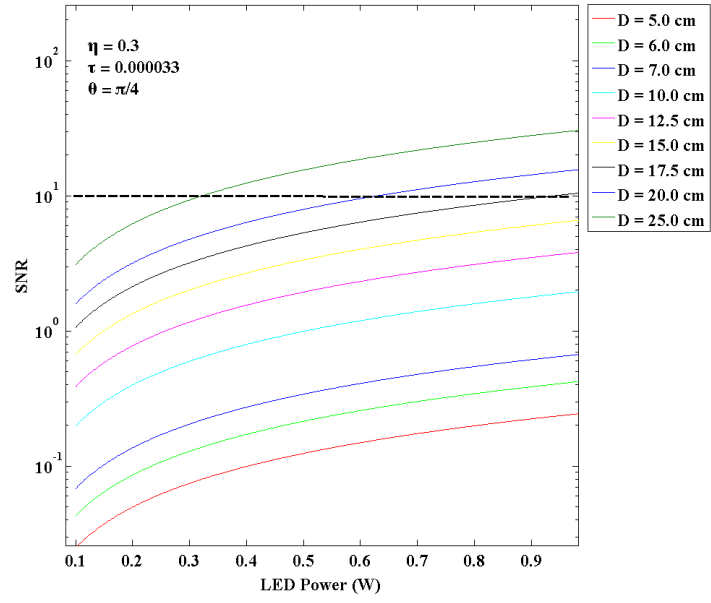


Figure F.16:    SNR vs LED power plot with $\theta = \pi/4$ rad, $\eta = 0.9$, $\tau = 0.000033$.

*Appendix G.   Code Used for Pretest Calculations*

```
clc; clear; clf
h = 6.626E-34;                          %J s
c = 2.998E8;                            %m/s  I need to convert all«
units to calculate using cm
c_cm = 2.998E10;                        %cm/s  I need to convert all«
units to calculate using cm
k = 1.38066E-23;                        %J/K
q = 1.60218e-19;                        %coulombs

T = 5793;                               %temp in Kelvin
%T = 4000
lambda = .250:0.01:2.50;                %units  in um
% 1 joule is 1 W-sec


%will make all plot print out
%%%%%%%%%%%%%%%%%%%%%%%%%%%%%%%%%%%%%%%%%%%%%%%%%%%%%%%%%%%%%%%%%%%%%%%%%
%Spectral Radiance calculation and plotting
%%%%%%%%%%%%%%%%%%%%%%%%%%%%%%%%%%%%%%%%%%%%%%%%%%%%%%%%%%%%%%%%%%%%%%%%%
%LeBB = @ (lambda)  2.*h.*c.^2./((lambda.^5.*1e-20).*exp(h.*c./(lambda.*k.«
*T.*1e-6))-1);      %w/m^2/um -sr
%Figure 1
%plot (lambda, LeBB(lambda))
%title('Plancks Blackbody equation--Spectral Radiance vs Wavelength (LeBB)')
%xlabel('Wavelength (nm)')
%ylabel ('Spectral Radiance (W m^{-2} sr^{-1} \mum^{-1})')
%figure
%%%%%%%%%%%%%%%%%%%%%%%%%%%%%%%%%%%%%%%%%%%%%%%%%%%%%%%%%%%%%%%%%%%%%%%%%


%%%%%%%%%%%%%%%%%%%%%%%%%%%%%%%%%%%%%%%%%%%%%%%%%%%%%%%%%%%%%%%%%%%%%%%%%
%Spectral irradiance calculation and plotting. EeBB=sun_solid_angle*LeBB
%%%%%%%%%%%%%%%%%%%%%%%%%%%%%%%%%%%%%%%%%%%%%%%%%%%%%%%%%%%%%%%%%%%%%%%%%
%The units of the spectral
%irradiance is W/m^2/um.  It is found by multiplying the radiance by the
%solid angle subtended by the earth.
%the earth subtends a solid angle within the emission cone of radiation
%leaving the sun.  That angle is 0.532 ^o == 9.3 mrad, calculaton  done
%below.
radconv = 0.532*pi/180;                 %solid angle conversion from degrees to«
radians   (theta)
solid_angle = pi*(radconv)^2/4;         %solid angle of the sun, used to get«
EeBB
EeBB = @ (lambda)  solid_angle*(2.*h.*c.^2./(lambda.^5.*10.^-20.*(exp(h.*c./«
(lambda.*10.^-6.*k.*T))-1)));   %w/cm^2/um
%Figure 2
%plot (lambda, EeBB(lambda));
%title('Plancks Blackbody equation--Spectral Irradiance vs Wavelength«
(EeBB)')
%xlabel('Wavelength (\mum)')
%ylabel ('Spectral Irradiance (W cm^{-2} \mum^{-1})')
%figure
%%%%%%%%%%%%%%%%%%%%%%%%%%%%%%%%%%%%%%%%%%%%%%%%%%%%%%%%%%%%%%%%%%%%%%%%%


%%%%%%%%%%%%%%%%%%%%%%%%%%%%%%%%%%%%%%%%%%%%%%%%%%%%%%%%%%%%%%%%%%%%%%%%%
%Modeling the large valley between 800 nm and 1100 nm--emissivity
%%%%%%%%%%%%%%%%%%%%%%%%%%%%%%%%%%%%%%%%%%%%%%%%%%%%%%%%%%%%%%%%%%%%%%%%%
```

```
lambda = 0.8:.001:1.1;
%lambda = 0.250:.001:2.5;
esun = @ (lambda) 0.85-0.52.*exp(-((lambda-0.93)./0.025).^2);
%Figure 3
%save my_data esun -ascii
%plot (lambda,esun(lambda));

%dlmwrite('my_data.out',EeBB)
%title('Emissivity equation modeling large valley)')
%xlabel('Wavelength (\mum)')
%ylabel ('Spectral Radiance (W m^{-2} \mum^{-1})')
%figure
%%%%%%%%%%%%%%%%%%%%%%%%%%%%%%%%%%%%%%%%%%%%%%%%%%%%%%%%%%%%%%%%%%%%%%%%
%emissivity*EeBB, the actual model used  for calculations
%%%%%%%%%%%%%%%%%%%%%%%%%%%%%%%%%%%%%%%%%%%%%%%%%%%%%%%%%%%%%%%%%%%%%%%%
model_irr = @ (lambda) EeBB(lambda).*esun(lambda);       %irradiance output
in w/cm^2/microns
%Figure 4
%plot (lambda,model_irr(lambda));
%title('Model for calculating noise due to solar background')
%xlabel('Wavelength (\mum)')
%ylabel ('Spectral Radiance (W cm^{-2} \mum^{-1})')
%figure
%%%%%%%%%%%%%%%%%%%%%%%%%%%%%%%%%%%%%%%%%%%%%%%%%%%%%%%%%%%%%%%%%%%%%%%%
%calculating the energy, in W, delivered to the detector
%%%%%%%%%%%%%%%%%%%%%%%%%%%%%%%%%%%%%%%%%%%%%%%%%%%%%%%%%%%%%%%%%%%%%%%%
%reflected solar exitance is found by multiplying the modeled irradiance by
%the reflectivity coefficient (rho).  Rho for asphalt was found at
%http://eetd.lbl.gov/coolroof/asshingl.htm to have a value of 0.05.
%Another site http://www.ecco.org/pdfs/EV24.pdf shows the same for asphalt
%and a much higher value for concrete, about 27%.
noise = quad(model_irr, .8, 1.1)              %solar irradiance on the ground;
modeled irradiance over range of interest
rho = 0.06;                      %reflection coefficient of asphalt, much
lower than card board
%rho = 0.718                      % this is the reflection coefficient
for paper according to  He Torrance model
%%%%%%%%%%%%%%%%%%%%%%%Marciniak used different numbers than I did.
Adet = .65*0.48;                 %Sprircon dimension 0.6 by 0.8 cm

D= 5.08;                         % 2 inch glass optic
D1 = 5;
D2 = 6;
D3 = 7;
D4 = 10;
D5 = 12.5;
D6 = 15;
D7 = 17.5;
D8 =20.0;
D9 = 25.0;

%D= 2.54;                         % smaller optic means that less noise
energy
%will be incident at the detector.  Also reduced the signal energy.
efl = 1;                         %focal length of glass optic 1 cm
Aoptic = pi*D^2/4;                       %cm^2
```

```
Aoptic1 = pi*D1^2/4;                        %cm^2
Aoptic2 = pi*D2^2/4;                        %cm^2
Aoptic3 = pi*D3^2/4;                        %cm^2
Aoptic4 = pi*D4^2/4;                        %cm^2
Aoptic5 = pi*D5^2/4;                        %cm^2
Aoptic6 = pi*D6^2/4;                        %cm^2
Aoptic7 = pi*D7^2/4;                        %cm^2
Aoptic8 = pi*D8^2/4;                        %cm^2
Aoptic9 = pi*D9^2/4;                        %cm^2

fov_opt = Adet/efl^2;                   %FOV of the detector
%%%%%%%%%%%%%%%%%%%%%%%

%%%final equation is emiss*LeBB*solidangle*rho*aoptic*opticfov/pi
%modle_irr = emiss*EeBB
%EeBB = LeBB*sun solid angle

lambda = 0.8:.001:1.1;                          %um
noise_phi_at_det = @ (lamdba) model_irr(lambda).*rho.*fov_opt.*Aoptic./pi;
%W  solar energy at the detector.  Since the
% reflected is lambertian, there is not cos-theta relationship here.  The
% energy is just a result of the 1/pi product.


noise_phi_at_det1 = @ (lamdba) model_irr(lambda).*rho.*fov_opt.*Aoptic1./pi;
noise_phi_at_det2 = @ (lamdba) model_irr(lambda).*rho.*fov_opt.*Aoptic2./pi;
noise_phi_at_det3 = @ (lamdba) model_irr(lambda).*rho.*fov_opt.*Aoptic3./pi;
noise_phi_at_det4 = @ (lamdba) model_irr(lambda).*rho.*fov_opt.*Aoptic4./pi;
noise_phi_at_det5 = @ (lamdba) model_irr(lambda).*rho.*fov_opt.*Aoptic5./pi;
noise_phi_at_det6 = @ (lamdba) model_irr(lambda).*rho.*fov_opt.*Aoptic6./pi;
noise_phi_at_det7 = @ (lamdba) model_irr(lambda).*rho.*fov_opt.*Aoptic7./pi;
noise_phi_at_det8 = @ (lamdba) model_irr(lambda).*rho.*fov_opt.*Aoptic8./pi;
noise_phi_at_det9 = @ (lamdba) model_irr(lambda).*rho.*fov_opt.*Aoptic9./pi;

%Figure 5
%plot (lambda, noise_phi_at_det(lambda));
%title('Energy delivered to the detector')
%xlabel('Wavelength \mum')
%ylabel ('Watts')
%figure
%%%%%%%%%%%%%%%%%%%%%%%%%%%%%%%%%%%%%%%%%%%%%%%%%%%%%%%%%%%%%%%%%%%%%%%%%%%


%%%%%%%%%%%%%%%%%%%%%%%%%%%%%%%%%%%%%%%%%%%%%%%%%%%%%%%%%%%%%%%%%%%%%%%%%%%
%shot noise current calculation
%%%%%%%%%%%%%%%%%%%%%%%%%%%%%%%%%%%%%%%%%%%%%%%%%%%%%%%%%%%%%%%%%%%%%%%%%%%
%eta = 0.6;
%eta = .5;                               %marciniak's number
%eta = .3;                               %my number
eta = .9                                %from paper
%eta = .6                                %assumed median value

%%%%%Matlab wont integrant a product, or I dont know how to do it, so I
%%%%%integrated lambda by hand and got lambda^2/2.  Evaluating from 0.8 to
%%%%%1.1 gives a final value of 0.285.  This is multiplied to expression to
```

```
%%%%%get final i_bar
int_lambda = (1.1^2/2 - 0.8^2/2)

%int_phi_at_det = quad(phi_at_det,0.8,1.1)
%i_bar = int_lambda.*(q.*eta.7(h.*c*1e6^2)).*quad(noise_phi_at_det,0.8,1.1)<
%extra 1e-6^2 term to convert
i_bar = int_lambda.*(6.4e-6.*q.*eta./(h.*c*1e6^2)).*quad(noise_phi_at_det,<
0.8,1.1)   %extra 1e-6^2 term to convert
%second equation is with pixel size added.

i_bar1 = int_lambda.*(q.*eta./(h.*c*1e6^2)).*quad(noise_phi_at_det1,<
0.8,1.1);
i_bar2 = int_lambda.*(q.*eta./(h.*c*1e6^2)).*quad(noise_phi_at_det2,<
0.8,1.1);
i_bar3 = int_lambda.*(q.*eta./(h.*c*1e6^2)).*quad(noise_phi_at_det3,<
0.8,1.1);
i_bar4 = int_lambda.*(q.*eta./(h.*c*1e6^2)).*quad(noise_phi_at_det4,<
0.8,1.1);
i_bar5 = int_lambda.*(q.*eta./(h.*c*1e6^2)).*quad(noise_phi_at_det5,<
0.8,1.1);
i_bar6 = int_lambda.*(q.*eta./(h.*c*1e6^2)).*quad(noise_phi_at_det6,<
0.8,1.1);
i_bar7 = int_lambda.*(q.*eta./(h.*c*1e6^2)).*quad(noise_phi_at_det7,<
0.8,1.1);
i_bar8 = int_lambda.*(q.*eta./(h.*c*1e6^2)).*quad(noise_phi_at_det8,<
0.8,1.1);
i_bar9 = int_lambda.*(q.*eta./(h.*c*1e6^2)).*quad(noise_phi_at_det9,<
0.8,1.1);

%i_bar = (1e-6).*(q.*eta./(h.*c)).*13e-3    %13 mw taken from the lab lights<
and the IR camera
%the C term from m to um.


t_int0 = 3.30
t_int = 0.33;                                               %seconds
t_int1 = .033;                                                %seconds
t_int2 = 0.0033;
t_int3 = 0.00033;
t_int4 = 0.000033;
t_int5 = 0.0000033;
delta_f = 1/t_int;
%%%%%%%%%%%%%%%%%%%%%%%%%%%%%%%%%%%%%%%%%%%%%%%%%%%%%%%%%%%%%%%%%%%%%%%%%%%%%%%
i_shot = sqrt(2.*q.*i_bar.*delta_f)                          %shot noise is<
in amps
%%%%%%%%%%%%%%%%%%%%%%%%%%%%%%%%%%%%%%%%%%%%%%%%%%%%%%%%%%%%%%%%%%%%%%%%%%%%%%%

i_shot1 = sqrt(6.40e-4^2.*2.*q.*i_bar1.*delta_f);
i_shot2 = sqrt(6.40e-4^2.*2.*q.*i_bar2.*delta_f) ;
i_shot3 = sqrt(6.40e-4^2.*2.*q.*i_bar3.*delta_f) ;
i_shot4 = sqrt(6.40e-4^2.*2.*q.*i_bar4.*delta_f) ;
i_shot5 = sqrt(6.40e-4^2.*2.*q.*i_bar5.*delta_f) ;
i_shot6 = sqrt(6.40e-4^2.*2.*q.*i_bar6.*delta_f) ;
i_shot7 = sqrt(6.40e-4^2.*2.*q.*i_bar7.*delta_f) ;
i_shot8 = sqrt(6.40e-4^2.*2.*q.*i_bar8.*delta_f) ;
i_shot9 = sqrt(6.40e-4^2.*2.*q.*i_bar9.*delta_f) ;
```

```
%%%%%%%%%%%%%%%%%%%%%%%%%%%%%%%%%%%%%%%%%%%%%%%%%%%%%%%%%%%%%%%%%%%%%%%%%%%%%%%
%Now i need the current generated by the LED, the signal current!!
%%%%%%%%%%%%%%%%%%%%%%%%%%%%%%%%%%%%%%%%%%%%%%%%%%%%%%%%%%%%%%%%%%%%%%%%%%%%%%%
Aspot = 18 * 3000;                              %area of spot on ground in cm^2
R = 50;                                         %m

%phi_sig_at_optic = (h*c*i_shot*100)/(q*980e-9*eta)
%phi_LED = phi_sig_at_optic * pi*R^2/(Aoptic*rho*1e-4)                  %W
%i_sig = phi_LED*rho*Aoptic*eta*q*980e-9/(pi*R^2*h*c*1e4)               %A


%%%%%%%%%%%%%%%%%%%%%%%%%%%%%%%%%%%%%%%%%%%%%%%%%%%%%%%%%%%%%%%%%%%
%brute forcing the answer
%%%%%%%%%%%%%%%%%%%%%%%%%%%%%%%%%%%%%%%%%%%%%%%%%%%%%%%%%%%%%%%%%%%

phi_LED = 0.1:.0015:1.00;                                               %W

%theta1 = 0
theta1 = 88.25*pi/180;
%for aerial vehicle
%theta2 = pi/4;
%signal_phi_det = @ (phi_LED) rho*phi_LED*cos(theta2)*Aoptic/(pi*R^2);
%W
%plot (phi_LED, signal_phi_det(phi_LED))
%figure

%%%%%%%%%%%%%%%%%%%%%%%%%%%%%%%%%AGV%%%%%%%%%%%%%%%%%%%%%%%%%%%%%%%%%%%%%%%%%%%
%        aeiral vehicle   45^o angle
%%%%%%%%%%%%%%%%%%%%%%%%%%%%%%%%%%%%%%%%%%%%%%%%%%%%%%%%%%%%%%%%%%%%%%%%%%%%%%%%
%signal_phi_det1 = @ (phi_LED) rho*phi_LED*cos(theta2)*Aoptic1/(pi*R^2);
%signal_phi_det2 = @ (phi_LED) rho*phi_LED*cos(theta2)*Aoptic2/(pi*R^2);
%signal_phi_det3 = @ (phi_LED) rho*phi_LED*cos(theta2)*Aoptic3/(pi*R^2);
%signal_phi_det4 = @ (phi_LED) rho*phi_LED*cos(theta2)*Aoptic4/(pi*R^2);
%signal_phi_det5 = @ (phi_LED) rho*phi_LED*cos(theta2)*Aoptic5/(pi*R^2);
%signal_phi_det6 = @ (phi_LED) rho*phi_LED*cos(theta2)*Aoptic6/(pi*R^2);
%signal_phi_det7 = @ (phi_LED) rho*phi_LED*cos(theta2)*Aoptic7/(pi*R^2);
%signal_phi_det8 = @ (phi_LED) rho*phi_LED*cos(theta2)*Aoptic8/(pi*R^2);
%signal_phi_det9 = @ (phi_LED) rho*phi_LED*cos(theta2)*Aoptic9/(pi*R^2);


%%%%%%%%%%%%%%%%%%%%%%%%%%%%%%%%%%%%%%%%%%%%%%%%%%%%%%%%%%%%%%%%%%%%%%%%%%%%%%%
%        AGV    88.25^o angle
%%%%%%%%%%%%%%%%%%%%%%%%%%%%%%%%%%%%%%%%%%%%%%%%%%%%%%%%%%%%%%%%%%%%%%%%%%%%%%%%
signal_phi_det1 = @ (phi_LED) 6.4e-4^2.*rho*phi_LED*cos(theta1)*Aoptic1/
(pi*R^2);
signal_phi_det2 = @ (phi_LED) 6.40e-4^2.*rho*phi_LED*cos(theta1)*Aoptic2/
(pi*R^2);
signal_phi_det3 = @ (phi_LED) 6.40e-4^2.*rho*phi_LED*cos(theta1)*Aoptic3/
(pi*R^2);
signal_phi_det4 = @ (phi_LED) 6.40e-4^2.*rho*phi_LED*cos(theta1)*Aoptic4/
(pi*R^2);
signal_phi_det5 = @ (phi_LED) 6.40e-4^2.*rho*phi_LED*cos(theta1)*Aoptic5/
(pi*R^2);
signal_phi_det6 = @ (phi_LED) 6.40e-4^2.*rho*phi_LED*cos(theta1)*Aoptic6/
(pi*R^2);
signal_phi_det7 = @ (phi_LED) 6.40e-4^2.*rho*phi_LED*cos(theta1)*Aoptic7/
```

G-6

```
(pi*R^2);
signal_phi_det8 = @ (phi_LED) 6.40e-4^2.*rho*phi_LED*cos(theta1)*Aoptic8/
(pi*R^2);
signal_phi_det9 = @ (phi_LED) 6.40e-4^2.*rho*phi_LED*cos(theta1)*Aoptic9/
(pi*R^2);


%i_sig = @ (phi_LED) signal_phi_det(phi_LED).*rho.*Aoptic.*(1/100)^2.*eta.
*q.*quad(noise_phi_at_det,0.8,1.1).*(1/1e6)./(pi.*R.^2.*h.*c); %A  lambda
integrated
i_sig = @ (phi_LED) signal_phi_det(phi_LED).*rho.*Aoptic.*(1/100)^2.*eta.*q.
*0.980.*(1/1e6)./(pi.*R.^2.*h.*c);   %A  lambda = 0.980


%%%%%%%%%%%%%%%%%%%%%%%%%%%%%%using the actual lambda value%%%%%%%%%%%%%%%%%%%%%%%%%
%i_sig1 = @ (phi_LED) signal_phi_det1(phi_LED).*rho.*Aoptic1.*(1/100)^2.
*eta.*q.*0.980.*(1/1e6)./(pi.*R.^2.*h.*c);
%i_sig2 = @ (phi_LED) signal_phi_det2(phi_LED).*rho.*Aoptic2.*(1/100)^2.
*eta.*q.*0.980.*(1/1e6)./(pi.*R.^2.*h.*c);
%i_sig3 = @ (phi_LED) signal_phi_det3(phi_LED).*rho.*Aoptic3.*(1/100)^2.
*eta.*q.*0.980.*(1/1e6)./(pi.*R.^2.*h.*c);
%i_sig4 = @ (phi_LED) signal_phi_det4(phi_LED).*rho.*Aoptic4.*(1/100)^2.
*eta.*q.*0.980.*(1/1e6)./(pi.*R.^2.*h.*c);
%i_sig5 = @ (phi_LED) signal_phi_det5(phi_LED).*rho.*Aoptic5.*(1/100)^2.
*eta.*q.*0.980.*(1/1e6)./(pi.*R.^2.*h.*c);
%i_sig6 = @ (phi_LED) signal_phi_det6(phi_LED).*rho.*Aoptic6.*(1/100)^2.
*eta.*q.*0.980.*(1/1e6)./(pi.*R.^2.*h.*c);
%i_sig7 = @ (phi_LED) signal_phi_det7(phi_LED).*rho.*Aoptic7.*(1/100)^2.
*eta.*q.*0.980.*(1/1e6)./(pi.*R.^2.*h.*c);
%i_sig8 = @ (phi_LED) signal_phi_det8(phi_LED).*rho.*Aoptic8.*(1/100)^2.
*eta.*q.*0.980.*(1/1e6)./(pi.*R.^2.*h.*c);
%i_sig9 = @ (phi_LED) signal_phi_det9(phi_LED).*rho.*Aoptic9.*(1/100)^2.
*eta.*q.*0.980.*(1/1e6)./(pi.*R.^2.*h.*c);

%done the correct way, as opposed to above which is slightly incorrect
i_sig1 = @ (phi_LED) signal_phi_det1(phi_LED).*(1/100)^2.*eta.*q.*0.980.*
(1/1e6)./(h.*c);
i_sig2 = @ (phi_LED) signal_phi_det2(phi_LED).*(1/100)^2.*eta.*q.*0.980.*
(1/1e6)./(h.*c);
i_sig3 = @ (phi_LED) signal_phi_det3(phi_LED).*(1/100)^2.*eta.*q.*0.980.*
(1/1e6)./(h.*c);
i_sig4 = @ (phi_LED) signal_phi_det4(phi_LED).*(1/100)^2.*eta.*q.*0.980.*
(1/1e6)./(h.*c);
i_sig5 = @ (phi_LED) signal_phi_det5(phi_LED).*(1/100)^2.*eta.*q.*0.980.*
(1/1e6)./(h.*c);
i_sig6 = @ (phi_LED) signal_phi_det6(phi_LED).*(1/100)^2.*eta.*q.*0.980.*
(1/1e6)./(h.*c);
i_sig7 = @ (phi_LED) signal_phi_det7(phi_LED).*(1/100)^2.*eta.*q.*0.980.*
(1/1e6)./(h.*c);
i_sig8 = @ (phi_LED) signal_phi_det8(phi_LED).*(1/100)^2.*eta.*q.*0.980.*
(1/1e6)./(h.*c);
i_sig9 = @ (phi_LED) signal_phi_det9(phi_LED).*(1/100)^2.*eta.*q.*0.980.*
(1/1e6)./(h.*c);
```

```matlab
%i_sig = @ (phi_LED) phi_LED.*rho.*Aoptic.*(1/100)^2.*eta.*q.*0.980.*↵
(1/1e6)./(pi.*R.^2.*h.*c);    %A

%i_sig =20.*rho.*Aoptic.*(1/100)^2.*eta.*q.*0.980.*(1/1e6)./(pi.*R.^2.*h.*c)↵
%A
%%%%%%%%%%%%%entering the energy delivered to the target, which was 20 W.
%Figure 6
%loglog (phi_LED, i_sig(phi_LED))
%title('Signal Current  i_{sig}')
%xlabel('LED Power (W)')
%ylabel('Current (A)')
%figure


%SNR = @ (phi_Led) i_sig(phi_LED)./i_shot;

SNR1 = @ (phi_Led) i_sig1(phi_LED)./i_shot1;
SNR2 = @ (phi_Led) i_sig2(phi_LED)./i_shot2;
SNR3 = @ (phi_Led) i_sig3(phi_LED)./i_shot3;
SNR4 = @ (phi_Led) i_sig4(phi_LED)./i_shot4;
SNR5 = @ (phi_Led) i_sig5(phi_LED)./i_shot5;
SNR6 = @ (phi_Led) i_sig6(phi_LED)./i_shot6;
SNR7 = @ (phi_Led) i_sig7(phi_LED)./i_shot7;
SNR8 = @ (phi_Led) i_sig8(phi_LED)./i_shot8;
SNR9 = @ (phi_Led) i_sig9(phi_LED)./i_shot9;

%Figure 7
%plot (phi_LED, SNR(phi_LED))
%dlmwrite('snrout.txt',SNR(phi_LED),'\t')
title('SNR vs LED Power')
xlabel('LED Power (W)')
ylabel ('SNR')
%figure
%%%%%%%%%%%%%%%%%%%%%%%%%%%%%%%%%%%%%%%%%%%%%%%%%%%%%%%%%%%%%%%%%%%%%%%%
%Figure 8
semilogy (phi_LED,SNR1(phi_LED),'r',phi_LED,SNR2(phi_LED),'g',phi_LED,SNR3↵
(phi_LED),'b',...
    phi_LED,SNR4(phi_LED),'c',phi_LED,SNR5(phi_LED),'m',phi_LED,SNR6↵
(phi_LED),'y',...
    phi_LED,SNR7(phi_LED),'k',phi_LED,SNR8(phi_LED),phi_LED,SNR9(phi_LED))
%loglog (phi_LED, SNR1(phi_LED),phi_LED,SNR4(phi_LED),phi_LED,SNR6(phi_LED),↵
phi_LED,SNR9(phi_LED))
%dlmwrite('snrout.txt',SNR(phi_LED),'\t')
%title('SNR vs LED Power')
xlabel('LED Power (W)','fontsize',24,'fontname','times new↵
roman','fontweight','bold')
ylabel ('SNR','fontsize',24,'fontname','times new↵
roman','fontweight','bold')
%currentaxes('fontsize',20,'fontname','times new roman')
legend('D = 5.0 cm','D = 6.0 cm','D = 7.0 cm', 'D = 10.0 cm','D = 12.5↵
cm','D = 15.0 cm','D = 17.5 cm','D = 20.0 cm','D = 25.0 cm')
figure


%%%%%%%%%%%%%%%%%%%%%%%%%%%%%%%%%%%%%%%%%%%%%%%%%%%%%%%%%%%%%%%%%%%%%%%%%%

%%%%%%%%%%%%%%%%%%%%%%%%%%%%%%%%%%%%%%%%%%%%%%%%%%%%%%%%%%%%%%%%%%%%%%%%%%
```

```
%       Range plots---done manually--ignore this
%%%%%%%%%%%%%%%%%%%%%%%%%%%%%%%%%%%%%%%%%%%%%%%%%%%%%%%%%%%%%%%%%%%%%%%

%PHI_LED = 0:0.01:1.0;
%Range = @ (PHI_LED)  (rho.^2.*Aoptic.^2.*PHI_LED.*cos(theta2).*eta.*q/↵
(i_sig9(PHI_LED).*pi.^2.*h.*c.*100)).^(.25);
%plot (PHI_LED, Range(PHI_LED))
%xlabel('LED Power Rating (mW)')
%ylabel ('Distance to Target (cm)')
%plot (PHI_LED,i_sig5(PHI_LED))
%%%%%%%%%%%%%%%%%%%%%%%%%%%%%%%%%%%%%%%%%%%%%%%%%%%%%%%%%%%%%%%%%%%%%%%


%%%%%%%%%%%%%%%%%%%%%%%%%%%%%%%%%%%%%%%%%%%%%%%%%%%%%%%%%%%%%%%%%%%%%%%
%Calcualte the noise from the lab lights for the remote sensing demo

lambdamod = 800:10:1100;
%intensity = @(lambdamod) (2e-13.*lambdamod.^2) - (3e-10.*lambdamod) +↵
0.0000002;


%%%%%%%%%%%%%%%%%%%%%%%%%%%%%%%%%%%%%%%%%%%%%%%%%%%%%%%%%%%%%%%%%%%%%%%%↵
%%%%%%%
%new model for the intensity of the fluorescent lights in the lab.  Must
%choose intensity calculation below
%%%%%%%%%%%%%%%%%%%%%%%%%%%%%%%%%%%%%%%%%%%%%%%%%%%%%%%%%%%%%%%%%%%%%%%%↵
%%%%%%%
lambda = 800:.5:1100;
y1 = @ (lambda) 1e-8.*exp(-((lambda-810)./5).^2);
y2 = @ (lambda) .5e-9.*exp(-((lambda-830)./5).^2);
y3 = @ (lambda) .5e-9.*exp(-((lambda-878)./3).^2);
y4 = @ (lambda) .5e-9.*exp(-((lambda-893)./3).^2);
y5 = @ (lambda) 2.6e-8.*exp(-((lambda-1015)./5).^2);

yfinal = @ (lambda) (4e-9 + y1(lambda) + y2(lambda) + y3(lambda) + y4↵
(lambda) + y5(lambda));
%intensity = @(lambdamod) (2e-13.*lambdamod.^2) - (3e-10.*lambdamod)+0.↵
0000002;
intensity = @ (lambda) 4e-9 + y1(lambda) + y2(lambda) + y3(lambda) + y4↵
(lambda) + y5(lambda);
%y = @ (lambda) 0.85+0.12e-8.*exp(-((lambda-0.81)./0.005).^2);

%esun = @ (lambda) 0.85 [verticle shift]
                   %+0.12 [amplitued]
                   %.*exp(-((lambda-
                   %0.93) [horizontal shift]
                   %0.0025  [width of peak])  .^2);


plot(lambda,yfinal(lambda))
%dlmwrite('my_data.out',y)
%save my_data.out y -ASCII
xlabel('Wavelength (nm)','fontsize',24,'fontname','times new↵
roman','fontweight','bold')
ylabel ('Spectral Irradiance (W cm^{-2} nm^{-1})','fontsize',↵
24,'fontname','times new roman','fontweight','bold')
```

G-9

```
%x = 0:.1:1;
%y = [x; exp(x)];
%fid = fopen('exp.txt', 'wt');
%fprintf(fid, '%6.2f %12.8f\n', y);
%fclose(fid)

%***************************this puts the data in a***********************file%
y = [lambda; .1e-8 + y1(lambda) + y2(lambda) + y3(lambda) + y4(lambda) + y5↵
(lambda)];
fid = fopen('exp.txt', 'wt');
fprintf(fid, '%6.2f %12.8f\n', y);
fclose(fid)
%%%%%%%%%%%%%%%%%%%%%%%%%%%%%%%%%%%%%%%%%%%%%%%%%%%%%%%%%%%%%%%%%%%%%%%%%%%%%↵
%%%%%%%




%plot (lambdamod, intensity(lambdamod))

int_lambdamod = (1.1^2/2 - 0.8^2/2);
%i_barlights = (1e-6).*int_lambdamod.*(q.*eta./(h.*c)).*quad(intensity,↵
0.8,1.1);   %extra 1e-6 term to convert
i_barlights = 6.4e-6.*(1e-6).*int_lambdamod.*(q.*eta./(h.*c)).*quad↵
(intensity,0.8,1.1);   %extra 1e-6 term to convert
%the 6.4e-6 is the size of the pixel from marciniak
i_shot_lights = sqrt(2.*q.*i_barlights.*delta_f)                        %↵
shot noise is in amps
i_sig_cots = .371.*rho.*Aoptic.*(1/100)^2.*eta.*q.*0.980.*(1/1e6)./(pi.*R.↵
^2.*h.*c)    %A
%use below equation only if I am not supposed to use rho, Aoptic, and R^2.
%i_sig_cots = .371.*(1/100)^2.*eta.*q.*0.980.*(1/1e6)./(pi.*h.*c)    %A
%%%%%%%%%%%%%%%%%%%%%%%%%%%%%%%%%%%%%%%%%%%%%%%%%%%%%%%%%%%%%%%%%%%%%%%%%%%
%noise_lights = 6.4e-6.*quad(intensity,0.8,1.1)
%noise_lights = 6.4e-6.*int_lambdamod.*(q.*eta./(h.*c)).*quad(intensity,↵
0.8,1.1)

noise_lights = 6.4e-6.*int_lambdamod.*(q.*eta./(h.*c)).*quad(intensity,↵
0.8,1.1)

slr = i_shot_lights/i_shot

energy_at_det = (10*i_shot)^2*h*c/(2*q^2*delta_f*eta*int_lambda);    %energy↵
needed at the detector to be 20dB over the solar noise


%from marciniak   background noise is about 106 pW.  The shot noise
%current calculated from em at about 3.2071e-17.  The signal flux is
%7.8e-12 A.  This new flux will produce a signal current of 3.6 e-12.  Now↵
we can
%get the SNR using these new values, which is 110877.  In dB this is 50.4
%dB.

%need to calculate i_shot_full and change the values of i_sig in the
%document to reflect the numbers per using the pixel size as an aperture.
```

G-10

```
%%%%%%%%%%%%%%new stuff from marciniak%%%%%%%%%%%% recalculated scaled signal
%%%%%%%%%%%%%%power and current*********************
area_pix = 6.4e-4^2
phi_sig_full = rho*0.216*(area_pix/.75)*(pi*0.0504^2/4)/(pi*18*3000)
Isig_full = phi_sig_full*eta*q*980e-7/(h*c)
```

## Bibliography

1. Arvesen, March 2008. URL `ngdc.noaa.gov/STP/SOLAR_DATA/SOLAR_IRRADIANCE`.

2. Bjork, B., Y. Yamamoto, and H. Heitmann. "Spontaneous emission control in semiconductor microcavities in confined electrons and photons", 1995.

3. Campbell, James B. *Introduction to Remote Sensing*. The Guildford Press, 2007.

4. Carr, W. N. and G. E. Pittman. "One-watt GaAs p-n junction infrared source". *Applied Physics Letters*, 3:173, 1963.

5. Chin, R. T. and C. R. Dyer. "Model-Based Recognition in Robot Vision". *Computing Surveys*, 18:67–108, 1996.

6. Chynoweth, A. G. and K. G. McKay. "Internal field emission in silicon p-n junctions". *Physics Review*, 106:418, 1957.

7. Coldren, L. A. and S. W. Corzine. *Diode lasers and photonic integrated circuits*. John Wiley and Sons, Inc., 1995.

8. (DARPA), Defense Advanced Research Programs Agency. "http://www.darpa.mil/grandchallenge".

9. Esaki, L. "Discovery of the Tunnel Diode". *IEEE Transactions on Electron Devcies*, ED-23(7), 1976.

10. Fletcher, R. M, C. P. Kuo, T. D. Osentowski, K. H. Huang, and M. G. Crawford. "The growth and properties of high performance AlInGaP emitters using lattice mismatched GaP Window layers". *Journal of Electrical Materials*, 20(1125), 1991.

11. Franklin, A. R. and R. Newman. "Shaped electroluminescent GaAs diodes". *Journal of Applied Physics*, 35:1153, 1964.

12. Fuerstenberg, Kay and Roland Schulz. "Laserscanners for Driver Assistance". *Final Program of the 3rd International Workshop on Intelligent Transportation (WIT 2006)*. 2006.

13. Garcia, J. C., E. Rosencher, P. H. Collot, N. Laurent, J. L. Guyaux, B. Vinter, and J. Nagle. "Expitaxially stacked lasers with Esaki juncctions: A bipolar cascade laser". *Applied Physics Letters*, 71(26), 1997.

14. Hall, R. N. "Recombination process in semiconductors". *Proceedings of IEE*, 93(106 B), 1960.

15. Hall, R. N. "Tunnel Diodes". *IRE Transactions on Electron Devices*, 1–9, 1960.

16. Hunt, N. R. J, E. F. Schubert, D. L. Sivco, A. Y. Cho, and G. J. Zydzid. "Power and efficiency limits in single-mirror light-emitting diodes with enhanced intensity". *Electron. Lett.*, 28(2169), 1992.

17. Hyperphysics. URL `http://hyperphysics.phy-astr.gsu.edu`.

18. IJCAI'99. *Active global localization for mobile robot using multilple hypothesis tracking*, 1999.

19. Jelalian, Albert V. *Laser Radar Systems*. Artech House, Inc, 1992.

20. Jr., H. Holonyak. "From transistors to light emitters". *IEEE Journal of Selected Toptic in Quantum Electronics*, 6(6), 2000.

21. Korshak, A. N., Z. S. Gribnikov, and V. V. Mitin. "Tunnel-junction-connected distributed-feedback vertical cavity surface emitting laser". *Applied Physics Letters*, 73(11), 1998.

22. Langley, D., J. Gillespie, and M. Bellott. Conversations with Capt Derrick Langley, Capt Bellott, and James Gillespie concerning the adhesion of conformal metal to SiN, 2007.

23. Laserfocus. URL `www.laserfocusworld.com`.

24. Liu, X., M. H. Hu, H. K. Nguyen, C. G. Caneau, M. H. Rasmussen, R. W. Davis Jr., and C. Zah. "Comparison between epi-down and epi-up bonded high-power single-mode 980 nm semiconductor laser". *IEEE Transactions on Advanced Packaging*, 27(4):640–646, November 2004.

25. Lott, J. A. Advanced Microelectronics course taught at the Air Force Institute of Technology by Dr. J. A. Lott in 2006.

26. Marciniak, M. Discussion with Dr. Mark Marciniak, Professor at the Air Force Institute of Technology, WPAFB, OH, March 2008.

27. McKay, K. G. "Observations of Zener current in germanium p-n junctions". *Physics Review*, 83:650, 1951.

28. McKay, K. G. "Avalanche breakdown in silicon". *Physics Review*, 94:877, 1954.

29. McKay, K. G. and K. B. McAfee. "Electronic multiplication in silicon and germanium". *Physics Review*, 94:877, 1954.

30. Miller, M., M. Grabherr, R. Jager, M. Kicherer, F. Mederer, and K. J. Ebeling. "kW/cm2 VCSEL Arrays for High Power Applications". K. D. Choquette and C. Lei (editors), *Vertical-Cavity Surface-Emitting Lasers IV*, volume 3946, 198–206. SPIE, 2000.

31. Miller, S. L. "Avalanche breakdown in germanium". *Physics Review*, 99:1234, 1955.

32. Moller, C., J. Bottcher, M. Protsch, and H. Dunzel. "GaAs-Based tunnel junctions for micro-cavity devices". invited talk, IEEE, 2002.

33. Muscara, A., M. E. Stagna, S. Leonardi, S. Coffa, L. Caristia, and S. Lorenti. "Design and electro-optical characterization of Si-bsed resonant cavity light emit-

ting devcies at 850 nm". *Journal of Luminescence*, 121(121):293–297, December 2006.

34. Nelson, T. "Conversation with Dr. Thomas Nelson at AFRL, at WPAFB in Dayton, OH".

35. Nelson, T. and J. Ehret. Discussion with Dr. Tom Nelson, AFRL/RY and Mr. Jim Ehret, AFRL/ML, concering optimizing the slope efficiency of tunnel junctions., 2006.

36. Ng, T. C. *Development of a 3D LADAR system for autonomous vehicle guidance.* Technical Report 1, SIMTech, 2005.

37. Olshansky, R., C. B. Su, J. Manning, and W. Powazinik. "Measurement of radiative and non-radiative recombination rates in InGaAsP and AlGaAs light sources". *IEEE Journal of Quantum Electronics*, 838, 1984.

38. Page, H., A. Robertson, C. Sirtori, C. Becker, G. Glastre, and J. Nagle. "Demonstration of GaAs-based auantum cascade laser operating on a Peltier cooled element". *IEEE Photonics Technology Letters*, 13(6):556–558, 2001.

39. Palik, E. D. *Handbook of optical constants of solids.* Academic Press, 1998.

40. Qu, Y., S. Yuan, C. Y. Liu, B. Bo, G. Liu, and H. Jiang. "High-power In-AlGa/GaAs and AlGaAs/GaAs semiconducor laser arrays emitting at 808 nm". *IEE Photonics Technology Letters*, 16(2):389–391, February 2004.

41. Razeghi, M. and G. J. Brown (editors). *Improved performace of quantum cascade lasers via manufacturable quality epitaxial side down m ounting process utilizing aluminum nitride heatsinks*, volume 6127. Center for Quantum Devices, SPIE, Norwestern University, Evanston IL, 2006.

42. Round, J. H. "A note on carborundum". *Electrical World*, 19:309, 1907.

43. Saing-Marc, P., J. L. Jezouin, and G. Medioni. "A versitle PC Based Range Finding System". *IEEE Transactions on Robotics and Automation*, 7(2):250 – 256, April 1991.

44. Schockely, W. *Electrons and holes in semiconductors.* D. Van Nostrand Company, 1950.

45. Schockley, W. and W. T. Read. "Statistic of the recombination of holes and electrons". *Physics Review*, 87(835), 1952.

46. Schubert, E. F. *Light Emitting Diodes.* Cambridge University Press, 2003.

47. Schubert, E. F. *Light Emitting Diodes.* Cambridge University Press, Cambridge, 2006.

48. Schubert, E. F., J. N. E. Hunt, Malik R. J., M. Micovic, and D. Miller. "Temperature and modulation characteristics of resonant-cavity light emitting diodes". *Journal of Lightwave Technology*, 14(7), 1996.

49. Seetharaman, Dr. Guna. "Discussion with Dr. Guna Seetharaman, Professor at The Air Force Institute of Technology", 2006. Discussion with Dr. Guna Seetharaman, Professor at The Air Force Institute of Technology.

50. Seetharaman, G. S., K. P. Valavanis, M. C. Mulder, and M. Bayoumi. *A Hybrid Range-Intensity Sensor for Dynamic Scene Analysis and Sensor Fusion.* Technical Report TR 91-1-12, The Center for Advanced Computer Studies, The University of Southwestern Louisiana, Lafayette, LA 70504-44330, May 1991.

51. Seyrafi, K. and S. A Hovanessian. *Introduction to Electro-Optical Imaging and Tracking Systems.* Artech House, Inc, New York, 1993.

52. Siskaninetz, W. J. *Bipolar Cascade Vertical-Cavity Surface-Emitting Lasers for RF Photonic Link Applications.* Ph.D. thesis, The Air Force Institute of Technology, 2007. Dissertation, AFIT/DS/ENG/07-22.

53. Siskaninetz, W. J., J. E. Ehret, T. Dang, J. E. Van Nostrand, J. A. Lott, and T. R. Nelson. "Reduced power consumption in GaAs based bipolar cascade lasers". *Electronics Letters*, 38(26), 2002.

54. Stettner, R., H. Bailey, and R. Richmond AFRL. "A 3D FLASH LIDAR". *SPIE*, April 2001.

55. Sugawara, H., M. Ishikawa, Y. Kokubun, Y. Nishikawa, S. Naritsuka, G. Hatakoshi, and M. Suzuki. "Semiconductor Light Emitting Device". US Patent 5,153,889, October 6 1992.

56. Surmann, H., K. Lingermann, A. Nuchter, and J. Hertzberg. "A 3D laser range finder for autonomous mobile robots", April 2001.

57. Sze, S. M. *Semiconductor Devices: Physics and Technology, 2nd Edition.* John Wiley and Sons, Inc., 2002.

58. Talghader, J. and J. S. Smith. "Conference of Lasers and Electro-Optics". *Paper CWF4.* Lasers and Electro-Optics, Baltimore, MD, 1995.

59. Tirerack, March 2008. URL `http://www.tirerack.com`.

60. Velodyne. "Velodyne Website:http://www.velodyne.com/lidar/", October 2007. URL `http://www.velodyne.com/lidar/`.

61. Walthelm, A. and A. M. Momlouk. "Multisensoric active spatial exploration and modeling". in Bynamische Perzeption: Workshop der GI-Fachgruppe 1.0.4.

62. Walthelm, A. and A. M. Momlouk. Westin, S. H., H. Li, and K. E. Torrance "A comparison of four BRDF models". submitted for publication at the 2004 Eurographics Symposium on Rendering, 2004

63. Wipiejewski, T., M. G. Peters, B. J. Thibeault, D. B. Yound, and L. A. Coldren. "Size-dependent output power saturation of Vertical-Cavity Surface-Emitting Laser diodes". *IEE Photonics Technology Letters*, 8(1):10–12, January 1996.

64. Yariv, A. *Quantum Electronics.* John Wiley and Sons, Inc., third edition, 1989.

65. van der Ziel, J. P. and W. T. Tsang. "Intergrated multilayer GaAs laser separated by tunnel junctions". *Applied Physics Letters*, 41(6), 1982.

*Vita*

Major Reginald J. Turner graduated from Avondale High School in Avondale Estates, Georgia. He entered undergraduate studies at Tuskegee University, located in Tuskegee, Alabama, where he graduated with a Bachelor's degree in Electrical Engineering in 1993. He was commissioned through the Reserve Officer Training Course, at Tuskegee University, in 1993. In 1995, he earned his first Masters degree in Electrical Engineering from North Carolina Agricultural and Technical State University, located in Greensboro, North Carolina. In 2000, Major Turner finished his second Masters degree in Divinity and Theological Studies from the United Theological Seminary, located in Dayton, Ohio.

Major Turner was first assigned to the National Air Intelligence Center, Wright-Patterson AFB, Ohio where he served as an intelligence analyst. In June 1998, he was assigned to HQ, Air Force Research Laboratory, Plans and Programs, Wright-Patterson AFB, Ohio, where he served as a Program Manager for Planning and Assessments. Next, he was hand picked to direct the Laser Effects Test Facility, and manage the Ground-Based Laser Technology program, Kirtland AFB, Albuquerque, New Mexico, where he later became the Deputy Chief, Laser Effects Research Branch, Air Force Research Laboratory, Detachment 12, Kirtland AFB, New Mexico. While there, he was selected to attend the Air Force Institute of Technology in August 2004. Upon graduation, he will be assigned to The National Security Agency, Ft George Meade, Maryland. Major Turner was selected for promotion to the rank of Lt Col in November 2007 and is scheduled to assume this rank in September 2008.

Permanent address:   Air Force Institute of Technology
2950 Hobson Way
Wright-Patterson AFB, OH 45433-7765

VITA-1

| 1. REPORT DATE *(DD-MM-YYYY)* 07-05-2008 | 2. REPORT TYPE **Doctoral Dissertation** | 3. DATES COVERED *(From – To)* September 2004-June 2008 |
|---|---|---|

| 4. TITLE AND SUBTITLE | 5a. CONTRACT NUMBER |
|---|---|
| A Wide Area Bipolar Cascade Resonant Cavity Light Emitting Diode for A Hybrid Range-Intensity Sensor | 5b. GRANT NUMBER |
| | 5c. PROGRAM ELEMENT NUMBER |
| **6. AUTHOR(S)** | 5d. PROJECT NUMBER |
| Turner, Reginald J., Major, USAF | 5e. TASK NUMBER |
| | 5f. WORK UNIT NUMBER |

| 7. PERFORMING ORGANIZATION NAMES(S) AND ADDRESS(S) | 8. PERFORMING ORGANIZATION REPORT NUMBER |
|---|---|
| Air Force Institute of Technology Graduate School of Engineering and Management (AFIT/EN) 2950 Hobson Way WPAFB OH 45433-7765  DSN: 785-3636 | AFIT/DEE/ENG/08-12 |

| 9. SPONSORING/MONITORING AGENCY NAME(S) AND ADDRESS(ES) | 10. SPONSOR/MONITOR'S ACRONYM(S) |
|---|---|
| Dr. Robert Bedford AFRL/RY 2241 Avionic Circle, Area B Bldg 620 WPAFB, OH 45433-7301 | 11. SPONSOR/MONITOR'S REPORT NUMBER(S) |

**12. DISTRIBUTION/AVAILABILITY STATEMENT**

APPROVED FOR PUBLIC RELEASE; DISTRIBUTION UNLIMITED

**13. SUPPLEMENTARY NOTES**

**14. ABSTRACT**

This dissertation focused on the development of an illuminator for the HRIS. This illuminator enables faster image rendering and reduces the potential of errors in return signal data, that could be generated from extremely rough terrain. Four major achievements resulted from this work, which advance the field of 3-D image acquisition. The first is that the TJ is an effective current spreading layer for LEDs with mesa width up to 140 μm and current densities of $\sim 1 \times 10^6$ A/cm$^2$. The TJ allows fabrication of an efficient illuminator, with required geometry for the HRIS to operate as a real-time 3-D imaging system. Secondly, a design for a Bipolar Cascade-Resonant Cavity Light Emitting Diode (BC-RCLED) has been accomplished, that will illuminate the FOV of the hybrid-ranged intensity system with a single sweep of the beam. This device is capable of producing $\sim 330$ mW of output power. Additionally, from this work, key parameters for HRIS design were identified. Using a collection optic with a 15 cm diameter, an HRIS mounting height of 1.5 m, and a detector integration time of 330 msec, a SNR of 20 dB was achieved. Lastly, we demonstrated that the BC-RCLED designed for the HRIS can deliver sufficient energy to produce the required SNR. Also, through parametric analysis, we determined that a system trade-off, between the collection optic diameter, and the integration time, results in an increase in the SNR from 20 to nearly 50, or extending the operational range from 50 to nearly 130 m.

**15. SUBJECT TERMS**
Remote Sensing, real-time 3-D imagery, Advanced LIDARs, Resonant Cavity Light Emitting Diodes, Esaki Tunnel Junction

| 16. SECURITY CLASSIFICATION OF: | | | 17. LIMITATION OF ABSTRACT | 18. NUMBER OF PAGES | 19a. NAME OF RESPONSIBLE PERSON **Maj LaVern Starman, PhD (ENG)** |
|---|---|---|---|---|---|
| REPORT U | ABSTRACT U | c. THIS PAGE U | UU | 194 | 19b. TELEPHONE NUMBER *(Include area code)* (937) 255-6565; email: lavern.starman@afit.edu |

**Standard Form 298 (Rev: 8-98)**
Prescribed by ANSI Std. Z39-18